Strain Responses And Transport Properties in Strontium Titanate-based Complex Oxide Devices

by

Xinyi Wu

B.S., University of Science and Technology of China, 2016

M.S., University of Pittsburgh, 2017

Submitted to the Graduate Faculty of
the Dietrich School of Arts and Sciences in partial fulfillment
of the requirements for the degree of

Doctor of Philosophy

University of Pittsburgh

2022

UNIVERSITY OF PITTSBURGH

DIETRICH SCHOOL OF ARTS AND SCIENCES

This dissertation was presented

by

Xinyi Wu

It was defended on

November 15th, 2022

and approved by

Dr. Jeremy Levy, Department of Physics and Astronomy, University of Pittsburgh

Dr. Tao Han, Department of Physics and Astronomy, University of Pittsburgh

Dr. Michael Hatridge, Department of Physics and Astronomy, University of Pittsburgh

Dr. Roger Mong, Department of Physics and Astronomy, University of Pittsburgh

Dr. David Waldeck, Department of Chemistry, University of Pittsburgh

Dissertation Director: Dr. Jeremy Levy, Department of Physics and Astronomy, University of Pittsburgh

Strain Responses And Transport Properties in Strontium Titanate-based Complex Oxide Devices

Xinyi Wu, PhD

University of Pittsburgh, 2022

In this thesis, I summarize my work in mesoscale devices created in strontium titanate ($SrTiO_3$)-based heterostructures, seeking to deepen the understanding of superconductivity and electron-pairing in those materials. In Chapter 1, relevant advances in the field of $SrTiO_3$, lanthanum aluminate and strontium titanate ($LaAlO_3/SrTiO_3$), and samarium titanate and strontium titanate ($SmTiO_3/SrTiO_3/SmTiO_3$) quantum wells are reviewed. In Chapter 2, a brief introduction to relevant experimental setups and techniques is provided, from nano-fabrication procedures for mesoscale devices to our efforts on the application of uniaxial strain at cryogenic temperatures, while at the same time performing transport measurements. In Chapter 3, I summarize our observations of the quasi-particle excitation using voltage or optical disturbances in $SmTiO_3/SrTiO_3/SmTiO_3$ quantum wells in the pseudogap phase. In Chapter 4, results demonstrating the effects of uniaxial strain on superconductivity in quantum wires at the $LaAlO_3/SrTiO_3$ interface created using conductive atomic force microscopy (c-AFM) are summarized. Both hysteretic and non-hysteretic responses to the strain in the system are closely examined. Future research efforts and an outlook for this field are presented in Chapter 5.

Table of Contents

List of Tables

List of Figures

Preface

While this thesis is a summary of my Ph.D. work, it would not have been possible without the support and help from many people.

First, I would like to express my deepest appreciation to my research advisor, Prof. Jeremy Levy, for his guidance and support.

Special thanks for Patrick Irvin, for his mentorship. I'm also grateful to all my labmates for the shared good times and frustrations during my graduate study and research. In particular, Megan Briggemann, Michelle Tomczyk, Arthur Li, Lucy Chen, Qing Guo, Yuhe Tang, Yun-Yi Pai, Dengyu Yang, Aditi Nethwewala, Muqing Yu, Erin Sheridan, and Sayanwita Biswas, as well as the new batch of students.

My experiments can not be done without samples. I want to thank Prof. Chang-Beom Eom's and Prof. Susanne Stemmer's research group for providing high-quality samples. I also want to thank my dissertation committee members, Prof. Tao Han, Prof. Michael Hatridge, Prof. Roger Mong, and Prof. David Waldeck, for their guidance and feedback. Their questions and suggestions is very helpful.

Finally, I want to thank my family and friends for their unconditional love, support, and encouragement. They kept me going through difficult times during my Ph.D. journey.

1.0 Introduction

Superconductivity is one of the greatest discoveries of the past century. It was first discovered in mercury that when the temperature is below a critical value, the resistance disappeared abruptly [1]. Since then, superconductivity has been observed in many other materials, enabling transformative applications in high-efficiency electric power transmission, magnetic levitation devices, magnetic resonance imaging, and superconducting electrical circuits for quantum computation [2]. Research to increase the superconducting transition temperature T_c and understand the mechanism behind superconductivity have been very active for decades, yet these two problems remain unsolved.

Superconductivity is unusual because electrons travel in pairs without resistance, as the Nobel-prize-award-winning Bardeen, Cooper, and Schrieffer (BCS) theory [2] explains it. The electron pairs are known as "Cooper pairs". Since electron carries a negative charge and should repel each other, there must be a net attractive force binding the two electrons together in pairs. Therefore, understanding the origin of electron pairing is pivotal to developing the theory related to superconductivity, and to realizing future applications.

$SrTiO_3$ and $SrTiO_3$-based materials make up a family of superconducting semiconductors that generated strong interests in the science community. This dissertation focuses on studying superconductivity and electron pairing mechanisms in two types of heterostructures in this family: the interface of $LaAlO_3/SrTiO_3$ and $SmTiO_3/SrTiO_3/SmTiO_3$ quantum wells. Not only do these oxide heterostructures provide a platform for studying correlated nanoelectronics, which includes superconductivity, they also intersect with semiconductor electronics, which allows for single-electron control [3]. Especially, the ability to locally control the metal-to-insulator transition at the $LaAlO_3/SrTiO_3$ interface [4] have made it possible for the creation of nanoscale devices, leading to promising applications in quantum information.

Seeking to shed new light on the superconductivity in these materials, this dissertation approaches superconductivity and electron pairing from two angles: the pseudogap state and the external strain modulation.

The pseudogap state is a state with a depletion of single particle (E.g. electron) density of state near the Fermi energy and also a phase that exists right next to the superconducting phase in phase diagrams [5]. The pseudogap phase was first discovered in high-temperature superconductors, such as cuprates [6, 7, 8]. Recently, the phase was discovered in $SrTiO_3$-based quantum wells [9]. Since the properties of unconventional superconductors are largely shaped by competing phases, studying the pseudogap phase in $SrTiO_3$-based quantum wells provides information on electron-pairing, even in a non-superconducting state.

Strain is found to enhance superconducting transition temperature in $SrTiO_3$ films under some conditions [10, 11, 12, 13]. It is a powerful experimental method with the ability to induce ferroelastic or ferroelectric phase transitions [14, 15, 16], which are believed to be linked to superconductivity in $SrTiO_3$. Therefore, experiments probing effects of strain on superconductivity are expected to provide more insights on the superconductors studied. The quasi-1D superconducting nanowire at the interface of $LaAlO_3/SrTiO_3$ [17] is an intriguing system for which effects of strain on transport properties have not been investigated previously. Researches presented in the dissertation fill in the blanks.

In Chapter 1, a review for advances on those topics is provided.

1.1 Properties of $SrTiO_3$

1.1.1 Lattice structures of $SrTiO_3$

Properties of $LaAlO_3/SrTiO_3$ heterostructures arise primarily from the substrate $SrTiO_3$, one of the most celebrated substrates [3]. $SrTiO_3$ is a known multiferroic, exhibiting ferroelasticity [18, 19, 20, 21] and paraelectricity [22, 23] that are on the verge of a paraelectric-ferroelectric quantum phase transition [24].

$SrTiO_3$ has a perovskite crystal structure [26]. At room temperature, $SrTiO_3$ has an ideal cubic unit cell (space group Pm3m), consisting of four TiO_6 octahedra surrounding a Sr atom, as shown in Figure 1 (a). It has a lattice parameter of $a = 0.3905$ nm. Sr atoms are located at the vertices of the cube, and one O atom each sit at the center of six faces of the cube. At

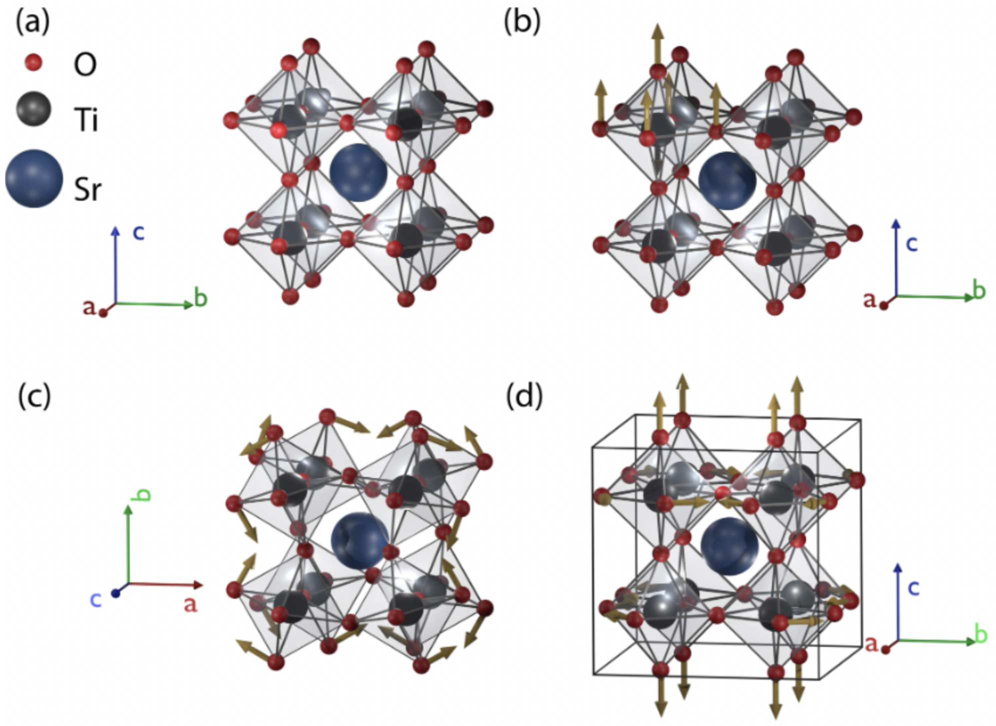

Figure 1: (a) The cubic unit cell of $SrTiO_3$ at room temperature. (b) and (c) FE displacement (b) and AFD distortion (c) in the phase transition at around 105 K. (d) The tetragonal unit cell at below 105 K. Figure adapted from Ref. [25].

low temperature or under applied stress, $SrTiO_3$ undergoes symmetry-breaking structural transitions and the following distortions occur: (1) Ferroelectric-type (FE) displacement, which is the polar displacement between cations and anions, causing built-in polarization (Figure 1 (b)); (2) anti-ferrodistortive transition (AFD), where the oxygen octahedra TiO_6 rotates in opposite directions (Figure 1 (c)). Generally, AFD transition occurs at around $T = 105$ K, causing the cubic structure changing to a tetragonal lattice structure. After the transition, two lattice vectors contract, and the third one elongates along the rotational axis, as shown in Figure 1 (d). This AFD transition has a rotation angle (Glazer classification $a^0a^0c^-$) $\alpha = 2.1°$, and the c/a ratio changes to 1.00056. Domains with different tetragonal orientations (x-, y- or z-axis) of the tetragonal unit cells can form. Domain structures vary sample by sample. Even within the same sample, domains change after cycling the temperature [21].

Studying ferroelastic domain structures is essential to understanding $SrTiO_3$ because they show strong correlations with electronic properties in the material. Domain walls are likely to be polarized or charged [27], as revealed by scanning SET images [28]. Anisotropic electrostriction creates striped potential modulations and thereby influences electron systems [29]. Moreover, recent research has revealed enhanced channels of conductivity at domain walls [29] and an enhancement of the superconductivity transition temperature [30] arises from these domains in $SrTiO_3$ and $SrTiO_3$-based heterostructures. Furthermore, domains can be controlled and moved by electrical gating [31, 28, 32]. This may be attributed to dielectric and elastic moduli differences between domains of different orientations. Domains are also found to be sensitive to strain or pressure, which can directly induce structural changes [16, 33, 34].

1.1.2 Superconductivity of $SrTiO_3$

Doped $SrTiO_3$ is one of the most dilute bulk systems to display superconductivity. Schooley et al. first discovered $SrTiO_3$ to be superconducting at around 250 mK in 1964 [35]. Superconductivity in $SrTiO_3$ has been observed with carrier densities as low as $\sim 10^{15}$ cm^{-3} [36, 37]. This low carrier concentration implies a small Fermi energy, making it an unconventional superconductor, inexplicable by the Bardeen-Cooper-Schrieffer (BCS) theory of superconductivity. A superconducting transition temperature - carrier concentration phase diagram that showcases a superconducting dome, with carrier densities ranging between $\sim 10^{17}$ - 10^{21} cm^{-3} has been reported [38, 35]. In Figure 2 (a), an example of the phase diagram is given, combining data from $SrTiO_3$ samples treated with O reduction and Nb doping [38, 35]. Lower carrier concentrations (data points plotted with black squares) are achieved by Nb doping, while higher concentrations (data points plotted with white hollow squares) are achieved by oxygen reduction. This phase diagram shares essential features with multiple quantum materials, such as high transition temperature superconductor cuprates [39], motivating researchers to study $SrTiO_3$ as a model superconductor system.

The co-existence of interesting electronic properties including superconductivity and ferroelasticity in $SrTiO_3$ is particularly intriguing. Ferroelastic domains in X, Y or Z directions are formed in $SrTiO_3$ after a cubic-to-tetragonal phase transition below 105 K (Section 1.1.1). Enhanced conductivity along ferroelastic domains walls is observed with scanning single electron (SET) transistor microscopy [28] and superconducting quantum interference device (SQUID) microscopy [40]. The SET experiment also found different surface potentials in the ferroelastic X, Y, Z domains, arguing that Z domains are more conductive than X or Y domains. Furthermore, the ferroelastic domains have been shown to play an important role in superconductivity and the electron pairing mechanism [17, 30] (Section 1.2.2).

There has also been evidence for multiple Lifshitz transitions (marked by dashed lines in Figure 2 (a)) [41] and proximity to a ferroelectric quantum critical point. The latter led to a series of studies to experimentally tune superconducting $SrTiO_3$ through a ferroelectric phase transition, by electric field [42], hydrostatic pressure or strain [43, 44, 45, 15], cation (Ca, La) or oxygen isotope substitution [46, 47, 48]. The results led to speculations that quantum ferroelectric fluctuations near the quantum critical point are responsible for the superconductivity [49].

The nature of the superconductivity and electron pairing in $SrTiO_3$ has remained enigmatic for more than half a century since the discovery of superconductivity in $SrTiO_3$. The three most discussed theories are: (i) long-range electron-phonon interaction, which was put forward by Gurevich, Larkin, and Firsov (GLF) [50] and replaced the role of the Debye frequency w_D in the BCS theory by the longitudinal optical phonon frequency, w_L; (ii) soft bosonic modes, which could couple to the states at the Fermi surface and provide a possible pairing glue near quantum critical points; (iii) inter-valley phonons, although this is typically a small contribution to the pairing force [51, 52].

1.1.3 Strain effects on superconductivity in $SrTiO_3$

Strain is one of the several mechanisms that can cause structural changes in $SrTiO_3$, for example, induce incipient ferroelectricity and displace ferroelasic domain boundaries [16, 33, 34, 15, 54]. Therefore, it is a powerful experimental tool to probe superconductivity. Strain

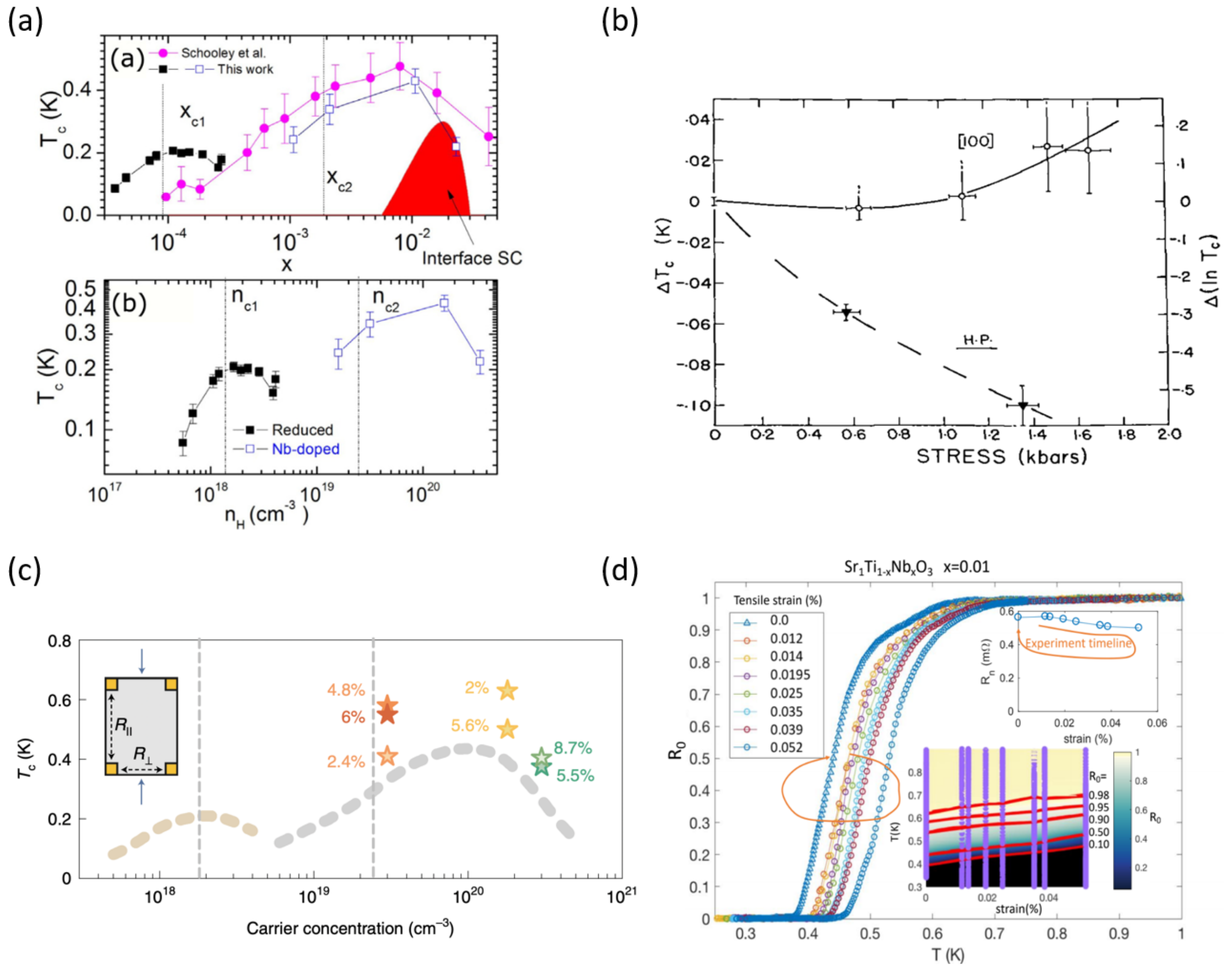

Figure 2: (a) Superconducting dome: the critical temperature T_c - carrier concentration phase diagram of doped $SrTiO_3$, adapted from Ref. [38], Figure 2. (b) T_c in $SrTiO_3$ is shifted by the hydrostatic pressure and the uniaxial pressure along [100] direction. Figure adapted from Ref. [12], Figure 9. (c) Superconducting phase diagram of the undeformed $SrTiO_3$ in dashed lines, with the enhanced T_c measured from plastically deformed $SrTiO_3$ samples created by applying hydrostatic pressure. Figure adapted from Ref. [53], Figure 4. (d) The application of minute external uniaxial strain enhanced T_c in Nb-doped $SrTiO_3$. Figure adapted from Ref. [10], Figure 2.

is also a central topic studied in this thesis (Chapter 4). We start with a summary of the milestones in the literature that provide the necessary background required to set up the problem of strain effects on $SrTiO_3$.

Experimental works have demonstrated the interplay between strain and superconductivity via externally-applied stress. In 1969, Pfeiffer et al. observed decreasing T_c under hydrostatic pressure while witnessing both increases and decreases for compression along the [100] crystallographic axis [11, 12], as shown in Figure 2 (b). In $SrTiO_3$ crystals plastically deformed by extreme pressure, enhanced superconductivity was observed along with signatures of ferroelectric fluctuations (Figure 2 (c)) [53]. Recent technological advances have enabled the application of tensile strain at cryogenic temperatures [55, 56]. It has been discovered that a minute uniaxial tension of 0.05% induced a striking 50% increase in critical temperatures in Nb-doped $SrTiO_3$ (Figure 2 (d)) [10]. These intriguing results motivated the experiments in Chapter 4, in which we investigate the effects that external uniaxial strain has on superconductivity in 1D nanowire devices in $LaAlO_3/SrTiO_3$.

Another widely-used method to apply the strain involves growing epitaxial thin films, including heterostructures, superlattices, or micromembranes [57, 58, 59]. These materials continue to be discussed in detail in Section 1.2 and Section 1.3. Here, current understandings of the relations between epitaxial strain and superconductivity are shared. When $SrTiO_3$ is grown on top of or below another oxide, it can be compressed or elongated because the lattice constant of the top substrate is dissimilar to the lattice constant of the bottom substrate [60, 61]. Bark et al. grew $SrTiO_3$ thin films on top of various single crystal substrates ($NdGaO_3$, $(La_{0.3}\ Sr_{0.7})(Al_{0.65}Ta_{0.35})O_3$ (LSAT), $DyScO_3$, Si, $GdScO_3$), creating samples with different strains at the interface ranging from -1.21% compression to +1.59% tension. The strain was found to change the carrier concentration and the conductivity of those samples significantly [62]. Both properties are closely linked to the superconductivity. Later, Ahadi et al. [13] observed an increased T_c up to 700 mK in compressively strained Sm-doped $SrTiO_3$/LSAT samples. Besides changing the types of oxides to grow together, varying the top substrate's thickness or growth parameters (E.g. temperature) also influences the epitaxial strain at the interface [63].

Several recent theoretical proposals attempt to bridge between superconductivity and ferroelectric properties, providing a possible explanation for some of the experimental results [64, 65]. Building upon the aforementioned soft phonon mode model near the ferroelectric phase transition, Dunnett et al. predicted a linear dependency of T_c on the uniaxial and bi-axial strain. More specifically, under tension, T_c is predicted to increase, while under compression, T_c is predicted to decrease [64]. This is consistent with observations made by Herrera et al. [10].

1.2 $LaAlO_3/SrTiO_3$ Heterostructures

The fabrication of complex oxide heterostructures is enabled by advances in synthesizing epitaxial materials in the laboratory using various deposition techniques, including pulsed laser deposition (PLD) and molecular beam epitaxy (MBE) (Section 2.1). The interfaces give rise to phenomena absent in the bulk structures and expand the ability to control a variety of properties: carrier density, mobility, ferroelectricity, magnetism and superconductivity [62, 15, 66, 67, 68, 69]. Among heterostructures, the most notable is the interface between $LaAlO_3$ and $SrTiO_3$, which has approximately 3.17% lattice mismatch.

1.2.1 Emergent properties at the $LaAlO_3/SrTiO_3$ interface

One of the $SrTiO_3$-based materials that is studied in-depth in this thesis is $LaAlO_3/SrTiO_3$. The interfacial material is also the most extensively studied conductive $SrTiO_3$-based heterostructure. A two-dimensional electron system (2DES) formed at the interface between the two insulating perovskite oxides was first reported by Ohtomo and Hwang. [59]. The confinement of the electron gas is reported to be within a few nanometers from the interface when samples are annealed in a high oxygen environment after growth, confirming the reduced dimension of conductivity, as shown in Figure 3. $LaAlO_3$ crystalline layers grown on TiO_2-terminated $SrTiO_3$ substrates have a critical thickness of 4 unit cells when the interface switches from insulating to conductive [70]. This interface has exhibited various emerging properties: electric field tunable metal-to-insulator transition when $LaAlO_3$

is at a thickness of 3.4 unit cells [4], electric field tunable superconductivity (Section 1.1.2) [71, 72, 73], Rashba spin-orbit coupling [74, 75], and a large negative magnetoresistance at low temperatures [76, 77].

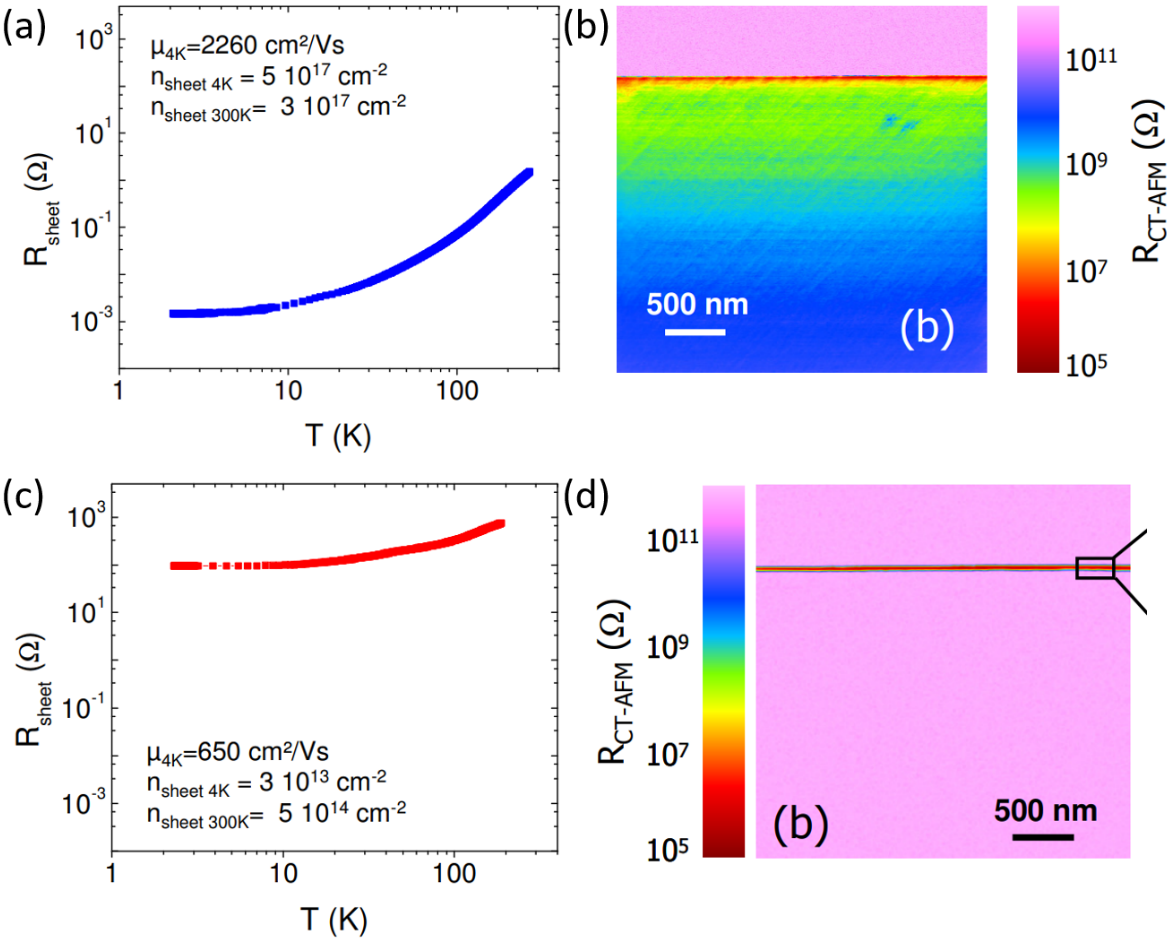

Figure 3: (a) The sheet resistance as a function of the temperature for a unannealed $LaAlO_3/SrTiO_3$ sample. An high sheet carrier density of 5×10^{17} cm^{-2} at $T = 4$ K was observed. (b) Conducting-tip atomic force microscope (c-AFM) resistance mapping for the unannealed sample revealed conductive regions and the electron gas spreading a few microns into bulk $SrTiO_3$ substrates. (c) The sheet resistance for a $LaAlO_3/SrTiO_3$ sample that was annealed in a high oxygen environment after growth. (d) The c-AFM image for the annealed sample shows electrons confined within a few nanometers from the interface. Figures are adapted from the publication by Basletic et al., Figure 3 and Figure 4 [78].

Three dominant mechanisms have been proposed to explain the interfacial conductivity: (1) electronic reconstruction due to the polar discontinuity at the polar non-polar interface, called "polar catastrophe"[79]; (2) unconventional doping of the $SrTiO_3$ by La atoms from the $LaAlO_3$ layers [80]; (3) oxygen vacancies in the $SrTiO_3$ substrates [81]. The polar discontinuity theory, despite being prevalent early on and providing an explanation for some characteristic features (E.g. the critical thickness for 2DES), doesn't explain the conductive non-polar interfaces formed when the $LaAlO_3$ layers are amorphous [82], or (110) and (111) oriented [83, 84]. Moreover, conventional $LaAlO_3/SrTiO_3$ interfaces can be strengthened with a $SrCuO_3$ overlayer to promote the oxygen exchange with the surface and reduce the number of oxygen vacancies, leading to a improved mobility in transport [85]. Despite great efforts in developing theories and hypothesis, the mechanism for the formation of the 2D conductive electron gas remains in question.

There are several ways to tune the interface to go through a metal-to-insulator(MIT) transition: changing the thickness of $LaAlO_3$ layers; applying electrical voltages from a back gate [70] or a conductive atomic force microscope (c-AFM) tip [86, 4]; conducting electron-beam (e-beam) lithography [87], as shown in Figure 4. Especially, the last two methods support local metal-to-insulator transition at nanometer precision. Such extreme nanoscale control holds great promise for oxide-based nanoelectronic devices.

Ferroelastic domains formed at below 105 K in $SrTiO_3$ continue to play an important role in $LaAlO_3/SrTiO_3$ interfaces, by contributing to inhomogeneity at the interface. In the system, it has been demonstrated that ferroelastic domains enhanced the current density along narrow paths oriented along the crystallographic axes [40], induced anisotropic electron transport [29], modulated the superconducting transition temperature T_c [30], coupled to a ferroelectric phase [43], and tuned the magnetic degree of freedom [89, 90].

In addition to $LaAlO_3/SrTiO_3$, a collection of other $SrTiO_3$ heterostructures also host conductive interfaces. For example, the trilayer $SrTiO_3/LaTiO_3/SrTiO_3$ heterostructure is discovered to be conductive with 2D electron gas at the $LaTiO_3/SrTiO_3$ interface and 2D hole gas at the $SrTiO_3/LaTiO_3$ interface, even when there is only one unit cell of $LaTiO_3$ sandwiched in the middle [91, 92]. Combinations of polar/non-polar ABO_3 perovskites, such as $NaAlO_3/SrTiO_3$, $PrAlO_3/SrTiO_3$, and $NdGaO_3/SrTiO_3$, are also fabricated and found to

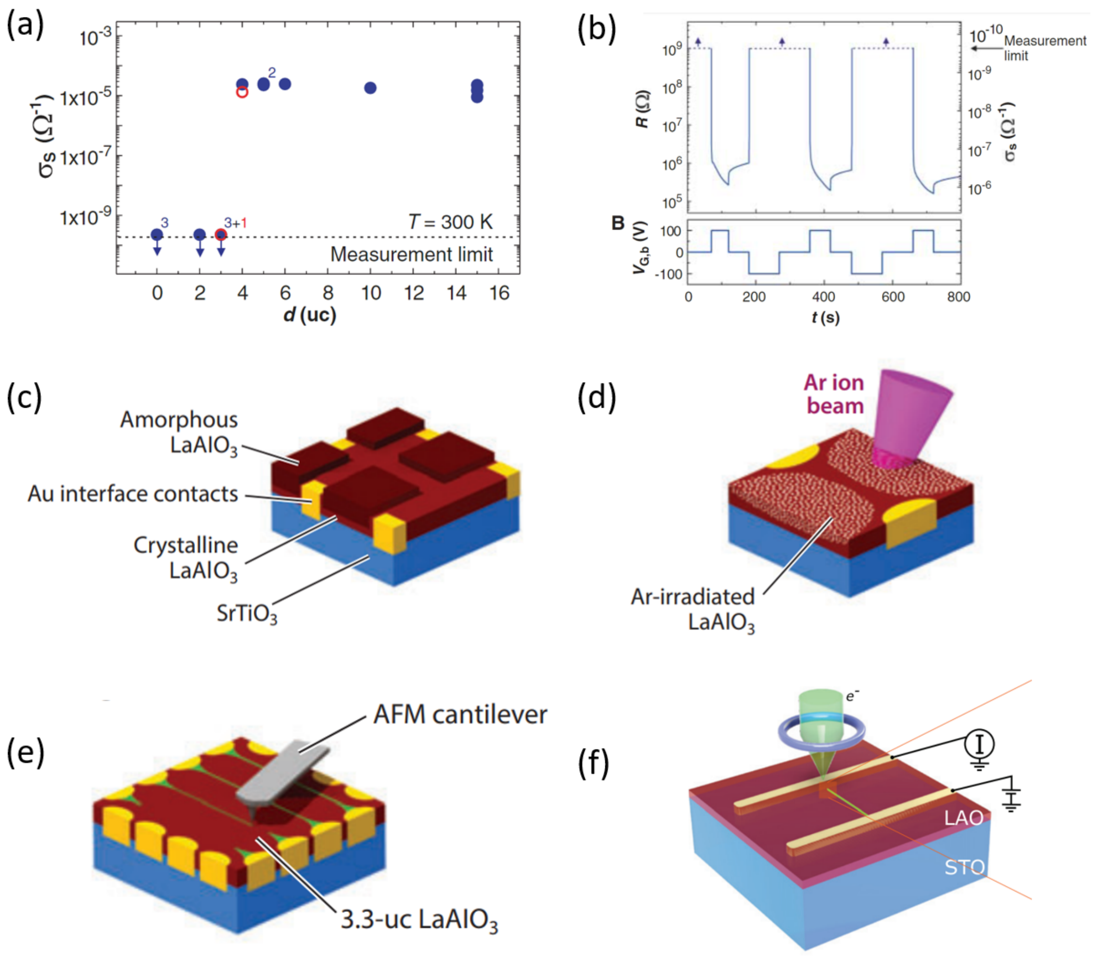

Figure 4: (a) Sheet conductance at the $LaAlO_3/SrTiO_3$ interface at 300 K in samples with different thicknesses for $LaAlO_3$ layers. (b) Sheet conductance switched between $\sim 1 \times 10^{-6}$ ohm^{-1} and unmeasurable high values as the applied back gate voltage switched between -100 V and 100 V. (a-b) adapted from Ref. [70]. (c) Lithographic techniques to engineer $LaAlO_3$ regions to have a mix of crystalline (conductive) and amorphous (insulating) states. (d) Lithography techniques using Argon ions to create local defects to make conductive regions insulating. (e) Lithography techniques using c-AFM tips to apply voltages to make insulating regions conductive. (c-e) are adapted from Ref. [88]. (f) Lithography techniques using e-beam to expose insulating regions to make them conductive, adapted from [87].

support 2DES. These combinations also engineer different epitaxial strain at the interface, providing valuable data to investigate the relation between the strain and electron transport [93]. The $SrTiO_3/GaTiO_3/SrTiO_3$ quantum well is discovered to be a Mott insulator, while the $SrTiO_3/NdTiO_3/SrTiO_3$ quantum well have very high carrier densities. The interface of $SmTiO_3/SrTiO_3$ exhibits similar properties as $LaAlO_3/SrTiO_3$: polar discontinuity at its interface, as well as carrier densities tunable by changing the $SmTiO_3$ thickness, bringing about metal-to-insulator transitions [94]. The quantum well of $SmTiO_3/SrTiO_3/SmTiO_3$ is also investigated for properties including quasistatic antiferromagnetism and the pseudogap phase (Section 1.3) [95, 96, 9]. As novel $SrTiO_3$-based heterostructures continue to be discovered, previous researches in $LaAlO_3/SrTiO_3$ provide much-needed guidance and references.

1.2.2 Superconductivity at the $LaAlO_3/SrTiO_3$ interface

Superconductivity in $LaAlO_3/SrTiO_3$ has many similarities with bulk $SrTiO_3$ that is doped with Nb or by oxygen vacancies. It was found in 2007 that the heterostucture undergoes a superconducting phase transition at temperature below 200 mK [71], as shown in Figure 5 (a). The thickness of the superconducting layer for the initial experiment was revealed to be 10 nm [97], but the thickness can be extended up to 100 nm for the overdoped regime. The Ginzburg-Landau superconducting coherence length was calculated to be 30 - 100 nm based on the temperature dependence of the perpendicular critical field [98, 75, 99]. The coherence length increases with increasing carrier concentration.

The superconducting transition temperature T_c can be controlled by the electric field, forming a dome-shape [71], as shown in Figure 5 (b). Moreover, the dome-shape as a function of superfluid density was also achieved [100]. In the system, researchers have also observed the temperature and gate dependent superconducting gaps and pseudogaps. These features are similar to what has been seen in bulk $SrTiO_3$ [38, 35] and other high-temperature superconductors, such as cuprates [39, 6, 7] . Moreover, electron pairing without superconductivity was observed (Figure 5 (c)) [101, 102], providing evidence favoring the crossover to Bose-Einstein condensation (BEC) regime [5].

At the interface, superconductivity with further reduced dimension from 2D to 1D may be achieved. Nanowires created using c-AFM lithography at room temperature, become superconducting at around 200 mK [4, 17]. Pai et al. [17] created devices with different numbers of nanowires and different conductive channel widths using c-AFM lithography and found that the superconducting critical current, defined as the maximum value of the sustained direct current in the superconducting devices, was independent of the conductive channel width. This striking discovery demonstrated that superconductivity and electron pairing exist at the edges of conductive channels, pointing to the quasi-1D nature of the nanowires.

Since the interface inherits superconductivity from bulk $SrTiO_3$, many hypotheses for the superconducting mechanism for $SrTiO_3$ (Section 1.1.2) are also applicable to the interface. In the special scenario of c-AFM created nanowire superconductors, the ferroelastic domain hypothesis stands out as particularly relevant. Conductive channels created in this method are elongated in the Z direction at room temperature, seeding the formation of ferroelastic Z-oriented domains under $T = 105$ K [103]. The elongation has been imaged at room temperature using piezoelectric force microscopy (PFM) (Figure 18 (b)). The AFM-lithography-induced elongation is likely to arise from the piezoelectric properties of $SrTiO_3$ [104], taking into account the effect of a top-layer $LaAlO_3$ as well [105, 106, 107, 108], or the carrier density modulation.

At low-temperatures, due to the compensation of strain, insulating areas surrounding the conductive channels turn into ferroelastic X- or Y-oriented domains. Therefore, conductive channel boundaries coincide with domains walls, as illustrated in Figure 5 (d), leading to the considerations of the connection between the ferroelastic domains and superconductivity.

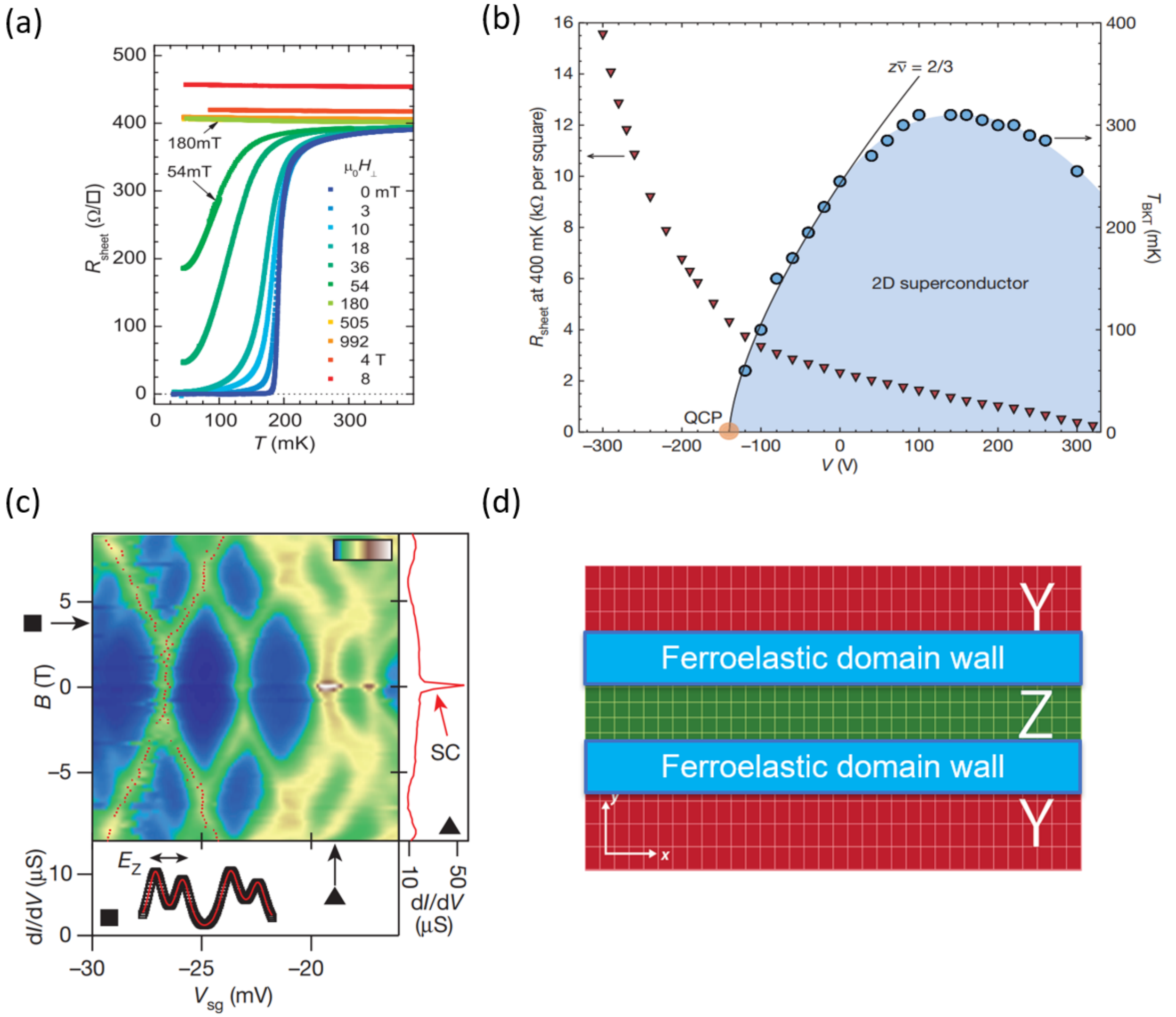

Figure 5: (a) The first observation of a superconducting phase transition in $LaAlO_3/SrTiO_3$ at $T = 200$ mK, adapted from Ref. [71]. (b) Superconducting "dome" in $LaAlO_3/SrTiO_3$, tunable with respect to electric field, adapted from Ref. [72]. (c) Magnetic field dependence of two zero bias peaks in $LaAlO_3/SrTiO_3$ SETs, indicating electron pairing, adapted from Ref. [101]. (d) A diagram showing conductive channels created using c-AFM lithography at the $LaAlO_3/SrTiO_3$ interface, turn into ferroelastic Z domains at low temperatures. Domains walls decorate conductive channel edges. Adapted from Ref. [17]

1.3 $SmTiO_3/SrTiO_3/SmTiO_3$ Heterostructures

1.3.1 Properties of the quantum wells

Combining $SrTiO_3$ with other transition metal oxides produce a group of heterostructures with spectacular properties. It is particularly attractive to study the induced phenomena through interfacial proximity, by combining various perovskites with rich properties. Besides $LaAlO_3/SrTiO_3$, the milestone in the field discusses in the previous section, another heterostructure studied in the research is the quantum wells between antiferromagnetic Mott insulator $SmTiO_3$ and band insulator $SrTiO_3$ (Chapter 3).

In Figure 6 (a), a schematic for the $SmTiO_3/SrTiO_3/SmTiO_3$ quantum wells is shown. It is discovered that a strongly correlated two-dimensional electron liquid is confined in the narrow $SrTiO_3$ layers [109]. Assuming that polar discontinuity at each $SmTiO_3/SrTiO_3$ interface contributes to mobile carriers, the sheet carrier density is deduced to be $\sim 7 \times 10^{14}$ cm^{-2}. In these quantum wells, the proximity effects of antiferromagnetic $SmTiO_3$ induce a nearly isotropic negative magneto-resistance in originally non-magnetic $SrTiO_3$ layers [109]. In thin quantum wells (t_{QW} less than five), 2DES is found to be non-Fermi liquids, as the temperature dependence of the resistance ($R \sim AT^n$) measurements found $n \sim 5/3$ instead of $n \sim 2$ [96, 110] (Figure 6 (b)). Analysis of transverse and Hall resistivity data revealed two distinct scattering rates co-existing in the system, which is another non-Fermi-liquid behaviour known as the separation of transport lifetime (Figure 6 (e)) [110]. For thicker quantum wells (t_{QW} equal or larger than five), the reduction of three-dimensional carrier densities and symmetry-lowering distortions may be the cause for the change of electronic behaviours to Fermi-liquid-like.

Most strikingly, a pseudogap phase, a phase in which the Fermi surface possesses a partial energy gap, is also discovered in thin $SmTiO_3/SrTiO_3/SmTiO_3$ quantum wells [9]. The pseudogap features, revealed in the conductance spectra (dI/dV vs V, Figure 6 (c)) and the normalized conductance spectra ($d\ln(I)/d\ln(V)$ vs V), Figure 6 (d)) diminish with increasing temperature or t_{QW}.

That the intriguing properties listed above all occur near a quantum critical point tunable by the thickness of the quantum wells, suggests that fluctuations can play an important role here. In fact, signatures of large potential and magnetoresistance fluctuations have been directly observed in thinner quantum wells [111].

Moreover, a comparison with ferromagnetic $GdTiO_3/SrTiO_3/GdTiO_3$ quantum wells shows that non-Fermi-liquid features is only present in the $SmTiO_3/SrTiO_3/SmTiO_3$ quantum wells (Figure 6 (b)). Therefore, the electronic and magnetic properties are probably also linked.

1.3.2 Pseudogap phase

The pseudogap phase is one of the most mysterious non-superconducting states, often seen in high temperature superconductors such as cuprates and Bi2212 [6, 7, 8, 112, 113, 114, 115, 116]. As a central puzzle of cuprate superconductors, it is detected as a reduction of the single particle density of states (DOS) near the Fermi energy, often using experimental methods such as the tunneling spectroscopy and the angle-resolved photoemission spectroscopy (ARPES) [113, 9]. The pseudogap phase often appears next to the superconducting phase in phase diagrams, sometimes at temperatures comparable to T_c. According to the BCS-BEC crossover theory, which emphasizes the concept of pairing without superconductivity, a preform-pairs scenario is proposed. Since materials in the pseudogap state can be quite insulating, these electron pairs should be localized [5].

Similar to cuprates, $SrTiO_3$ is also an unconventional superconductor. Therefore, it is not a surprise to see the pseudogap phase in $SrTiO_3$-based materials. Besides the $SmTiO_3/SrTiO_3$ $/SmTiO_3$ quantum wells, pseudogaps or superconducting gaps that are tunable electrically have also been observed in $LaAlO_3/SrTiO_3$ heterostructures (Figure 6 (f)) [117]. Experiments also provided evidence for pre-formed pairs in the normal conductive state in $LaAlO_3/SrTiO_3$ [101, 102], favoring the BEC-BCS theory. Since both $LaAlO_3/SrTiO_3$ and $SmTiO_3/SrTiO_3/SmTiO_3$ quantum wells inherent a lot of properties from the shared $SrTiO_3$ component, it is natural to consider that pre-formed electron pairs may exist in the pseudogap state in $SmTiO_3/SrTiO_3/SmTiO_3$ quantum wells as well.

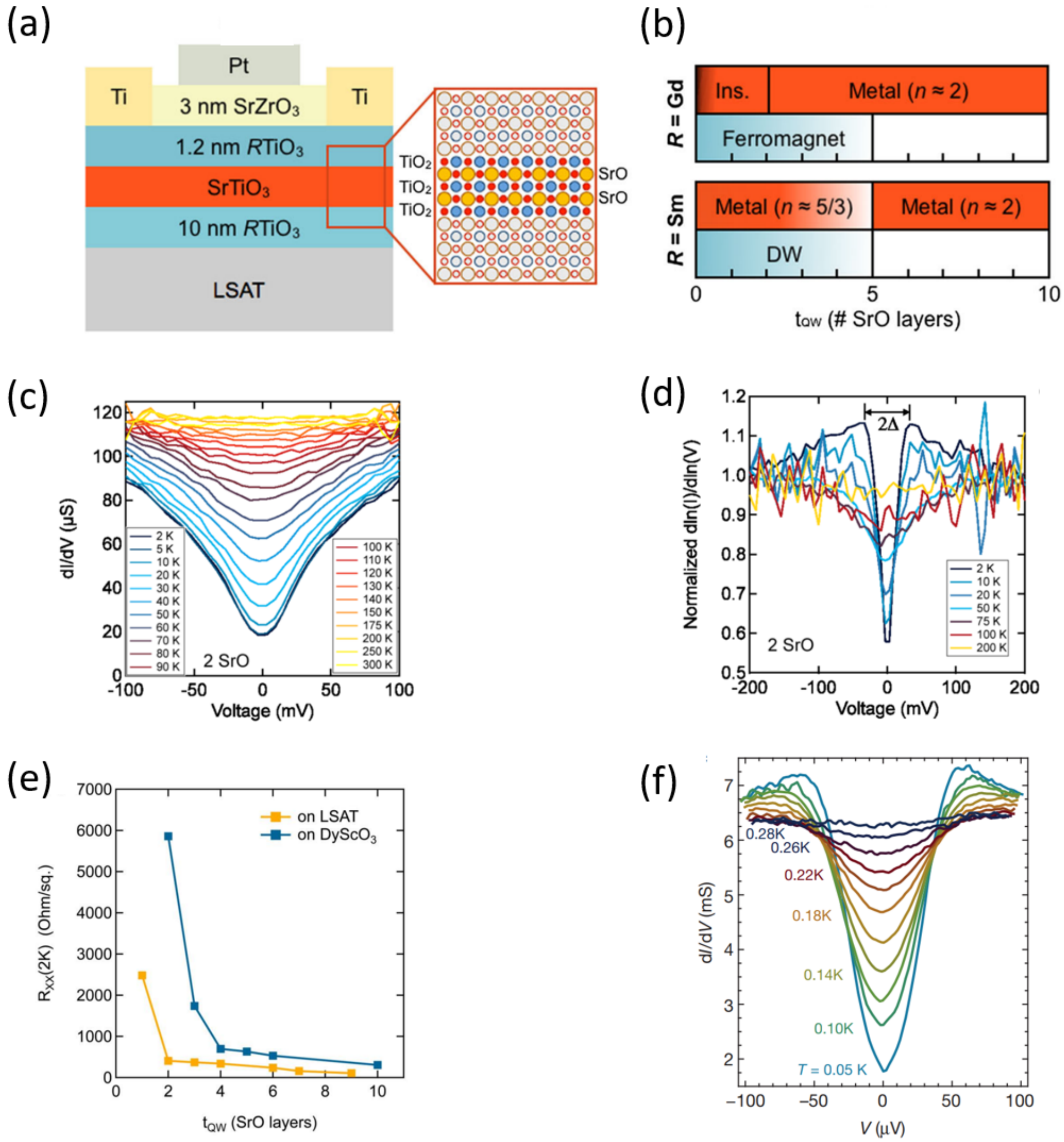

Figure 6: (a) Cross sectional view of narrow $SrTiO_3$ quantum wells confined in insulating $RTiO_3$ barriers (R = Sm or Gd). (a-d) are adapted from Ref. [9]. (b) Phase diagram of $GdTiO_3/SrTiO_3/GdTiO_3$ quantum wells (top) and $SmTiO_3/SrTiO_3/SmTiO_3$ quantum wells (bottom) as a function of $SrTiO_3$ thickness, measured in terms of the number of SrO layers t_{QW}. For $SmTiO_3/SrTiO_3/SmTiO_3$ quantum wells, (c) and (d) are the conductance spectra (dI/dV) and the normalized conductance spectra [$d\ln(I)/d\ln(V)$ vs V) as a function of temperature for $t_{\mathrm{QW}} = 2$. (e) shows the low temperature residual sheet resistance R_{XX} $(2 \cdot \mathrm{K})$, adapted from Ref. [118]. (f) Conductance spectra in $LaAlO_3/SrTiO_3$ interface reveals a similar superconducting gap observed with gap width $\Delta = 100$ μeV, adapted from Ref. [117].

2.0 Experimental techniques

2.1 $LaAlO_3/SrTiO_3$ sample preparation

2.1.1 Sample growth

The $LaAlO_3/SrTiO_3$ samples used in the experiments are grown using pulsed laser deposition (PLD) by our collaborators Ki-Tae Eom, Jung-woo Lee, and Hyungwoo Lee in Prof. Chang-Beom Eom's research group at the University of Wisconsin-Madison [107]. We use $SrTiO_3$ single crystals commercially available from vendor MTI corporation. There, high purity $SrTiO_3$ powder is turned into single crystal boules through the Verneuil (flame-fusion) process, as shown in Figure 7 (a) [119]. The vendor also epi-polishs single crystals into pieces in size 5 mm × 5 mm × 100 μm before shipping to us. The 100-μm-thick $SrTiO_3$ substrates, which is the thinnest type commercially available, are chosen for the research in order to achieve maximum uniaxial strain (experiments described in Chapter 4).

At Dr. Chang-Boem's research group, the following procedures are performed to grow $LaAlO_3$ on top of $SrTiO_3$ and to determine edge orientations for samples.

To obtain TiO_2-terminated substrates, the $SrTiO_3$ substrates are etched by buffered hydrofluoric acid (HF) for 1 min and then annealed at 1000°C for six hours to make the surface atomically smooth with single-unit-cell height steps. This step is a prerequisite for the reproducible layer-by-layer growth with atomic precision with PLD and also plays a significant part later in the formation of 2DES at the interface, after $LaAlO_3$ is deposited. The HF treatment method used was developed by Kawasaki et al. [120] and Koster et al. [121].

A thin layer (3.4 unit cell) of $LaAlO_3$ is grown on top by PLD, which is the primary method for growth for this material, although molecular beam epitaxy (MBE) [122], metal-organic chemical vapor deposition (MOCVD) [123], and sputtering [124] can be used as well. PLD is a physical vapor deposition technique where a high-power pulsed laser beam is focused inside a vacuum chamber to strike a target of the material that is to be deposited

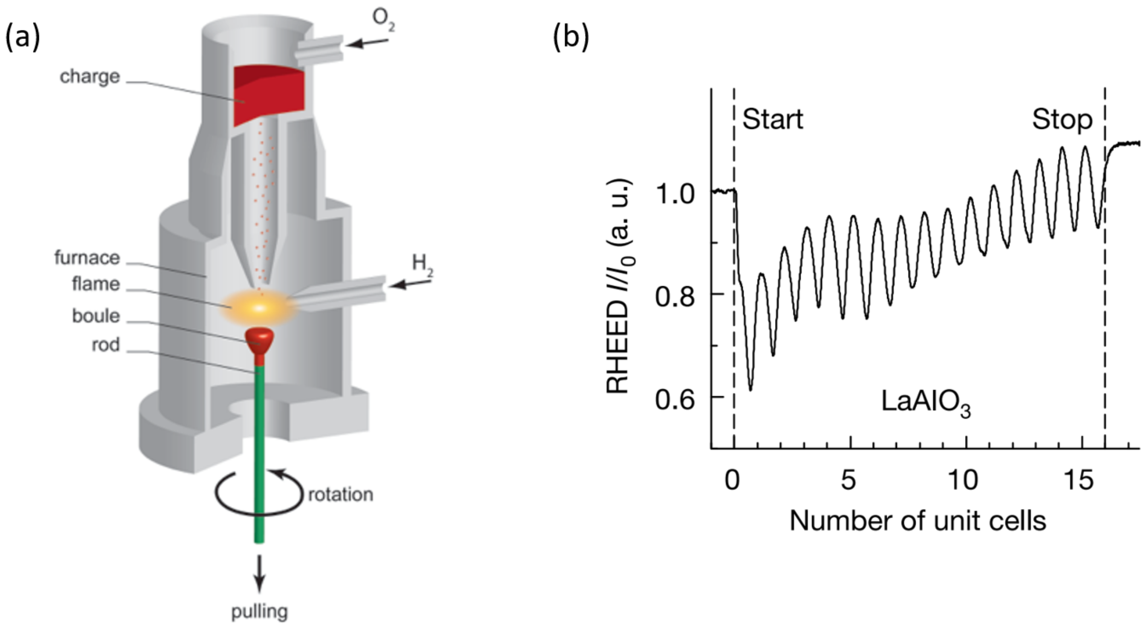

Figure 7: (a) A diagram showing the Verneuil process that transforms powders into $SrTiO_3$ single crystal substrates. Picture credit to: MTI Corporation. (b) RHEED intensity oscillations of the specular reflected beam for the growth of $LaAlO_3$ directly on the TiO_2 terminated $SrTiO_3$ (001) surface. Figure adapted from Ref. [59].

[125]. Additional growth parameters include the growth temperature at 550 °C and the background oxygen pressure at 10^{-3} mbar. $LaAlO_3$ thickness is chosen to be 3.4 unit cell, optimal for a subsequent process of c-AFM lithography (Section 2.3.2). For additional details of the growth technique, refer to [70]. After growth, the sample is slowly cooled back down to room temperature.

The thickness of $LaAlO_3$ during growth is determined by reflection high-energy electron diffraction (RHEED), as depicted in Figure 7 (b) [127]. The layer-by-layer growth is reflected in the oscillations of the intensity of the specular spot of RHEED. The maximal intensity happens when the surface is smooth, indicating a fully-covered surface or a completed layer. Furthermore, the development of high-pressure RHEED technique allows for operations in an environment with higher base pressure, thus enabling the monitoring of the growth of

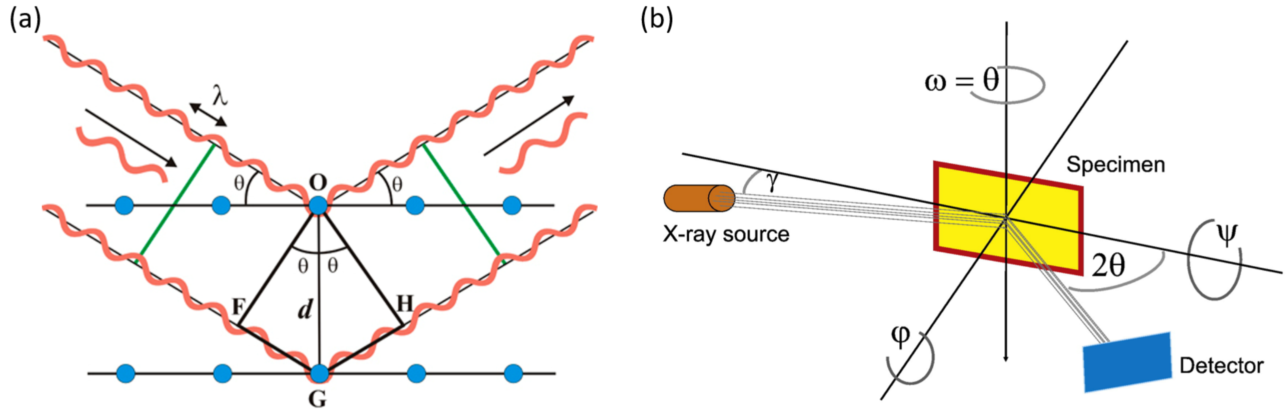

Figure 8: (a) Diagram explaining the Bragg's law. In lattices, atoms form parallel planes, with a distance d in between. The distance determines a specific angle θ when constructive interference occurs, identified as a peak in diffraction signals. Picture credit to: the International Union of Crystallography (IUCr). (b) Schematic picture of the definition of the different angles used in the text for description of the various scans, adapted from Ref. [126].

oxide heterostructures.

Since some $SrTiO_3$ substrates come in random crystallographic orientations, High Resolution X-Ray Diffraction (HRXRD) is utilized to determine the edge orientation for each sample. It is imperative to know the edge orientation, or the direction for the [100] plane. This is due to its association with ferroelastic domain orientations at low temperature (Section 1.1.1) and the way crystal cleaves when scribed (Section 2.1.3). According to the Bragg Equation, for (110) plane in $SrTiO_3$, the $(\theta, 2\theta)$ angle is $(16.198°, 32.3964°)$ for X-rays generated from a copper source [128, 129]. This means that if the angle between the incoming X-ray beams and the (110) planes is 16.198°, the path difference for waves reflected by adjacent lattice planes be an integer multiple of the wavelength of the X-rays λ, resulting in a peak in diffraction signals. For each sample, our collaborators aim the X-ray beam to the edge of the sample and collect diffraction signals. Our collaborators start from $(\theta, \psi) =$

(16.198°, 45°), take a rocking curve in θ between 15.5° and 16.5°, then scan ϕ between -45° and +45°, until a strong peak signal is found. At this time, it is implied that the $SrTiO_3$ (100) direction is parallel to the incoming X-ray beams.

2.1.2 Sample processing

One of the challenges with transport experiments on the $LaAlO_3/SrTiO_3$ interface involves the making of good electrical contact from the wirebond pads to the 2DES at the interface. One part of my Ph.D. research is processing the samples before c-AFM lithography. The following sample processing recipe is adapted from the previous work of Daniela Bogorin, Mengchen Huang, and Jianan Li [130] from the University of Pittsburgh.

1. Initial cleaning: the sample is immersed in acetone and isopropy alcohol (IPA) respectively and placed in an ultrasonic cleaner to remove the surface contaminants or vacuum grease on the back of the sample. Deionized water (DI water) should be prevented from touching the $LaAlO_3$ surface in this and later steps, because H_+ ions can be absorbed by the sample surface, making it difficult to perform c-AFM lithography later.

2. Photolithography: the sample is patterned with standard Ultraviolet (UV) photolithography procedures using a mask aligner or with a direct laser writer (DLW). The latter approach has a slightly higher resolution of 2 μ m.

Firstly, the sample needs to be covered with photoresists uniformly and spin-coating is the standard technique. When the sample is spinning at an angular speed in the range between 1000 rpm and 6000 rpm, the liquid photoresist on the sample surface spread out. The higher the angular speed of spinning, the thinner the photoresist layer be. The eventual thickness of photoresist also depends on the viscosity, concentration of the solvent, and surface roughness. After spin-coating, the sample is baked at 95 °C to evaporate the solvent in the photoresist to make it solid. The recipes used in this research (spinning speed and time as listed in Table 1) are optimized to make the AZ4110 layer as thin as $1.1\mu m$ and match the subsequent UV exposure recipe. Additionally, AZ4620 is used as glue, attaching a sample to a Si wafer, to replace the use of normal double-sided tapes, so its thickness doesn't matter as much in the application. Because AZ4620 is solvable in acetone, by immersing in acetone

Table 1: Spin-coating conditions for photoresist AZ4620 and AZ4110.

Photoresist	AZ4620	AZ4110
Spinning speed	4000 rpm	4000 rpm
Spinning time	30s	30s
Baking temperature	95°C	95°C
Baking time	300s	60s
Thickness	–	1.1 μm

for 10 min, the sample can be separated from the wafer easily and safely.

Secondly, the sample is selectively exposed to the UV light, which change the solubility of the photoresist . AZ4620 and AZ4110 are both negative photoresists, which means exposed regions are easier to be dissolved in developer solvents and be removed. Samples can be exposed with two different methods: mask exposure (Suss MJB3) or direct laser writing (Heidelberg MLA100 Direct write lithographer). The latter has the advantages of high resolution and convenience to operate over the former.

Direct laser writing usually contains a UV laser source, a red light source to provide guidance for alignment, a spatial light modulator to convert the design to light patterns, a series of lenses to expand and focus light, beam splitters, and a CCD that monitors the sample surface in real-time. Part of the optical setup is shown in Figure 9 (a). UV light with wavelength $\lambda = 405$ nm is generated from a laser diode. Design data is created using software such as LayoutEditor and input into the computer, which also controls CCD imaging, laser power, sample movement, and laser alignment. Therefore, processes such as laser alignment and dose control are highly automated.

Thirdly, the sample is immersed in a buffered base solution to wash away exposed parts of the photoresist. The process is called developing. In this research, AZ400K (potassium borate), diluted with DI water by a 1:4 ratio, is used for developing. Accordingly, the optimal time for developing is between 2 min to 2 min 30 s before the sample is washed with DI

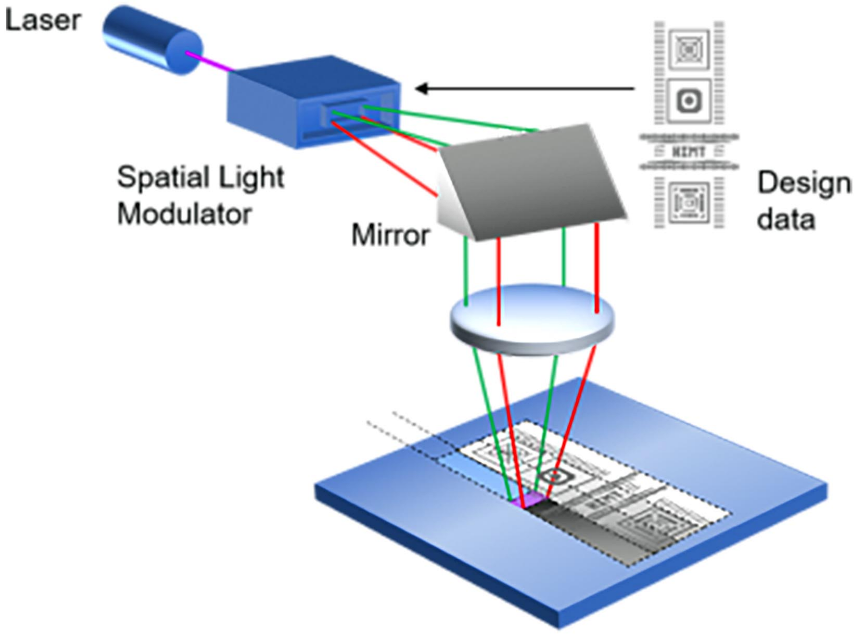

Figure 9: (a) Diagram of the working principle of the Heidelberg Direct laser writer, which is an instrument used for the maskless laser lithography technique. A spatial light modulator (SLM) is used to project light encoded with design data onto the wafer. The whole image may consist of many individual images in stripe form. Typical dynamic or programmable masks imported into the system have file extensions such as GDS, AOM, GLV, and DMD. Picture credit to: Heidelberg Instruments.

water to remove excessive developer and then blown dry. A variation in the developing time could cause the resulting pattern to deviate from the design, so the time must be carefully controlled. Images of samples post UV exposure and developing is shown in Figure 10 (a-c).

3. Oxygen plasma: contaminants introduced by processes 1 and 2 are stripped away with a highly versatile plasma-etching instrument (Model March PX-500 Plasma Asher). This step is repeated each time after photolithography and liftoff, which be discussed later in the same section. Some parameters used are: gas = oxygen, Power = 100 W, time = 30 s.

4. Ion milling: the sample is bombarded with Ar+ ion flow to carve into the material, exposing the interface, in regions not protected with the photoresist.

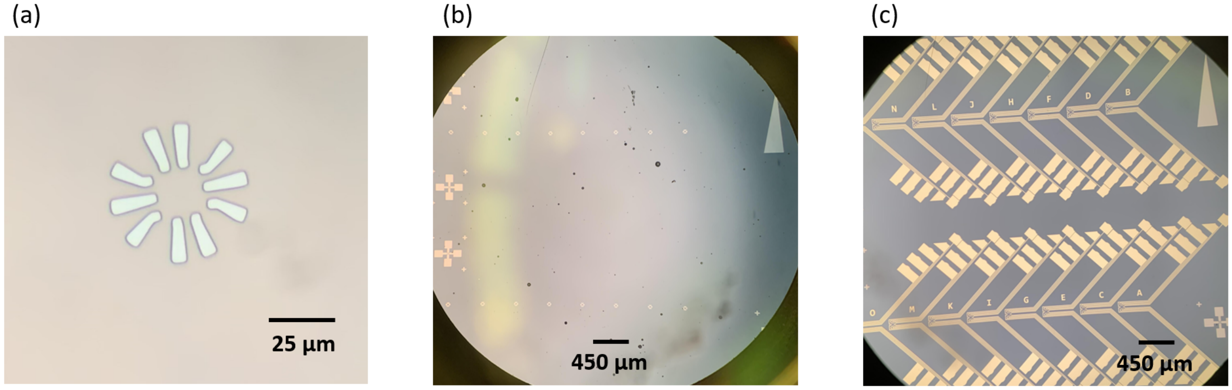

Figure 10: (a) Image of photolithography-created pattern for metal fingers in a typical canvas for c-AFM writing. Light brown regions are covered by hardened photoresist, while light blue regions have the $LaAlO_3$ surface exposed. (b) Image of a sample under an optical microscope, after depositing the first laser of metal, containing alignment markers and Ti/Au metal fingers in direct contact with the interface of $LaAlO_3/SrTiO_3$. The sample is patterned with 16 canvases (16 groups of electrodes), along with cross-shaped markers used for aligning the sample in the Direct laser writer. (c) Image of the sample after depositing the second layer of metal, containing wire-bond pads connected to metal fingers.

In general, there exists three methods for etching: wet-chemical solutions using reactive chemical solutions (such as HF, HCl) [131, 132], plasma etching using reactive gas molecules (such as O_2, SF_6, etc.) [133, 134], and ion milling using accelerated ionized argon plasma to bombard sample physically [135, 136]. Ion milling works well on most inorganic materials, including $LaAlO_3/SrTiO_3$ and allows for directional control. Thus, it's the most suitable approach for the step.

5. Deposition: 4 nm of titanium (Ti) and 25 nm of gold (Au) are deposited by electron-beam evaporation or sputtering to make electrodes. The making of electrodes is divided into two parts: (1) making tiny metal fingers in direct contact with the interface, as depicted in Figure 10 (b); (2) making large metal pieces connecting metal fingers to wire-bond pads (Figure 10 (c)). Therefore, step 1-6 are executed at least twice on a sample, one for each

part.

In the research, both ion milling and metal deposition take place inside the Plassys Electron Beam Evaporation system. As shown in Figure 11, a beam of electron generated from a heated tungsten filament is accelerated by a high voltage. The beam changes direction in the magnetic field and eventually hits a target material anode. Heated up by electrons, atoms from the target turn into gas, move upwards, and re-condense onto sample surfaces. After the deposition time elapsed, the shutter is closed to stop excess metal atoms getting into the upper chamber.

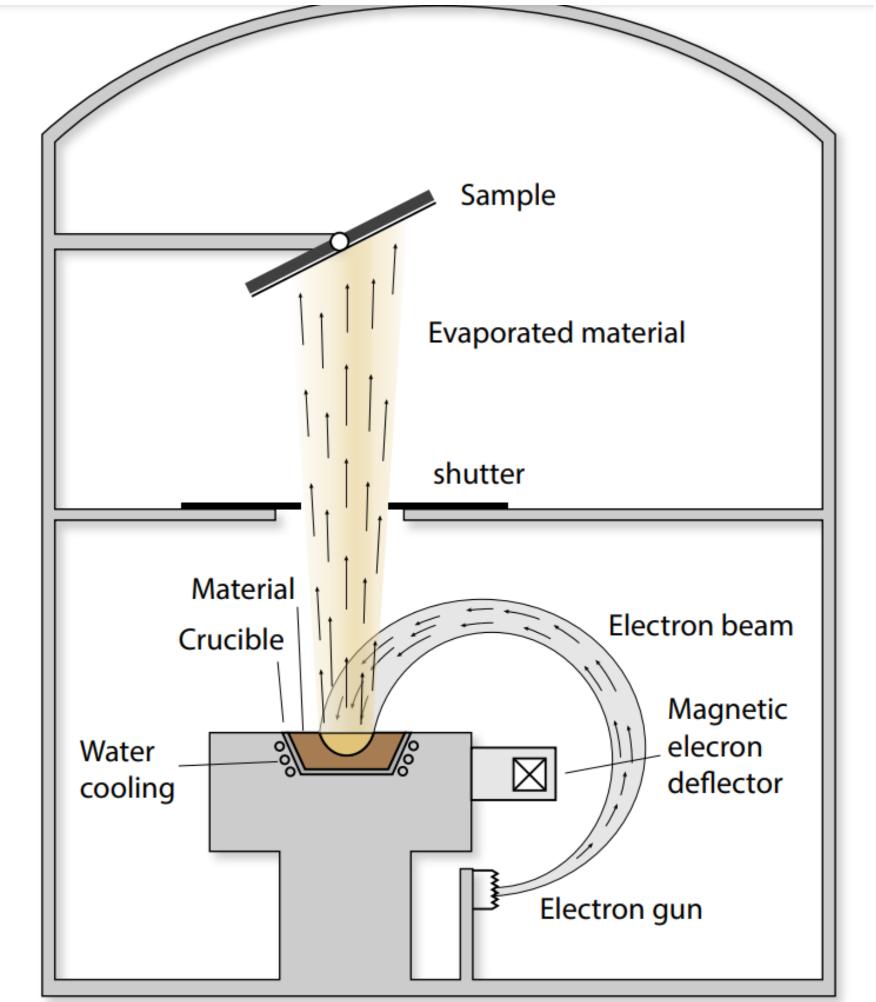

Figure 11: Diagram of a electron-beam evaporation system, adapted from Ref. [130].

6. Lift-off: the sample is immersed in acetone for greater than 4 hours to remove the

excessive metals covering the photoresist. Then, IPA and acetone are utilized as photoresist solvents, and the excessive metals are shed away in the ultra-sonic cleaner similar to initial cleaning. In the final step, Oxygen plasma is repeated so that the sample surface is clean enough for atomic steps to be visible in AFM imaging afterward. Prolonged plasma ashing on the sample unprotected by a photoresist layer can also affect the electrical transport properties of the interface.

2.1.3 Sample scribing and cracking

Scribing techniques are used to create minor distortions on thin $LaAlO_3/SrTiO_3$ plates, enabling controlled breaking of the plate in half [137]. An older technique is the mechanical scribing, which utilizes a diamond indenter to scratch the surface of the plate, causing regional stress and a minute deflection of the sample away from the scribed side. A newer technique is the laser scribing, which utilizes laser pulses that are powerful enough to melt a small block of the material. The laser scribing has an advantage in control precision and speed, although it requires specialized equipment, depending on the types of materials to cut.

In this research, we employed the mechanical-scribe-and-cleave strategy to split processed samples into two pieces roughly 2.5 × 5 mm in size, in order to maximize the extent of uniaxial stress on each piece of sample in later processes. A robot arm (commercially available mode Rotrics DexArm) is adopted to press the diamond indenter on the sample surface and trace it along a desired line over and over, as shown in Figure 12 (a). Ideally, the line should be parallel to a crystallographic direction of the $SrTiO_3$ substrate. The vertical load or the force pressing down on the sample needs to be large enough to cause plastic deformation and deepen the crack marks [138], as shown in Figure 10 (b), but also not too large that the indenter gets stuck in the sample and break it in undesired ways. The utilization of the robot arm instead of human operations makes scribing automatic and highly repeatable.

After scribing creates a weak point on the sample, cleaving is the second step to breaking a sample in half. Applying tensile stress in the vicinity of the weak point causes the sample to break at the point. Since $SrTiO_3$ substrate is a single crystal, the broken edges tend to

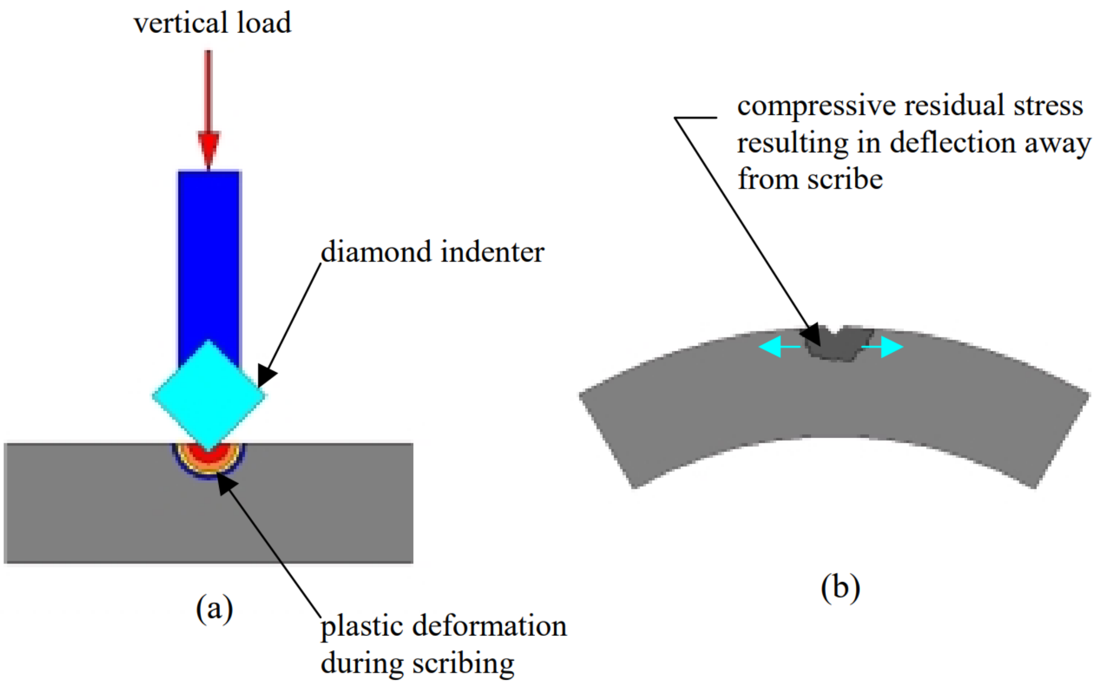

Figure 12: (a) The diamond indenter sliding over a brittle material with a suitable verticle force to cause plastic deformation. (b) Applying a tensile stress near the vicinity of the weak point can cause the sample to break. Diagram adapted from Ref. [137], Figure 2.1.

be a crystal plane and have a mirror finish.

2.2 $SmTiO_3/SrTiO_3/SmTiO_3$ sample preparation

2.2.1 Sample growth

$SmTiO_3/SrTiO_3/SmTiO_3$ quantum well films used in the research are grown on $(La_{0.3}Sr_{0.7})(Al_{0.65}Ta_{0.35})O_3$ (LSAT, $a = 3.96$ $\mathring{A}$) substrates by hybrid molecular beam epitaxy (MBE), by our collaborators in Prof. Susanne Stemmer's research group at University of Wisconsin Madison. As shown in Figure 13, the quantum well structure consists of (from bottom to top) a 10 nm-thick layer of $SmTiO_3$, a 2-u.c.-thick layer of $SrTiO_3$, a 1.2 nm-thick layer of $SmTiO_3$, and a 3-nm thick layer of $SrZrO_3$.

The growth method, detailed in [139, 140], is a widely-adopted methods for the growth of a family of films with rare earth elements including $GdTiO_3$, $GdScO_3$, $LaTiO_3$ on $SrTiO_3$ thin films [141, 142, 143]. Both $SmTiO_3$ and $SrTiO_3$ layers are co-deposited in ultra-high vacuum (i.e., 10^{-10} torr) and a relatively high growth temperature ($> 700°$), using effusion cells as sources for Sm atoms and Sr atoms as well as metal-organic precursors for Ti atoms and O atoms. The average quantum well width is specified by the number of SrO planes contained in $SrTiO_3$ layers, without considering TiO_2 planes. The width can be controlled with atomic layer precision by either estimating the growth time if the growth speed is known, or monitoring during growth with reflection high-energy electron diffraction (RHEED). Armed with advanced growth techniques, high-quality samples with even a single SrO layer sandwiched between $SmTiO_3$ barriers can be obtained. In the research, we use samples containing 2 SrO layers, which are discovered to exhibit the most striking pseudogap behaviors [118]. Although MBE offers atomic layer control, because of the existence of surface steps and substrate miscut, quantum well thickness variations of atomic planes may occur in different regions of a sample.

In the quantum well heterostructure, $SrTiO_3$ layers are conductive, while $SmTiO_3$ layers are insulating. Wide-band-gap $SrZrO_3$ is added on top as a tunneling barrier for top-gate devices (Section 2.2.2.1). At each $SrTiO_3/SmTiO_3$ interface is a TiO_2 layer, so a carrier density of $\sim 3.4 \times 10^{-14}$ cm^{-2} to compensate for the interfacial polar discontinuity can be deduced. Considering that a quantum well contains two such interfaces, a 2DES with $\sim 6.8 \times 10^{-14}$ cm^{-2} mobile carriers are spatially confined in the $SrTiO_3$ layers [144].

2.2.2 Sample processing

In the research, devices with two types of geometry are tested on $SmTiO_3/SrTiO_3/SmTiO_3$ quantum well samples: the top gate and the Hall bar geometry. One essential part shared by the fabrication of both devices is making interface electrodes, which are ohmic contacts to the 2DEL in $SrTiO_3$, as illustrated in six steps in Figure 13. Techniques similar to procedures

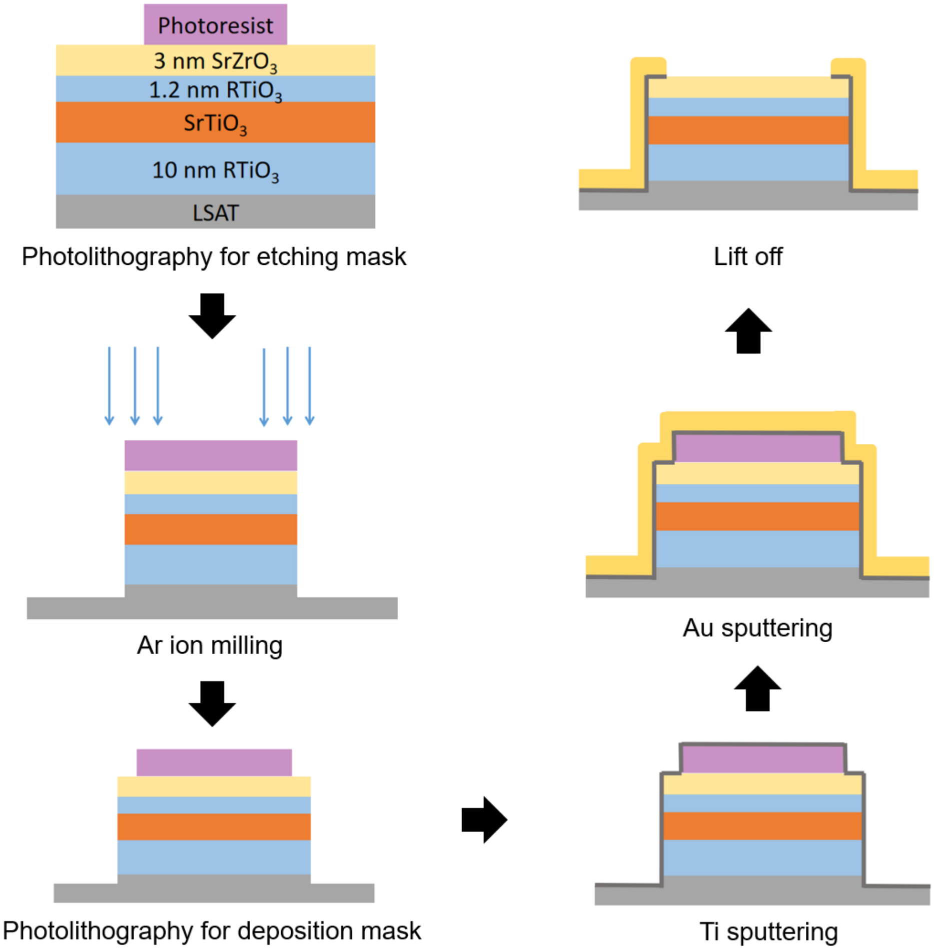

Figure 13: Six-step nanofabrication processes of interface electrodes in direct contact with 2DES in the $SmTiO_3/SrTiO_3/SmTiO_3$ quantum well structures.

on $LaAlO_3/SrTiO_3$ samples described in section 2.1.2 are adopted.

Firstly, photolithography is performed so that selected areas of the sample are protected by photoresist. Then, the sample is bombarded under Argon ions until 60 nm-thick material in unprotected areas is etched away, leaving the $SrTiO_3$ layers in the remaining quantum well structure open from the side. Next, photolithography is repeated with a different mask corresponding to the pattern for interface electrodes. Ohmic contacts are 4 nm-Ti and 50 nm-Au deposited in the Plassys Electron Beam Evaporation system. Finally, the sample is immersed in Acetone for longer than 4 hours to dissolve photoresist and lift off excess metal.

2.2.2.1 Top gate geometry

Tunnelling spectroscopy has been one of the most potent tools in investigating superconducting gaps and pseudogaps [113, 145, 112, 8]. In the research, top-gate geometry devices are designed as a standard superconductor-insulator-normal metal (SIN) junction, as shown in Figure 14 (a). The purpose is to conduct tunnelling experiments to map the electronic density of states near the Fermi level.

The geometry has an interface electrode on one side (blue-shaded areas in Figure 14 (c)) and a top gate electrode on the other side (green-shaded areas in Figure 14 (c)). The top gate electrode is shaped as a circle with a diameter of 100 μm connected to a square pad to facilitate wire-bonding. It is made of 40 nm-thick Platinum (Pt) deposited on $SrZrO_3$ by electron beam evaporation. Because of the delicacy of the thin barrier layer on top of the quantum well structure, an Al wire is pasted with silver epoxy onto the square pad in the top gate electrode. The other end of the wire is wire-bonded to a PC board.

The physics behind tunneling spectroscopy is summarized as follows [146]. Since a pseudogap closely resembles a superconductor gap (Section 1.3.2), we can do the same analysis for the two types of systems in the case. In a SIN tunneling junction, we assume thermodynamic equilibrium at low temperatures without a voltage bias between the superconductor and the metal. The Fermi levels of the two systems are equal, and no current flows through the external circuit connected to the metal and the superconductor. If a voltage bias exceeding Δ/e (Δ is the energy gap value) is applied between the two systems, electrons tunnel through the insulator and a current flowing through the external circuit. Therefore there be a prominent peak in tunneling conductance as the voltage bias approaches the gap value.

2.2.2.2 Hall bar geometry

A Hall bar geometry device contains an isolated area with quantum well structures that shapes like a Hall bar (green-shaded area in Figure 14 (d)), with eight interface electrodes connected to the area (partly shown in blue-shaded area in Figure 14 (d)). The cross-sectional sketches show the current flowing in-plane, from normal metal to the pseudogap material to normal metal. The Hall bar is divided by electrodes into three 60 um-long

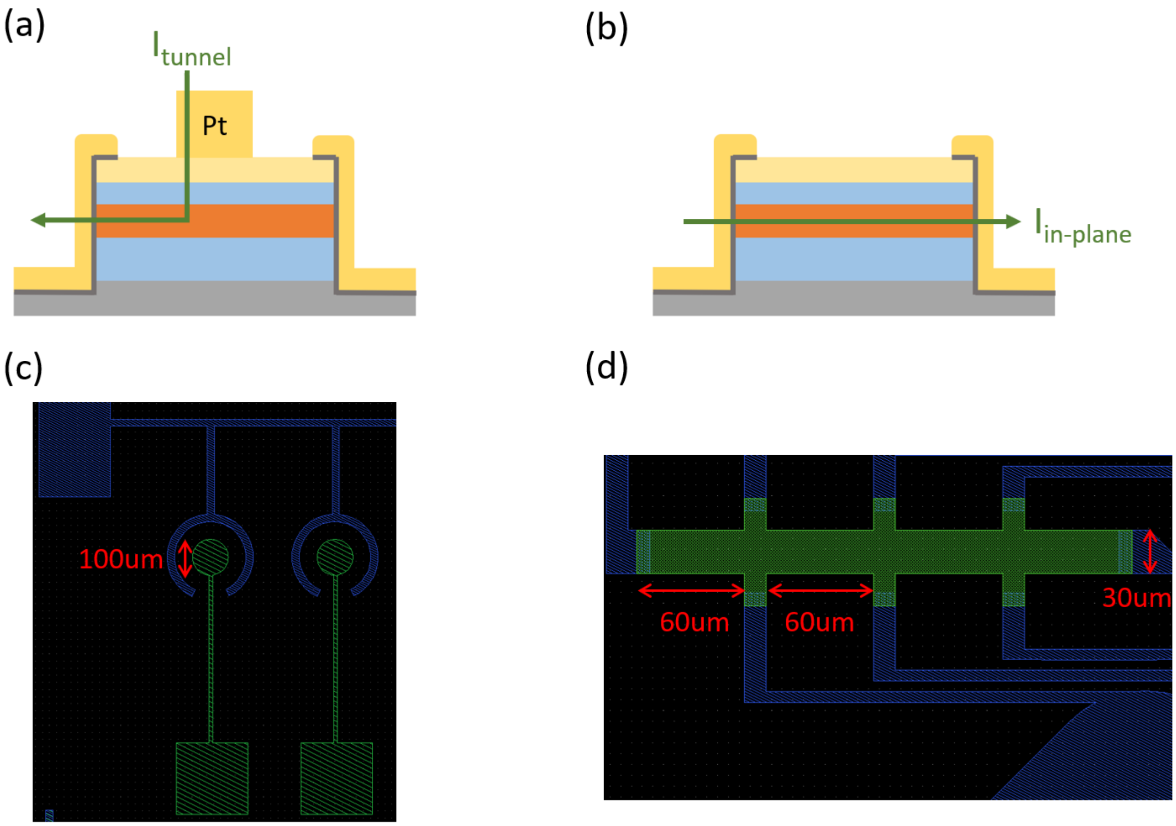

Figure 14: (a) and (b) Cross-sectional sketches of the top gate tunnelling and the Hall bar geometry. (c) Schematic diagram of two top gate devices with two Pt top gate electrodes (green) and one shared interface electrode (blue). (d) Schematic diagram of a Hall bar device. The quantum well structure only exists in the Hall bar area (green) and can be accessed by eight interface electrodes (blue). The designs are created with Layout Editor.

sections horizontally and the vertical width of its main channel is 30 um.

2.3 c-AFM lithography

Nanoscale devices can be created at the $LaAlO_3/SrTiO_3$ interface using conducting atomic force microscopy (c-AFM). A report by Thiel et al. [70] demonstrated that the interface (with $LaAlO_3$ thickness being 3 u.c.) can be switched between the insulating and the conducting phase using a back gate with +/- 100 V voltages applied to its back gate. Inspired by this, Cen et al. [4] realized that the creation of metastable conductive structures in nanoscale using an AFM tip with +10 / -3 V voltages applied through the tip to the $LaAlO_3$ surface. This powerful and versatile method is key to researches summarized in Chapter 4. In the session, we introduce: (a) the working principles of AFM, (b) how to "see" sample surfaces, (c) how to create nanowire devices with c-AFM lithography.

2.3.1 AFM operations

AFM mainly consists of three parts: an AFM tip, a laser optics system, and a piezoelectric scanning system [147]. The AFM tip is shaped like a long beam (this part is also called a cantilever) with a sharp tip at one end. The piezoelectric scanning stage holds the sample and allows for movements of the sample position manually or controlled by a computer. The laser optics system is illustrated in Figure 15 (a): laser is deflected from the top surface of the AFM tip and collected by a quad photo detector. The quad detector has quadrants A (top right), B (top left), C (bottom right), and D (bottom left) and determines the position of the laser spot through the following equations:

$$I_{sum} = I_A + I_B + I_C + I_D$$

$$I_{vertical} = (I_A + I_B) - (I_C + I_D)$$

$$I_{lateral} = (I_A + I_C) - (I_B + I_D)$$

I_A, I_B, I_C, and I_D are the intensities on the four quadrants of the detector. I_{sum} is the total intensity. $I_{vertical}$ and $I_{lateral}$ are the vertical and horizontal intensity differences. Assume the laser spot is round and its intensity has a Gaussian distribution. When the center of the laser spot changes, the distribution of laser intensity on the four quadrants changes as well. The detector can monitor the movement of the laser spot by tracking changes in measured voltages as a function of $I_{vertical}$ and $I_{lateral}$.

When the sample surface interacts with the tip, the force on the tip deforms the cantilever, causing the laser spot to move on the quad detector. The deformation of the cantilever

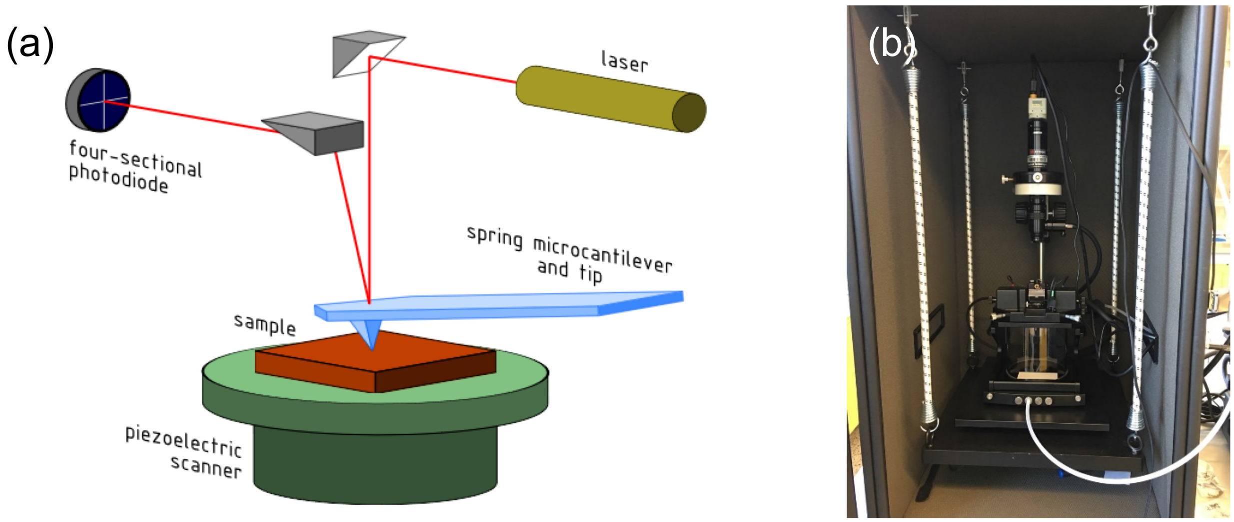

Figure 15: (a) The schematics of a contact mode AFM. The cantilever is a long beam with a tip located at its apex. A laser is reflected from the back surface of the cantilever, and collected by a quad detector. Minute deformation in the tip would shift the center of the laser spot on the quad detector, and be detected by changing differential currents from four sections of the qua detector. Figure adapted from Ref. [148]. (b) Agilent 5500 AFM manufactured by Agilent Technologies, Inc. used in this research. Other models of AFM used in this research include Nanosurf Easyscan 2 AFM and Cypher AFM manufactured by Asylum Research.

follows Hooke's law: $F = -k \times x$ Here, x is the amount of deformation, and k is the spring constant of tip's cantilever. For different types of AFM tips, k can vary between 0.1 N/m and 100 N/m. Tips used in this research have $k = 3$ N/m.

The force between the tip and the sample surface is a function of the distance in between them, as shown in Figure 16. As the tip-surface distance increases from zero, the repulsive force drops rapidly. Then it is replaced by the attractive force, which decreases slower with the distance as the distance approaches infinity.

AFM has three basic modes: contact mode, tapping mode and non-contact mode. Figure 17 compares how the three modes. They also operate in different ranges of tip-surface

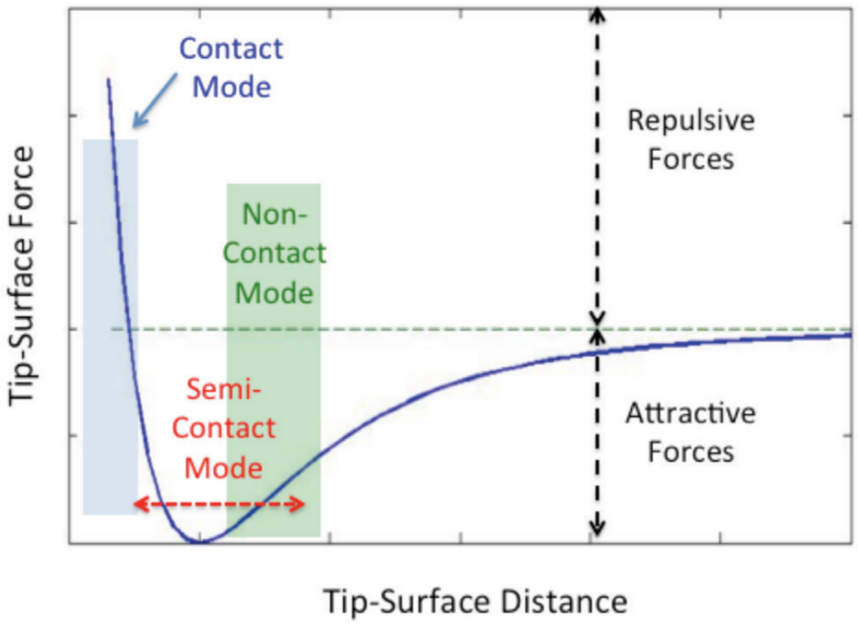

Figure 16: Plot of the force that the sample surface applies to the tip as a function of the distance between the tip and the surface. A positive sign in the force indicates repulsion, while a negative sign indicates attraction. The approximate regions corresponding to the contact mode (blue rectangle), the semi-contact mode or tapping mode (dashed red line) and the non-contact mode (green rectangle). Figure adapted from Ref. [149] .

distance, as shown in Figure 16. In this research, we frequently use the first two modes and provide more contexts for them.

2.3.1.1 Tapping mode

In tapping mode or Acoustic AC mode, the cantilever externally oscillates near its basic resonance frequency (10 kHz – 500 kHz), driven by a sinusoidal electric signal on the tip piezoelectric actuator. As the tip scans across the surface, deviations in the oscillation amplitude or frequency are detected with a lock-in amplifier. From this, interactions between the tip and the surface are measured, providing information about the surface tomography or types of materials present in the sample. The piezoelectric actuator's driving frequency is set to be away from the basic resonance frequency to maximize the gradient of oscillation deviations and the system's sensitivity.

This mode is not detrimental to the surface or the tip, since the tip is not pressed against the surface. This mode has improved lateral resolution on soft samples and it is particularly useful for biology studies.

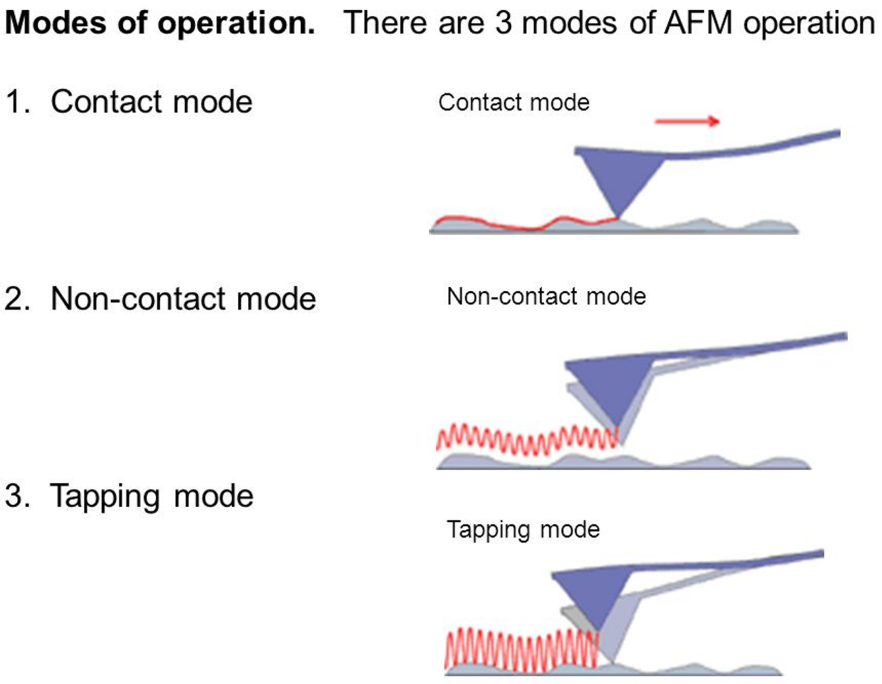

Figure 17: A comparison between three basic AFM modes. Figure credit to: ScienceDirect journal.

2.3.1.2 Contact mode

In contact mode, the AFM tip makes gentle contact with the sample, exerting 0.1 - 1000 nN force on the sample surface. Most commonly, in a constant force mode, the tip maintains a constant cantilever deflection, as well as a constant total force applied to the sample. As the tip scans the sample surface, error signals from the quad detector are input into a feedback circuit to control the tip piezoelectric actuator. Outputs of the feedback circuit are also used to generate a topography image. Another type of contact mode called constant height mode has the height of scanner fixed and uses the error signals to generate a topography image directly.

Calibrations to link the sensitivity of the quad detector to surface features must be done. For example, the amount of nanometers of surface-height change that corresponds to a unit of voltage measured on the detector needs to be determined, as part of the calibration process.

Contact mode usually has the fastest scanning speed but can deform sample surfaces. It is also the only mode that can attain "atomic resolution".

For non-contact mode, the tip is further removed from the sample surface and oscillates at a "free" amplitude. The surface is detected in a similar manner to the tapping mode. However, since the attractive force on the tip is generally minute, this method usually does not provide very good resolution unless placed under a strong vacuum.

2.3.1.3 Additional imaging modes

Besides the three basic modes discussed above, AFM is a highly versatile tool that can be used to perform many different imaging modes with the same basic hardware [147].

1. Scanning microscopy imaging (STM) monitors the tunneling current that runs through the tip, the sample and the narrow "gap" as a bias voltage is applied on the tip. Changes of only 0.1 nm in the separation distance could cause an order of magnitiude difference in the tunneling current, making STM remarkably high lateral resolution.

2. Piezoresonse force microscopy (PFM) measures sample topography simultaneously with its mechanical response to application of electrical voltages, and is a handy tool to study the piezoelectric materials at nanoscale. Piezoelectric materials shrink or expand in the presence of external electric fields. Inversely, external stress of strain applied to those materials induce internal electric fields. In PFM measurement, a c-AFM tip is in contact with the sample with a sinusoidal bias voltage applied. For a piezoelectric sample, the electric field cause topographical changes. These changes be measured with the lock-in technique described in Section 2.5.4 to maximize the signal-to-noise ratio. If the sample contracts in

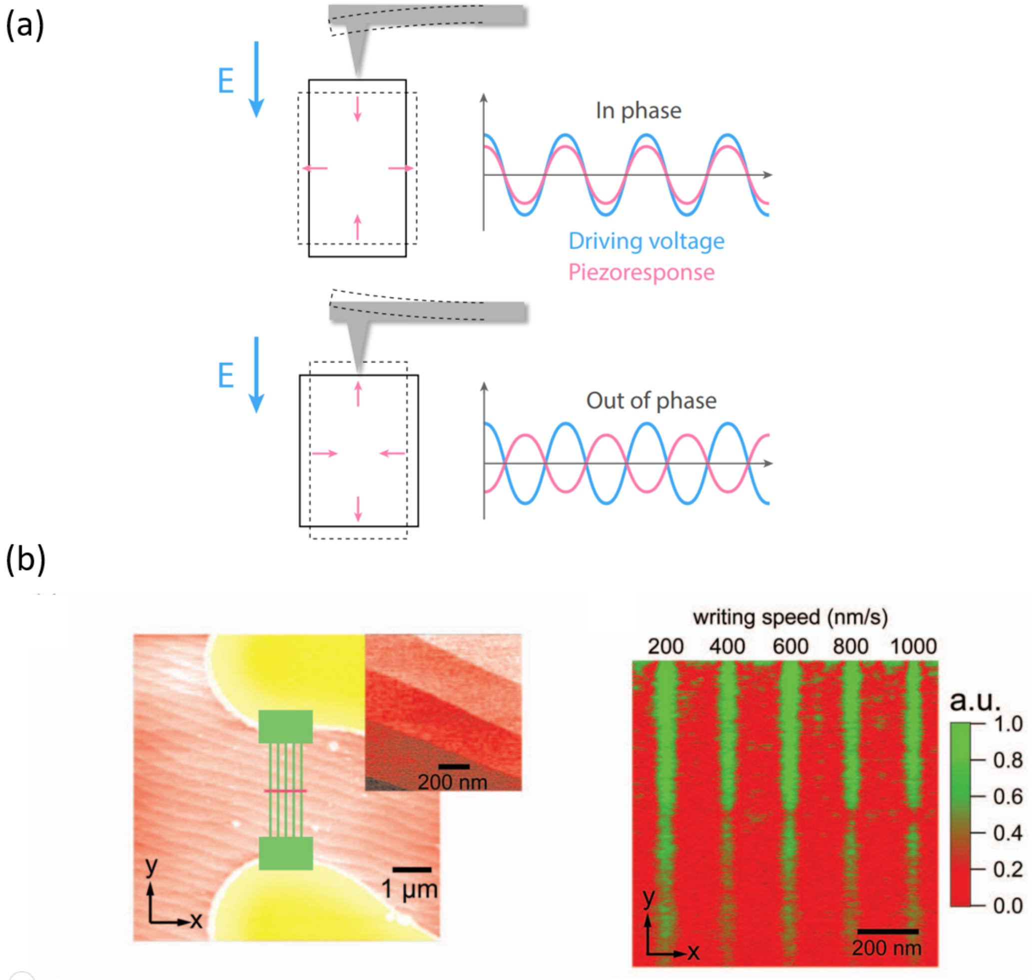

Figure 18: (a) Diagram showing how the PFM mode operates. A sinusoidal electric field is applied to the sample surface through a conductive tip, inciting piezoelectric responses in samples. Resulting changes in topography cause the laser spot on the quad detector to move (not shown in the diagram). Courtesy Jianan Li [130]. (b) c-AFM lithography schematic of five wires, separated by 200 nm, written with +10 V tip voltage, then cut in the middle using tip voltage -8 V (left). PFM amplitude imaging of the five parallel wires reveals that conductive wire regions are elongated in the Z direction at room temperature (right). Figure adapted from Ref. [103], Figure 2.

the same direction as the electric field and expand in the perpendicular direction, as shown in Figure 18 (a) in the top scenario, topography changes be in phase with the electric field. Inversely, if the sample elongate in the direction perpendicular to the electric field direction, topography changes be out of phase with the electric field.

PFM is used frequently to study ferroelectric domain orientation [150], ferroelectric domain boundary [151], carrier concentration [103], and certain mechanobiology properties in biological samples such as teeth, bone, and DNA [152, 153]. In researches related to the $LaAlO_3/SrTiO_3$ system, PFM has been used to image conductive nanostructures created using c-AFM lithography technique, as shown in Figure 18 (b) [103], and to probe the charging/discharging dynamics of nanoscale conducting islands in a joint measurement of capacitance changes of the heterostructures [154].

2.3.2 Creating quantum devices with lithography

Besides characterizing surface features, AFM can also modify sample properties. One such application central to the research in the thesis is c-AFM lithography, which creates conductive nano-structures at the interface of $LaAlO_3/SrTiO_3$.

Lithography processes are illustrated in Figure 19. We start with a insulating interface, with $LaAlO_3$ thickness being 3.4 unit cell, which is below the critical thickness of 4 unit cell. An AFM tip, with a positive bias, moves across the surface of the sample in contact mode. Meanwhile, the sample is grounded. The electric field from the tip induce a local metal-to-insulator transition at the interface and create conductive channels. The metal-to-insulator transition is reversible. If a negatively biased tip moves across the surface in contact mode, the process can erase conductive channels and create insulating barriers. The processes are conducted at room temperature. Conductive channels created in this way can have width as small as 2 nanometers and freeform shapes, making it a powerful tool to make a myriad of quantum devices, such as superconducting nanowires [17, 155, 156], waveguides that exhibits ballistic transport properties [157, 102, 158], Kronig-Penney superlattices [159].

To ensure that lithography successfully created long lasting conductive channels, we usually monitor the two-terminal or four terminal conductance between electrodes on canvases. In Figure 19, golden regions indicate a pair of electrodes in direct contact to the $LaAlO_3/SrTiO_3$ interface, made using sample processing methods described in Session 2.1.2. An sinusoidal source voltage with its amplitude being 100 mV is applied to the right electrode, while the left electrode is connected to an ammeter to measure current, and then to ground. A two-terminal conductance, calculated as current divided by source voltage, is monitored in real-time during lithography. When a conductive nanowire connecting two electrodes is created with lithography, a steep increase in conductance can be observed. One such example is provided in Figure 19 (b). Typical resistances of such nanowires are around 200 kOhms/μm and can vary greatly depending on the quality variation among different samples and even the different areas on a sample. Reversely, a negative tip voltage can erase the conductive channels and create barriers in the nanodevices, indicated by a decrease abrupt decrease in the two-terminal conductance (Figure 19 (c-d)). The decrease can be fitted to a exponential function to derive an estimation for the half-maximum width of the nanowire. A typical width of those nanowires is 2 nm.

2.3.2.1 Water-cycle mechanism

The mechanism for c-AFM lithography can be attributed to "water-cycle" mechanism [160] and surface protonation [161]. It has been discovered that the efficiency of c-AFM lithography is strongly dependent on atmosphere conditions.

On the one hand, the writing and erasing process only works when the surrounding air humidity is within a suitable range, leading to speculations of "water-cycle" mechanism. The hypothesis is that H_2O molecules dissociates into OH^- and H^+ at the $LaAlO_3$ surface and writing process removes some OH adsorbates, leaving the surface in excess of H^+ ions. H^+ ions attract electrons to the interface, make it locally conductive. Inversely, erasing process removes H^+ and restores the balance between OH^- and H^+, making the interface insulating again [160]. Repeated writing and erasing process doesn't modify interface qualities.

On the other hand, conductive regions created with lithography are metastable. Left under atmospheric conditions, they all gradually decay into a insulating state. For some samples and lithography parameters (Session 2.3.2.2), conductive regions can last for a day,

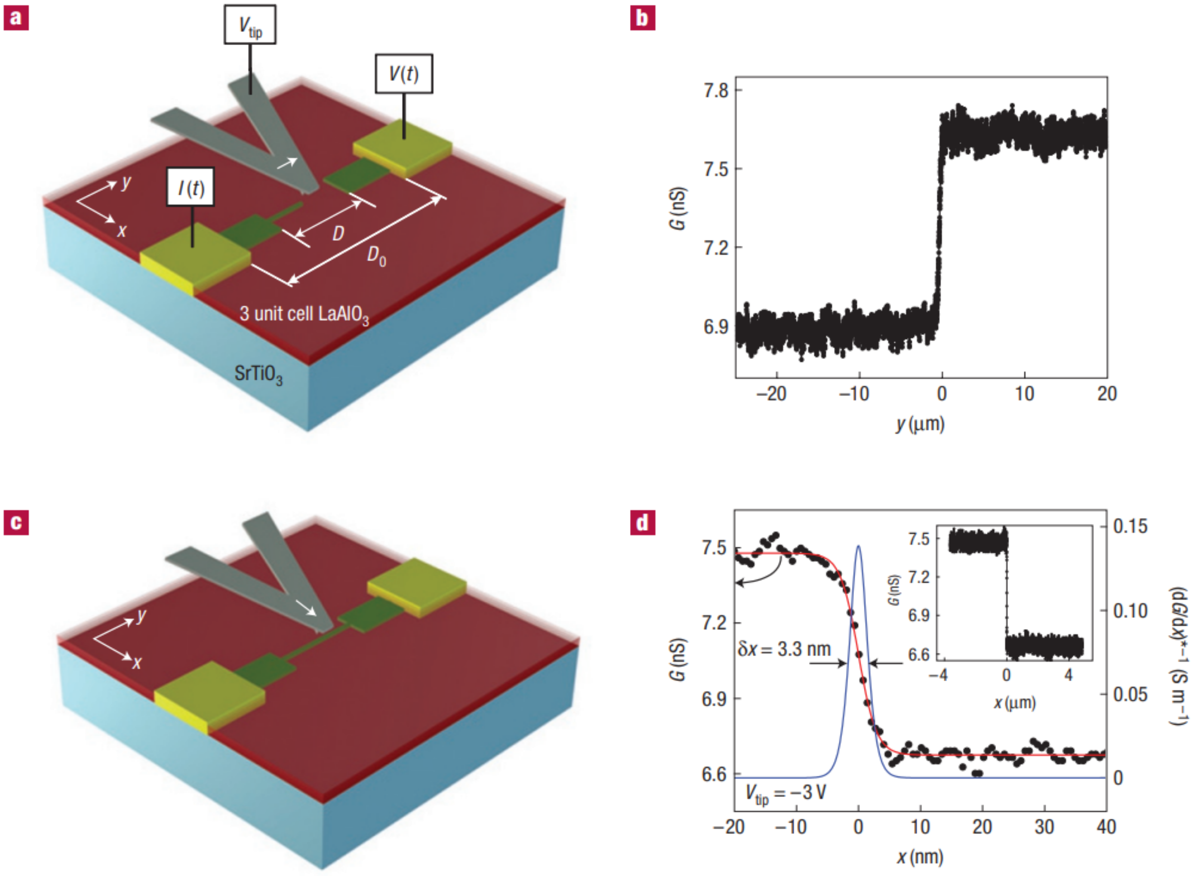

Figure 19: Writing and erasing nanowires at the $LaAlO_3/SrTiO_3$ interface. (a) A tip with a positive voltage moves across an insulating sample surface in contact mode, creating conductive channels. (b) The conductance between the two electrodes as a function of tip position while writing the nanowire connecting one electrode to another. A steep increase as a result of c-AFM lithography was recorded. (c) The experimental set-up for cutting a conductive wire. The tip is now biased with a negative voltage as it moves across the wire. (d) A decrease in conductance during wire cutting. The decrease was fitted to a function $G(x) = G_0 - G_1 \tanh(x/h)$ and the half-maximum width of the nanowire derived was 3.3nm. Figures adapted from Ref. [4]

but for others samples and parameters, conductive regions only exist for less than a hour or even several seconds. However, under vacuum conditions, conductive regions are much more stable and, in principle, can last indefinitely.

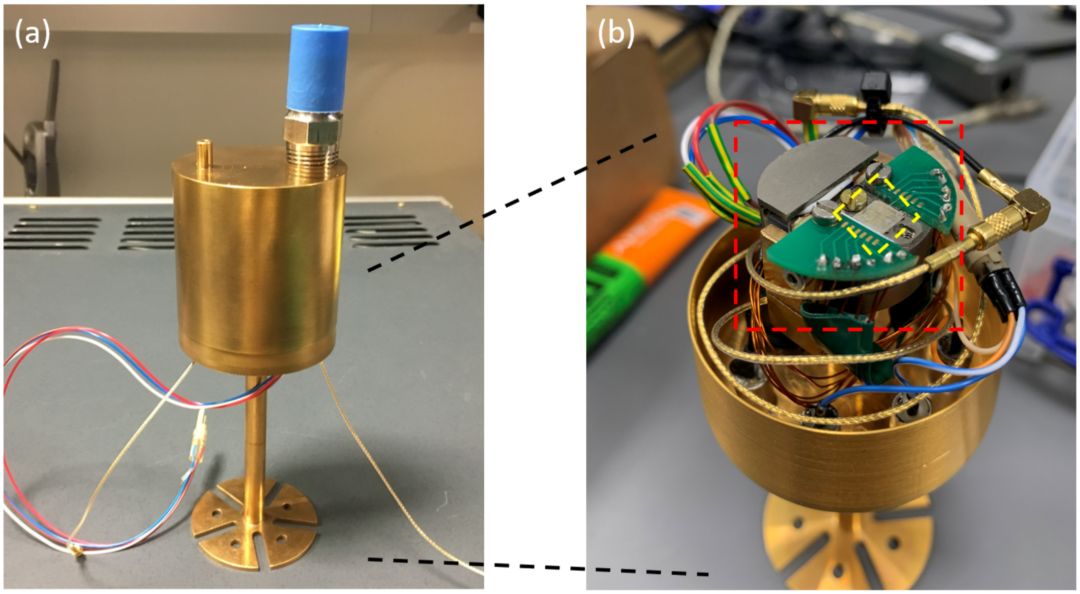

Figure 20: (a) A two-piece small vacuum chamber used in this research to transport the sample post-lithography from the AFM to the dilution refrigerator while keeping the sample in vacuum. There is also a port (covered by the blue cap) to connect to a vacuum pump. (b) The bottom piece of the chamber, with a strain cell (red dashed line, Section 2.4) and a sample (yellow dashed line) visible. The gold plated copper piece also serves as both the sample holder in the AFM and the cold finger in the dilution refrigerator.

In this research, we often conduct c-AFM lithography on 100 μ m-thick, 3.4 u.c. $LaAlO_3$ /$SrTiO_3$ samples to create nanowire devices, using AFM in model Agilent 5500 or Nanosurf Easyscan 2. When those instruments are not located in a humidity controlled room, our ability to create lasting conductive regions is sometimes obstructed by unsuitable weather (E.g. dry winter days or humid summer days). In an attempt to change humidity, a humidifier is sometimes employed.

Furthermore, those nanowire devices sometimes only last for 20 min in atmosphere, before part of the devices become insulating again, posing a challenge to transfer samples from the

AFM to the dilution refrigerators for cryogenic transport measurements with devices intact.

For the purpose of protecting devices by pumping vacuum around samples post lithography, a small two-piece vacuum chamber (Figure 20) is custom designed and made. Top and bottoms pieces of the chamber, both made of gold-plated copper, have matching cone shapes so that when pressed together, the joint between them be vacuum tight. This type of cone vacuum seal is also extremely quick to assemble. The bottom piece also serves as the sample holder in the AFM Nanosurf 2 and the cold finger in the dilution refrigerator DR200. Therefore, it has clamps to grab on the strain cell and vacuum-grade Lemo and Fischer panel connectors for electrical wiring.

After lithography created nanowire devices, we join the two pieces to enclose the sample and the strain cell (Section 2.4) in the chamber and pump vacuum from a port (covered by a blue rubber cap in Figure 20 (a)) on the top piece. It usually takes $10 \sim 15$ min for the pressure in the chamber to reach 10^{-2} mbar. At this time, atmosphere outside the chamber pushes the two pieces together, forming a decent seal and keeping the chamber in vacuum after breaking it away from the pump. This buys us time to assemble the chamber to a dilution refrigerator, connect wires and cables from panel connectors, pump air out of the large space in the dilution refrigerate, while the nanowire devices remain protected.

2.3.2.2 Writing nanowire devices

Key lithography parameters include the deflection set point which determines the force between the tip and the surface, the DC voltage applied to the tip, the resistance of a current limiting resistor in series with the tip, and the speed at which the tip moves across the surface. Optimal values for those parameters vary for different samples and AFM instrument used and are figured out after some testing. A set of typical parameters used in the research is listed below.

Another frequently used process is to remove contaminants from a canvas region of a sample by scanning the region over and over in contact mode. Contaminants could be nanofabribation process residues (Section 2.2), chemicals associated with epoxy curing (Section 2.4.1), or simply dust in the atmosphere. With a larger set point and a slower tip speed,

Table 2: Frequently used c-AFM lithography parameters for 100um-thick, 3.4 u.c. $LaAlO_3/SrTiO_3$ samples and Agilent 5500 AFM.

Parameters	Reference values
set point − deflection	0.4 V ∼ 0.6 V
writing tip voltage	+18 V ∼ +25 V
erasing tip voltage	-8 V ∼ -10 V
tip speed	0.4 um/s ∼ 1 um/s
tip resistor	100 kOhms

contact mode scan can pick up some particles and transport them to the edge of the scanned regions. If done successfully, a small-sized scan (3 μm by 3 μm) can reveal crystal terraces of $LaAlO_3$ in a striped pattern with about 0.4 nm step height. The process usually precedes c-AFM lithography. It can reduce unwanted defects in the lithography-created nanowire devices.

2.4 Uniaxial strain application

A cryogenic uniaxial strain cell, model CS100, manufactured by Razorbill Instruments, is used to apply continuously tunable tensile and compressive strains to $LaAlO_3/SrTiO_3$ samples. We will refer to this as "strain cell" in short. In this research, the operation needs to take place in a temperature well below the superconducting transition temperature $T_c \sim$ 300 mK of the material in order to observe the effects of strain on superconductivity and sometimes in magnetic field. The strain cell has a small size, roughly 20 × 24.2 × 14 mm, that fits into the dilution refrigerators used (Section 2.5.1).

2.4.1 Mounting sample

Mounting the sample on the very top face of the strain cell maximizes the angle of access. Therefore, we can use an AFM tip to scan the sample surface and create conductive nanostructures (Section 2.3) while the sample is mounted on the strain cell.

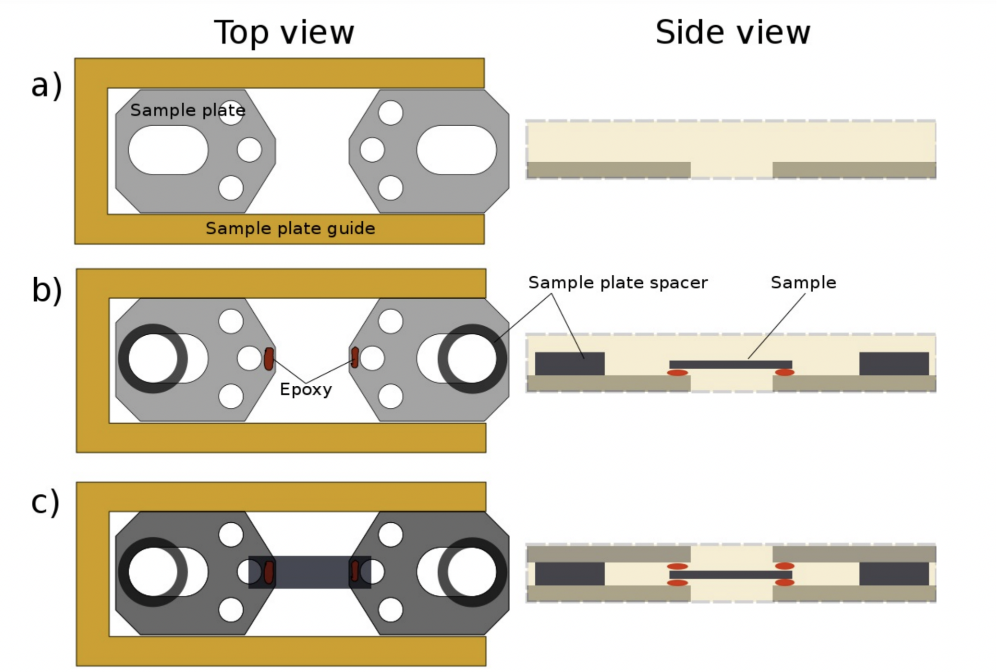

Figure 21: Diagram of CS100 sample mounting. Sequence: (a) align sample plates with sample plate guide, (b) secure the sample firmly with epoxy, (c) In the optional final step, secure the upper sample plates using the spacers to set a distance matching sample height. Figure adapted from Ref. [162].

The sample mounting process aims at fixing the two ends of the sample to the strain cell body so that it experiences homogeneous uniaxial strains when the instrument is operated. The process is shown in Figure 21. First, two sample plates are fastened to the strain cell using M2 brass screws and aligned parallel using the sample plate guide, which itself is fastened to the cell using M1.6 screws. A drop of epoxy Master Bond EP21TDCHT is then deposited to the two ends of the sample plates and the sample is placed on top. The the sample ends should always be separated from the sample plate by the epoxy, so that are electrically isolated.

The epoxy is a two-component epoxy adhesive. The two chemical components are mixed together by a weight ratio and left to cure for 72 hours in room temperature, due to considerations of the maximum permitted temperature of the strain cell. As the epoxy cures, the sample is placed under a venting hood to prevent fumes generated from the chemical reactions to condensate on and contaminate the sample surface. However, this step only alleviates the contamination, not prevents it. Once cured, the epoxy forms strong bonds with both Ti sample plates and Ti-based sample and has preferable qualities including superior toughness, excellent electrical insulation, small thermal expansion, and stability under harsh thermal cycles.

After the sample is secured, an optional step, shown in Figure 21 (c), is to deposit another layer of epoxy to the upper surface of the sample. Sample plate spacers are also placed to set the distance between upper and lower sample plates. Finally, the upper sample plates are placed above the sample plate spacers and epoxy, and fastened using M2 screws. The application of upper sample plates ensure the stress is applied evenly to the sample (not just to the bottom of the sample). However, in this research, the step is not adopted for the reason that epoxy might spread and contaminate the sample surface during the slow cure.

2.4.2 Operating CS100 strain cell

Figure 22 illustrates the movements in the strain cell when the sample is subjected to positive and negative strains. There are three sets of piezoelectric stacks, two outer stacks and one inner stack, that lengthen or shorten in response to voltages applied to them. Two ends of the sample is attached to the strain cell in the unstrained state. We apply voltages of opposite signs to outer stacks and the inner stack. When the outer stacks extended and the inner stack retracted, the sample is under tensile strain, while retracted outer stacks and the extended inner stack put the sample under compression. Using pairs of stacks working in opposite direction doubles the force exerted on the sample and the displacements of the sample, compared to a single piezoelectric stack.

The arrangement of three identical piezoelectric stacks also provides a smart way to

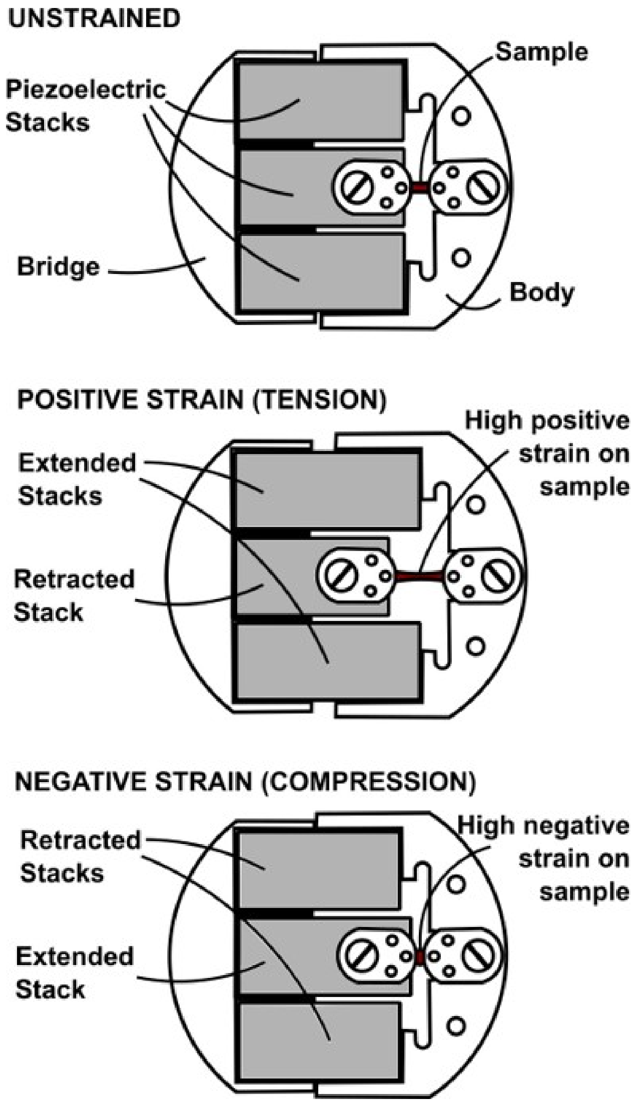

Figure 22: The principle of operation for the strain cell. Varying the signs of the voltages on the piezoelectric stacks changes the types of strain between tension and compression. The sample displacement is exaggerated in the diagram for illustrative purposes. Picture credit to: Razorbill Instruments.

compensate for the thermal expansion of stacks. The stacks lengthen in their polling direction upon cooling. This lengthening is many times longer than the stroke length of the stack, so that steps must to taken to prevent unwanted strain on the sample during cool down. The strain cells overcomes this issue by allows the thermal expansion of the stacks to cancel out, leaving the strain unaffected by the thermal elongation of the stacks. Therefore, the strain cell can operate in a wide range of temperature, from up to 400 K to less than 300 mK.

Despite being a new technique developed in the recent decade, strain cell has proven its versatility and strength in several studies: elastro-resistance measurements that revealed electronic nematic order for iron-based superconductors such as $Ba(Fe_{0.975}Co_{0.025})_2As_2$ [163], $CsFe_2As_2$ [55, 56], FeSe [164]; mageto-elastoresistance of WTe_2 [165]; strain-induced magnetic phase transition in CrSBr [166]; strain in conjunction with high-energy-resolution X-ray scattering in Advanced Photon Source revealing spin-orbit entangled pseudospin state in Sr_2IrO_4 [167, 168].

2.4.3 Calibrating strain

Position feedback, or the measurement of the displacement between two ends of a sample, is provided by monitoring a parallel plate capacitor below the sample. In the research, we use an Andeen-Hagerling high-precision capacitance bridge (model AH2500A, 1kHz) to obtain accurate measurements of the capacitor at room temperature or in cryogenic temperatures.

Each strain cell comes with a room-temperature calibration curve: the displacement as a function of the capacitance of the capacitor. We take into account the thermal contraction of the capacitor plates using the following equation: $C/C_{300K} = 1 + 2x\delta(T)$, where $\delta x(T)$ is the integral thermal expansion of titanium between T and 300 K. C_{4K}/C_{300K} is provided to be 0.968, and we use this number to estimate the calibration curve at cryogenic temperatures. We then measure curves of the capacitance as a function of the voltage applied to piezoelectric stacks, with a sample mounted on the strain cell at cryogenic temperature. Using the calibration curve, we can figure out the relations between the voltages applied to piezoelectric stacks and the displacement of a sample.

Besides the thermal contraction of the capacitor plates, the deformations of epoxy used in sample mounting and even the strain cell itself are likely to affect the accuracy of the position feedback. To reduce the effects of deformed epoxy, we use a type of epoxy with high toughness and purposefully apply only a very thin layer of epoxy. Deformed strain cell would be a problem if the sample is much stiffer than the Ti material the strain cell is made of, causing the capacitor to over-read the displacement.

The ratio between the capacitor-measured displacement and the actual displacement of the sample is denoted by $\Delta L_{meas}/\Delta L_{real}$. The ratio is affected by several factors, as described by the equation

$$\frac{\Delta L_{meas}}{\Delta L_{real}} = 1 + \frac{k_s}{k_\tau}(h_s + h_a)(h_s + h_c)$$

,where k_s is the spring constant of the sample, k_τ is the spring constant of the strain cell, h_s is the distance the sample is mounted above the top of the strain cell, and h_a and h_c are dimensional parameters of the strain cell. In the research, we estimate h_s to be about 1mm. As plotted in Figure 23 (b), keeping all other parameters fixed, $\Delta L_{meas}/\Delta L_{real}$ is proportional to k_s.

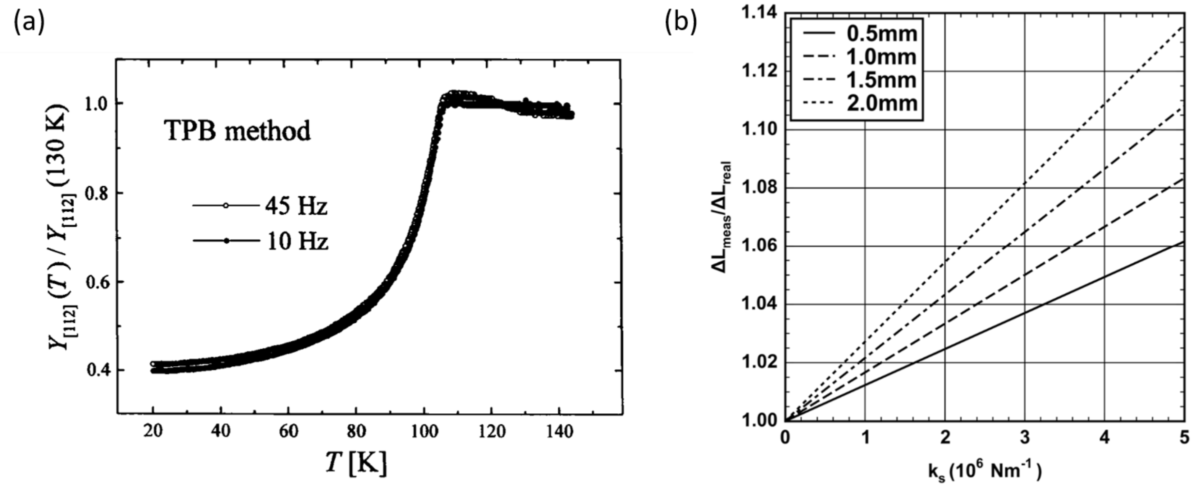

Figure 23: (a) Temperature dependence of the relative Young's modulus $Y_{|112|}$, of SrTiO$_3$ crystals measured by the TPB-method at low frequency. Figure credit to Ref. [169]. (b) The value of displacement measured from the capacitance sensor relative to the true displacement of the sample as a function of the sample spring constant k_s. h_s represent the different height of the sample above the top of the apparatus, which, in the research, is estimated to be 1.0 mm. Figure credit to: Razorbill Instrument.

Next, we give an estimation of the spring constant k_s of a sample, as defined by Hooke's Law $F = k_s \cdot x$. Consider the sample an ideal bar, or an elastic rectangular piece of solid,

Table 3: C_{ij} and other related elastic properties: bulk modulus (B), shear modulus (G), and Young's modulus (E) of $SrTiO_3$ compounds. All values given in units of GPa. The first row is the result of DFT calculations based on PBE functional [170], and they agree well with experimental values[171].

Compound	Method	B	G	E	C_{11}	C_{12}	C_{13}	C_{22}	C_{33}
$SrTiO_3$	PBE [170]	179.9	110.3	274.8	333.3	103.2	103.2	333.3	333.3
$SrTiO_3$	Expt [171]	178.8	112.5						

whose length L along the direction of displacement is 5 mm and the cross-sectional area S can be calculated by 5 mm × 0.1 mm = 0.5 mm ^{2}. We assume that the displacement ΔL along the length dimension is much smaller and negligible compared to L. The spring constant can be written as

$$k_s = E \cdot S/(L + \Delta L)$$

,where E is the Young's Modulus of $SrTiO_3$. The Young's modulus of bulk $SrTiO_3$ is approximately 274.8 GPa at room temperature [170] (Table 3). And under 105 K, after $SrTiO_3$ undergoes a cubic-to-tetragonal phase transition and forms three types of ferroelastic domains, the mobility of domain walls lowers the Young's modulus to 40 % of its value at 130 K, as shown in Figure 23 (a) [169]. Therefore, the spring constant k_s of the sample at cryogenic temperatures is estimated to be $\sim 1.096 \times 10^7 N \cdot m^{-1}$.

From our calculation, we know that those $LaAlO_3/SrTiO_3$ samples are extremely stiff. Extrapolating the linear relationship between $\Delta L_{meas}/\Delta L_{real}$ and k_s in Figure 23 (b), ΔL_{meas} $/\Delta L_{real}$ is estimated to be around 1.18.

Using the calibrated displacement measurement, ΔL_{meas} at 50 mK with a sample mounted are found to be only a few micrometers. A global strain, defined as the displacement divided by the sample length, which is 5 mm, is less than 0.03 %. More details are shared in Chapter 4.

2.5 Low-temperature transport measurements

2.5.1 Principle of dilution refrigerator

To study quantum mechanical behaviors in electronic transport, such as quantum hall effects and quantized conductance, samples need to be in the millikelvins regime, otherwise thermal broadening would wash out all those features. In the research, since the focus is the superconductivity of $LaAlO_3/SrTiO_3$ interface with T_c = 200 - 300 mK, dilution refrigerator is the widely used instrument to cool down samples to a suitable temperature T $\sim$ 50 mK.

Dilution refrigerator was first proposed in 1950s and realised experimentally in 1966 by Henry Hall at Oxford Instrument. At that time, minimum temperature of 200 mK was achieved. Nowadays, temperatures below 4 mK can be obtained using this technique [172].

The dilution process can be described as removing ^{3}He from the mixture of ^{3}He and ^{4}He across phase boundary (Figure 24). As temperature decreases and the percentage of ^{3}He in the mixture decreases, the mixture enters a superfluid phase. According to the phase diagram in Figure 24 (a), there's a finite solubility of ^{3}He in ^{4}He that decreases rapidly with temperature when temperature is below 0.8 K. When temperature is 0 K, the concentration of ^{3}He in ^{4}He must be lower than 6.4 %. The phase is also called diluted phase and is the key to dilution refrigeration. Extra ^{3}He be separated from the diluted mixture, floating on top of the mixture in the form of pure ^{3}He liquid. In Figure 24 (d), as ^{3}He atoms in the mixture are removed, ^{3}He atoms in the pure liquid cross the phase boundary in to the mixture. The process absorbs heat and provides cooling power.

The removal of the ^{3}He atoms takes place in still (Figure 24 (c)), where a pump is utilized to distil ^{3}He from ^{4}He by creating difference in vapour pressure. As a result, ^{3}He atoms cross the phase boundary in a mixture chamber connected to the still, making it the coldest place in the refrigerator.

Dilution cooling only operates when temperature is sufficiently low so it relies on other coolers to provide a stable cold environment. Pulse tube cooler or liquid helium bath is the most common method to cool down from room temperature to 4 K. This is followed by evaporative cooling of ^{4}He to lower temperature to around 1.2 K and then evaporative

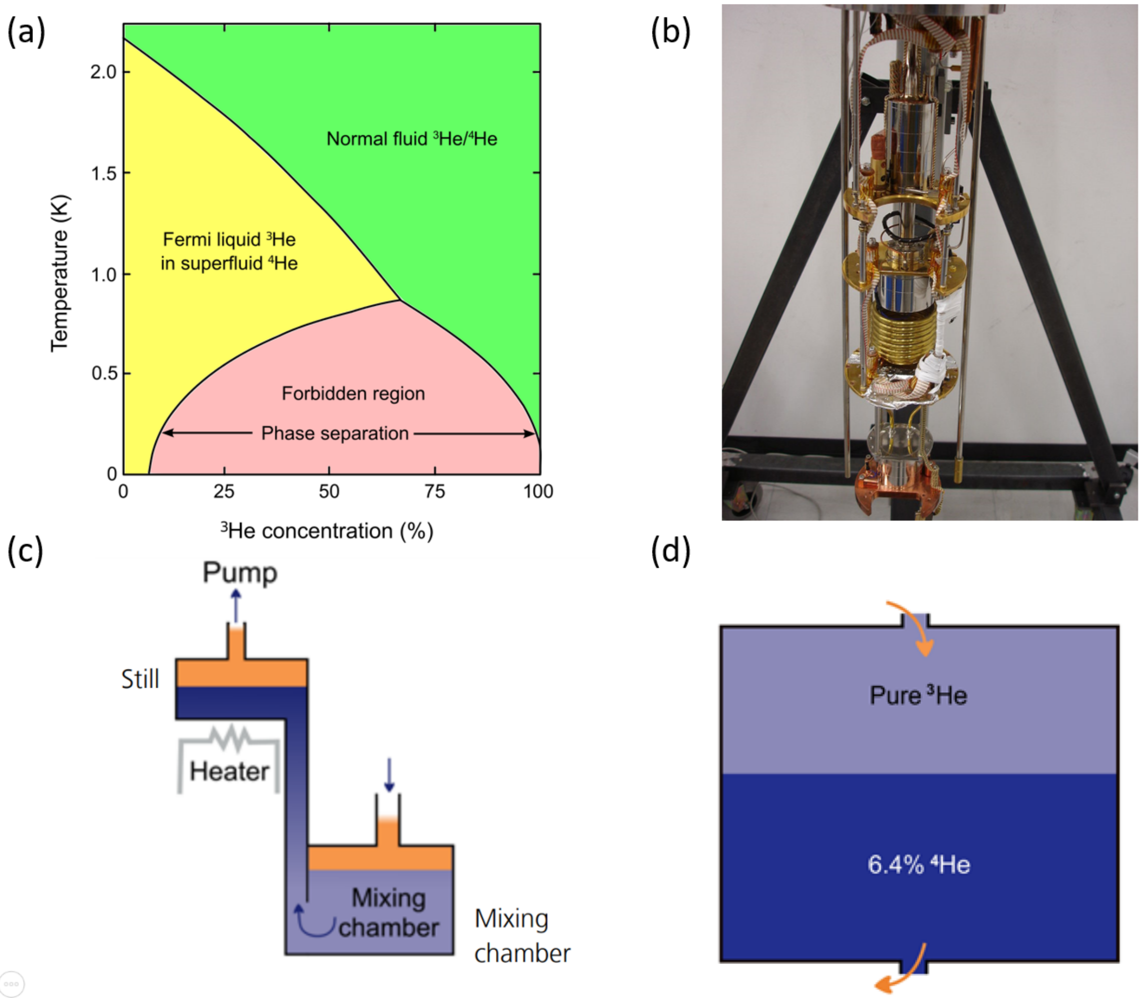

Figure 24: (a) Phase diagram of liquid ^{3}He and ^{4}He mixtures showing a forbidden region that causes the phase separation. (b) The inside of a Oxford Instruments dilution refrigerator, showing from top to bottom: the still, heat exchangers (golden coils) and the mixing chamber . (c) The removal of ^{3}He from diluted ^{4}He by pumping on a still, which connects to a mixing chamber. Still is heated to ensure enough vapour pressure for the pumping to be effective. (d) At low temperature, finite solubility caused the separation of ^{4}He-rich diluted phase and pure ^{3}He liquid. Figure credit to: Oxford Instrument [172].

cooling of ^{3}He to reach 0.3 K. Dilution cooling is the final step to get to base temperature.

In the research, multiple dilution refrigerators are used for experiments, most notable model Leiden Cryofree (CF) and Oxford DR200. Both belong to the “dry” category.

Taking another look at Figure 24 (a), ^{3}He atoms pumped from the still would circulate back into the mixing chamber. However, those atoms in circulation are much hotter and need to be cool down before they reach the mixing chamber. In a “dry” dilution refrigerator, the cooling is done by heat exchangers between the circulation line, the still and the mixing chamber, instead of an dedicated 1 K ^{4}He evaporation pot in a “wet” refrigerator. Heat exchangers are generally less efficient than 1 K pot, causing higher condensing pressure, especially at the start of circulation, and requiring an additional high pressure pump. “Dry” refrigerators have the advantage of requiring much less maintenance than “wet” refrigerator, except for servicing the aforementioned high pressure pump.

A system usually includes a dilution cooling unit(shown in Figure 24 (b)), pulse tube for pre-cooling, vacuum chambers and radiation shield cans, magnets, a gas handling system(GHS) and controlling software. Figure 25 is an example of a complicated GHS. It enabled a high level of automation of the following processes: cooling and warming the system, condensing and collecting the mixture, monitoring and logging pressure and temperature readings and any error messages, safety interlocks and pressure-relief valves etc. Thus, complex operations are reduced to clicks of a few buttons. Superconducting magnets are mounted inside the refrigerator on the 4 K stage and use large currents running through superconducting coils (made from Nb_3Sn or NbTi) to generate magnetic fields.

A sample either mounted directly on the cold finger of a demountable “puck” loads of a dilution refrigerator, or mounted on the strain cell, which is then attached to the puck using a custom-made clamp. After the sample has devices created with c-AFM lithography at room temperature, we transfer it into a puck and insert the puck into the refrigerator. The sample be attached to the mixing chamber plate with a bolted contact, so that it is in great thermal contact with the mixing chamber. The cool down process differs for different refrigerators. Take model Leiden CF as an example. It takes about ten hours to reach T = 5 K, about a hour and a half to condense the mixture, and about one hour to reach T < 50 mK with based temperature about T = 35 mK.

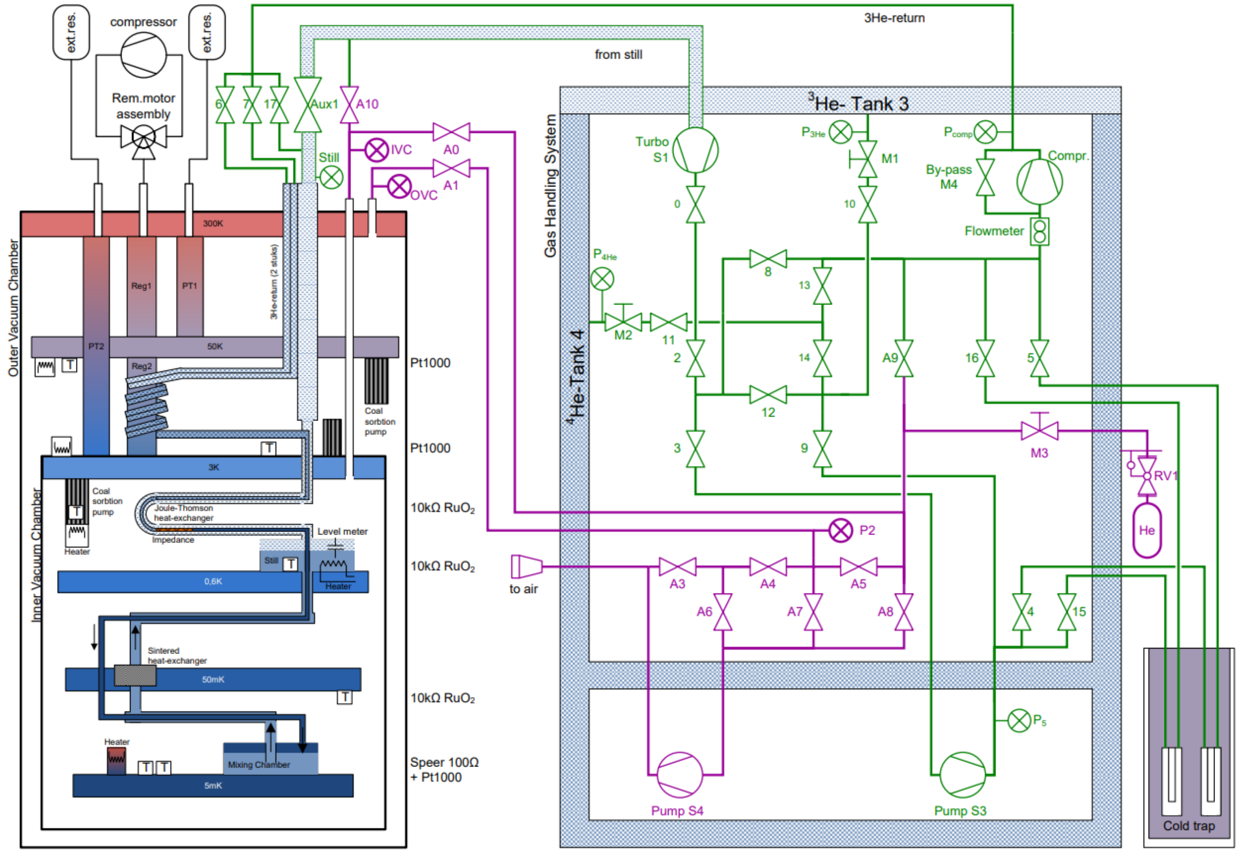

Figure 25: Schematics of the actual gas handling system in Leiden CF system. Picture credit to: Leiden Cryogenics.

2.5.2 Electrical transport measurement

2.5.2.1 Data Acquisition setups

Figure 26 is a simplified schematics for electric transport measurement and compares the two scenarios: the two-terminal measurement and the four-terminal measurement. The latter has improved accuracy by using separate pairs for current carrying (marked S and D) and voltage sensing electrodes (marked V+ and V-), so that wire, lead and contact resistances are eliminated from the four-terminal measurement. Therefore, the four-terminal measurement is the standard method used in the researches to characterize the resistivity of nanowire devices in $LaAlO_3/SrTiO_3$ samples (Chapter 3) or mesoscopic devices in $SrTiO_3$ quantum wells (Chapter 4).

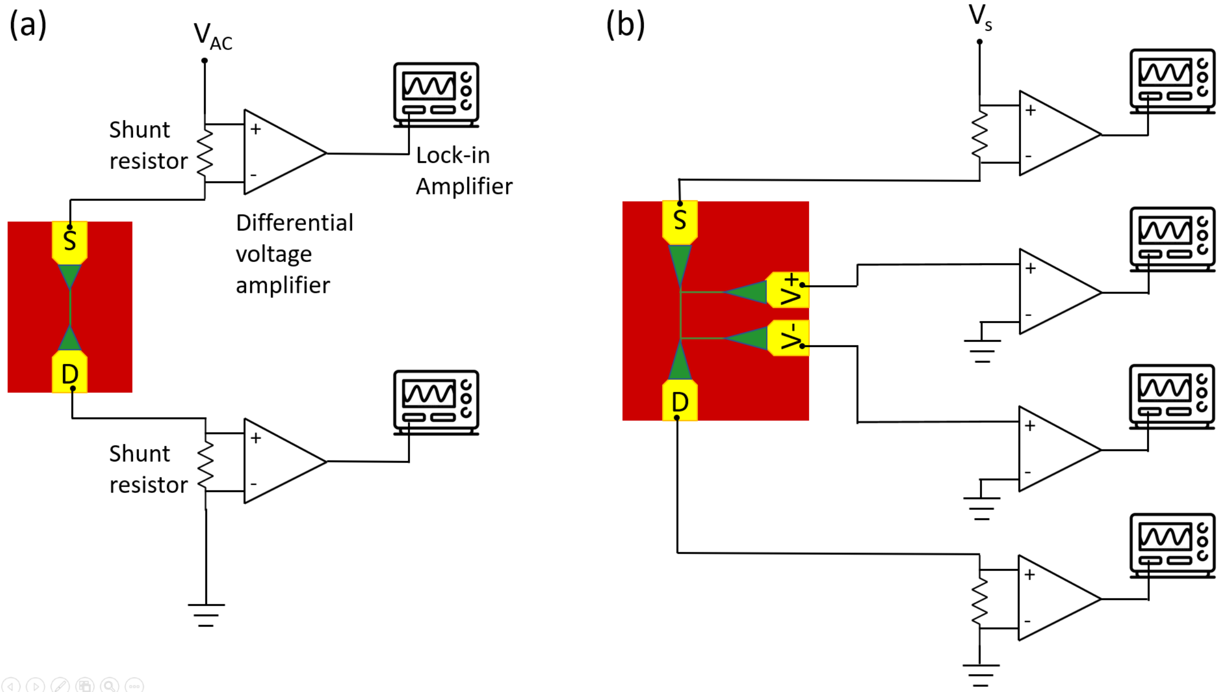

Figure 26: (a) Diagram of two-terminal measurements. A AC voltage bias is applied between source (S) and drain (D) electrodes. The measurement of the current flowing through a nanowire device (green) on a $LaAlO_3/SrTiO_3$ sample (red) is converted into the measurement of a voltage drop on a shunt resistor (in Instrument Krohn-Hite 7500). The voltage signal, amplified by a differential voltage amplifier, is input into a lock-in amplifier to extract the amplitude and the phase with a high precision. Cryo-filters and π-filters are not shown in the diagram. (b) Diagram of four-terminal measurements. The addition of two electrodes V+ and V- enables the voltage drop on a section of the nanowire device to be measured.

Wire-bonds connect electrodes on the sample to PC boards on the cold finger of the probe in a dilution refrigerator. From PC boards, wires for 24 DC lines then go through cryo-filters installed in the mixing chamber stage, which are either meander filters or low-pass RC filters with a nominal cutoff frequency of 1 kHz. The cryo-filters suppress the available frequency bandwidth in the DC lines to below a few tens of Hz, at the same time effectively reduce the electron temperature and high frequency noise. DC lines then go through phosphor bronze twisted pairs, and connect to a 24-pin Fischer connector that passes the signals to the outside of the refrigerator. From there, DC lines go to a breakout box with π-filters, then to amplifiers such as Kron-Hite 7008 or Femto for voltage or current amplification, and eventually to National Instrument NI-4461 cards. The NI-4461 DAQ cards are installed in a NI PXIe chassis. The electronics usually have special power supplies with 60 Hz-noise filtered and share a common grounding with the dilution refrigerator.

Coaxial lines are also necessary for transmitting AC signals from the built-in capacitor inside the strain cell to the Andeen-Hagerling capacitance bridge. For this purpose, superconducting coax cables (semi-rigid or miniature flexible) and thermo-coax cables are installed in the refrigerator, with LEMO connectors used at vacuum-sealed interfaces.

The computers controlling the GHS and data acquisition hardware are located in a separate room. There are cables as long as several meters running between the walls for communication between the computers and the hardware. Many of these cables are USB cables and at this length, USB repeaters are employed to magnify the signals and ensure data integrity. For the communication between the NI PXIe chassis and the computer, fiber MXI interface and suitable cables are employed.

2.5.2.2 Lock-in amplifiers

On computers, low frequency data are often processed with lock-in techniques. Lock-in amplifier is an instrument used extensively in laboratory researches, especially in the field of condensed matter physics. Lock-in is best for extracting weak signals reflecting physical properties that are buried in noise. Figure 27 illustrates the working principles of lock-in amplifiers. We start with an input signal (simplified to be single-frequency) pre-amplified by a factor g [173]:

$$V_I = g \cdot A_S \cdot \cos(2\pi f_S t + \phi)$$

,where A_S, f_S, and ϕ are the input signal's amplitude, frequency and phase respectively. This is multiplied by the reference signal represented by:

$$v_{RX} = cos(2\pi f_R t)$$

and a 90° phase-shifted version represented by:

$$v_{RY} = sin(2\pi f_R t).$$

The result, using the approximation that $f_S - f_R \ll f_R$ and $f_S + f_R \approx 2f_R$, can be simplified to give:

$$V_{MX} = V_I v_{RX} = 1/2gA_S\{cos(\phi) + cos[2\pi(2f_R)t + \phi]\}$$

and

$$V_{MY} = V_I v_{RY} = 1/2gA_S\{sin(\phi) + sin[2\pi(2f_R)t + \phi]\}.$$

Finally, V_{MX} and V_{MY} are fed through a low-pass filter with a time constant that is inverse of the cutoff frequency of the filter. The step gets rid of the second-harmonic $2f_R$ term, leaving the time-independent signal: $V_{OutX} = 1/2gA_S cos\phi$ and $V_{OutY} = 1/2gA_S sin\phi$. From those, A_S and ϕ can easily be deduced.

For a complex situation where the input signal is a mix of multiple frequencies, lock-in amplifying process exclusively extracts signals coherent with the reference frequency, which is also called synchronous detection.

Besides the low-pass filter as a part of the lock-in amplifier, other filters used in the research to improve signal-to-noise ratio include: notch filter, which rejects noise from the power line at 60 Hz, 120 Hz and 180 Hz; decimation or averaging over data points; zero phase low-pass filter, and Savitsky-Golay filter applied at the data analysis stage etc. [174, 175].

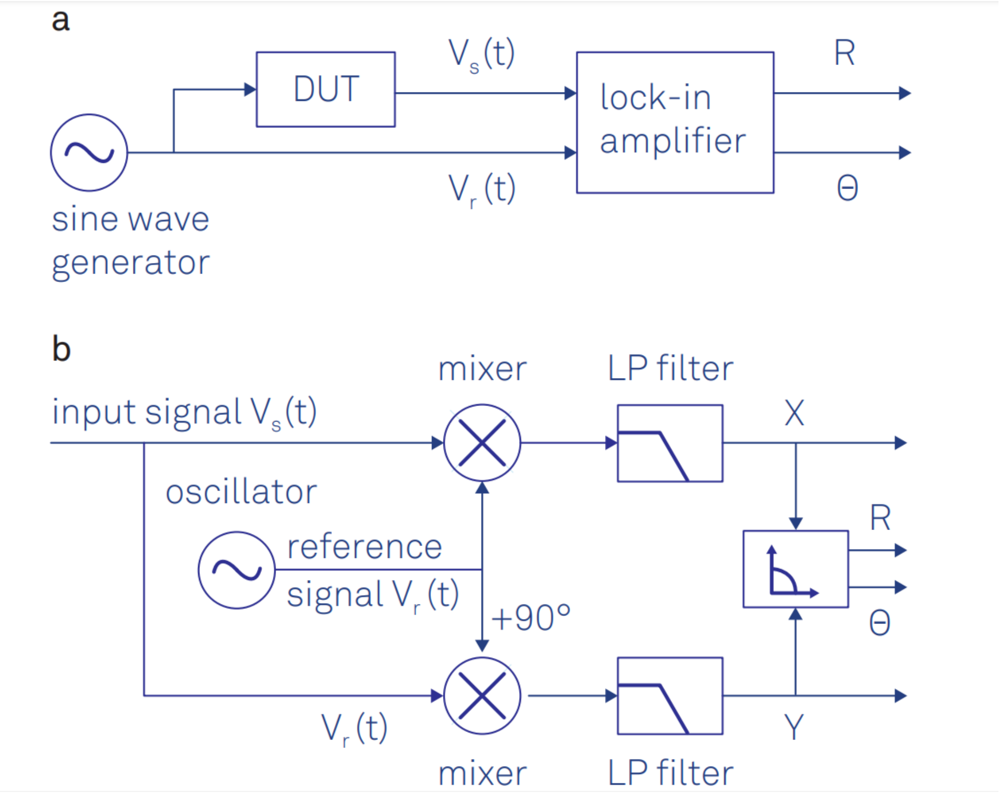

Figure 27: (a) Diagram of the lock-in amplification in the simple scenario of a sine wave as the input. A sinusoidal signal drives the device and also serves as a reference signal. The measured signal is analyzed by the lock-in to obtain its amplitude (R) and phase (θ). (b) Diagram of a typical lock-in measurement: the input signal is multiplied by a reference signal (generated from a separate oscillator of the desired frequency to lock) and a 90° phase-shifted version of the reference signal. The outputs are low-pass filtered and converted into X and Y values, from which R and θ can be calculated. Picture credit to: Zurich Instruments.

3.0 Breaking electron pairs in Pseudogap state in $SmTiO_3/SrTiO_3/SmTiO_3$ quantum wells

3.1 Introduction

The pseudogap phase is an unusual state of electronic matter which is associated with unconventional superconductivity in copper-oxide superconductors as well as superconducting semiconductors. It is characterized by a reduction in spectral weight near the Fermi energy, and generally appears above the superconducting transition temperature T_c in the low-doped regime. Understanding the pseudogap state has been the subject of intense focus for cuprate superconductors as it provides unique insights into correlated electron physics [6, 7, 113, 114, 115]. Besides cuprate superconductors, pseudogap behavior has also been found in heavy-fermion compounds [176], charge density wave systems [177], rare-earth nickelates [178], and ultracold atomic gas systems [179, 180]. Tunneling experiments have shown a clear gap feature in electrical transport [9, 181, 182]. Photoemission measurements are also used to probe the low-energy excitations of the electron system and revealed the Fermi surface to be “ gapped out ”, meaning that low-energy excitations only occupy disconnected segments known as Fermi arcs [183, 184].

The physical origin of the pseudogap phase continues to be debated. One particularly challenging question is whether the phase is related to pre-formed Cooper pairs. In the BCS-BEC crossover picture, fermionic incoherence is also brought up, and it is proposed that near quantum critical point, fluctuations can give rise to pairing but suppress superconductivity [185]. Disorder can also play a role in strongly correlated systems and has been shown in theory to induce a zero-energy anomaly [186] and stabilize a pseudogap state [187].

$SrTiO_3$ is one of a few semiconductors known to exhibit superconducting behaviour [35] and a domelike shape of T_c as a function of electron density [51]. It is considered to be an unconventional superconductor with an unknown pairing mechanism. Advances in understanding the nature of superconductivity in $SrTiO_3$ arose from heterostructures, in particular $LaAlO_3/SrTiO_3$ heterostructures [71, 72]. The interface system not only inherent from

$SrTiO_3$ properties including gate-tunable superconductivity to a quantum critical point[72], and gate-tunable pseudogap behavior past the low-density boundary of the superconducting "dome" [117]. Nanostructures formed at the $LaAlO_3/SrTiO_3$ interface show evidence for electron pairing without superconductivity [101]. Despite great efforts made for understanding the pseudogap phase in cuprates and $SrTiO_3$-based systems, it is far from clear that pseudogap phenomena arise from a single physical mechanism. In particular, mechanisms to describe pseudogap behavior in high-temperature copper oxide systems and in superconducting semiconductors based on as $SrTiO_3$ [188] may have disparate origins, despite the phenomenological similarities.

The hybrid Molecular Beam Epitaxy (hybrid MBE) growth technique has enabled new families of $SrTiO_3$-based quantum wells to be designed with high doping density and ultra-narrow widths. Similar to $LaAlO_3/SrTiO_3$, the quantum well systems containing rare-earth titanate/$SrTiO_3$ interfaces demonstrate a variety of emerging properties that can be tuned by quantum confinement, including metal-to-insulator transition [109], magnetism [139], quantum critical behaviour [140, 110], and a separation of transport and Hall scattering rates [110].

3.2 Experimental methods and results

Here, using a series of low-temperature transport and optical experiments, we examine whether this phase arises due to pre-formed electron pairs. We investigate the transport behavior of $SrTiO_3$ quantum wells when the system is driven out of equilibrium using two types of experimental methods: applying voltage biases exceeding the pseudogap energy and investigating the effects of the above-gap optical illumination on transport.

$SrZrO_3/SmTiO_3/SrTiO_3/SmTiO_3$ films used in the research were grown on $(La_{0.3}\ Sr_{0.7})(Al_{0.65}Ta_{0.35})O_3$ substrates using hybrid molecular beam epitaxy [139, 140], as detailed in Section 2.2. $SrZrO_3$ is deposited on top as a tunneling barrier for top-gated devices. The thickness of quantum wells in samples, as specified by the number of SrO planes contained in $SrTiO_3$ layers, is 2 SrO layers. Due to polar discontinuity, two $SrTiO_3/SmTiO_3$ interfaces in the quantum well each contribute to mobile carrier densities of $\sim 3.4 \times 10^{14}$ cm^2, leading to an expected total of $\sim 7 \times 10^{14}$cm^2 carriers spatially confined between insulating SmTiO$_3$ layers [139, 110]. In order to probe the transport properties, we fabricated Hall bar and tunneling devices using photolithography techniques (Section 2.2).

3.2.1 Characteristic pseudogap voltage measurements

To verify that our quantum well samples are in the pseudogap phase at low temperature and determine the energy scale, we first performed two-terminal current-voltage measurements. Current-voltage (I-V) measurements are performed in a Quantum Design Physical Property Measurement System at temperatures ranging from 50 mK to 300 K. Source voltages are generated using 24-bit Digital to Analog converter (DAC) National Instruments PXI-4461s, which simultaneously perform 24-bit Analog to Digital conversion (ADC) to collect current and current signals. The current is amplified by a transimpedance amplifier (model Femto DDPCA300) that also converts the current to voltage signals before being measured by PXI-4461s. Using several tunneling and Hall-bar devices on two samples, varying voltage bias and sweep directions, multiple I-V curves are obtained to ensure that the pseudogap features measured are reproducible.

Then, differential conductance spectra $\mathrm{d}I/\mathrm{d}V$ vs V and normalized conductance $\mathrm{d}(\ln I)/\mathrm{d}(\ln V) \sim (\mathrm{d}I/\mathrm{d}V)(I/V)^{-1}$ are obtained via numerical differentiation. Note that, by definition, (dI/dV) $(I/V)^{-1} \rightarrow 1$ as $V \rightarrow 0$. However, this is only true when the resistance is finite. Since in the sample, certain in-gap regions are completely insulating, the rule no longer holds. In tunneling spectroscopy, $\mathrm{d}I/\mathrm{d}V$ vs V is known to diverge exponentially with the drive voltage and the separation distance of the tunneling barrier [189, 190, 191]. Normalized conductance $\mathrm{d}(\ln I)/\mathrm{d}\ln V)$, which can be interpreted as a ratio of differential to total conductivity, eliminate the effect of the divergence and make it easy to compare density-of-state (DOS) characteristics of different device configurations.

Figure 28 (a) illustrates the dimensions of the quantum well structure. Figure 28 (b) shows the circuit diagram for I-V measurements between two transverse contacts of the Hall bar, electrodes 2 and 8. Hall bar devices contain eight ohmic electrodes in direct contact

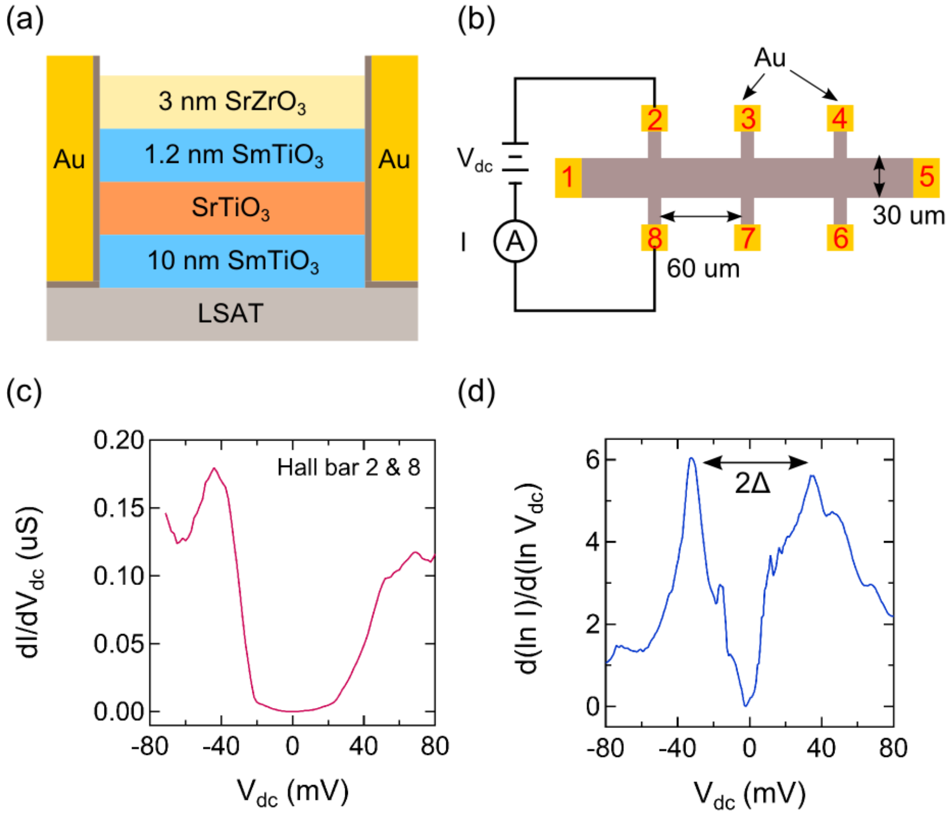

Figure 28: Device geometry and pseudogap features. (a) Cross sectional view of the $SmTiO_3/SrTiO_3/SmTiO_3$ quantum well structure. The thickness of the $SrTiO_3$ quantum well, defined by the number of SrO layers it contains, are 2 SrO layers. Ti (grey) and Au (yellow) contacts are made to be in direct contact with the conductive $SrTiO_3$ layer. (b)Schematic of the Hall bar device and the experiment setup for two-terminal current-voltage measurements between electrodes 2 and 8, separated at a distance of 90 μm. (c) Differential conductance spectra $\mathrm{d}I/\mathrm{d}V$ computed from I-V characteristic curves obtained using the setup in (b) shows a reduction of conductance near zero voltage and asymmetric coherence peaks. (d) Normalized conductance spectra $[\mathrm{d}\,(\ln I)/\mathrm{d}(\ln V)$ vs $V]$ indicates that the system is in the pseudogap phase . A gap with a characteristic voltage scale 40 mV is estimated.

with the 2DES in $SrTiO_3$ layers. Note that, in Figure 28 (b), the brown area does not reflect the real proportions of the hall bar, and the actual Hall bar design is described in Section 2.2. The corresponding I-V curves measured at T = 50 mK, when plotted as a derivative vs V_{dc}(Figure 28 (c)) and a logarithmic derivative vs V_{dc} (Figure 28(d)), show a well-defined gap, indicating a reduction of DOS around zero-bias, with coherence peaks on both sides. The positions of coherence peaks are used to estimate the characteristic voltage of the pseudogap as 40 mV. Observed characteristics point to a pseudogap phase as has been reported in earlier tunneling experiments by Marshall et al. [9].

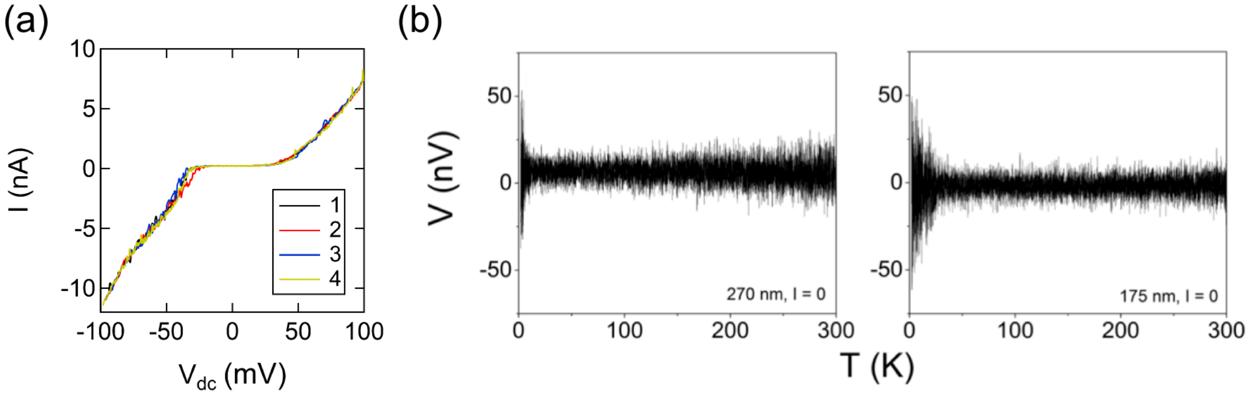

Figure 29: Current fluctuations (a) Four consecutive I-V characteristic curves measured at 50 mK between electrodes labeled 2 and 8 (placed 90 μm apart) show current fluctuations under the same voltage sources. (b) Unexpected voltage fluctuations that change with temperature are observed in $SmTiO_3/SrTiO_3/SmTiO_3$ quantum well samples with 10 layers of SrO (left, electrodes spacing distance is 270 nm) and 5 layers of SrO (right, electrodes spacing distance is 170 nm). (b) is adapted from Ref. [111].

Figure 29 (a) shows four I-V curves measured between electrodes 2 and 8 consecutively under the same experimental condition. Noticeably, current signals fluctuate when V_{dc} is near the gap energy. The result is consistent with the observation of temperature-dependent potential fluctuations at $I = 0$ in such quantum wells with a thickness of 5 layers of SrO, reported by Hardy et al. (Figure 29 (b)) [111] . Potential fluctuations increase under 20 K, only in thin quantum wells that are in the non-Fermi liquid regime, which is the same condition for pseudogap formation in the system.

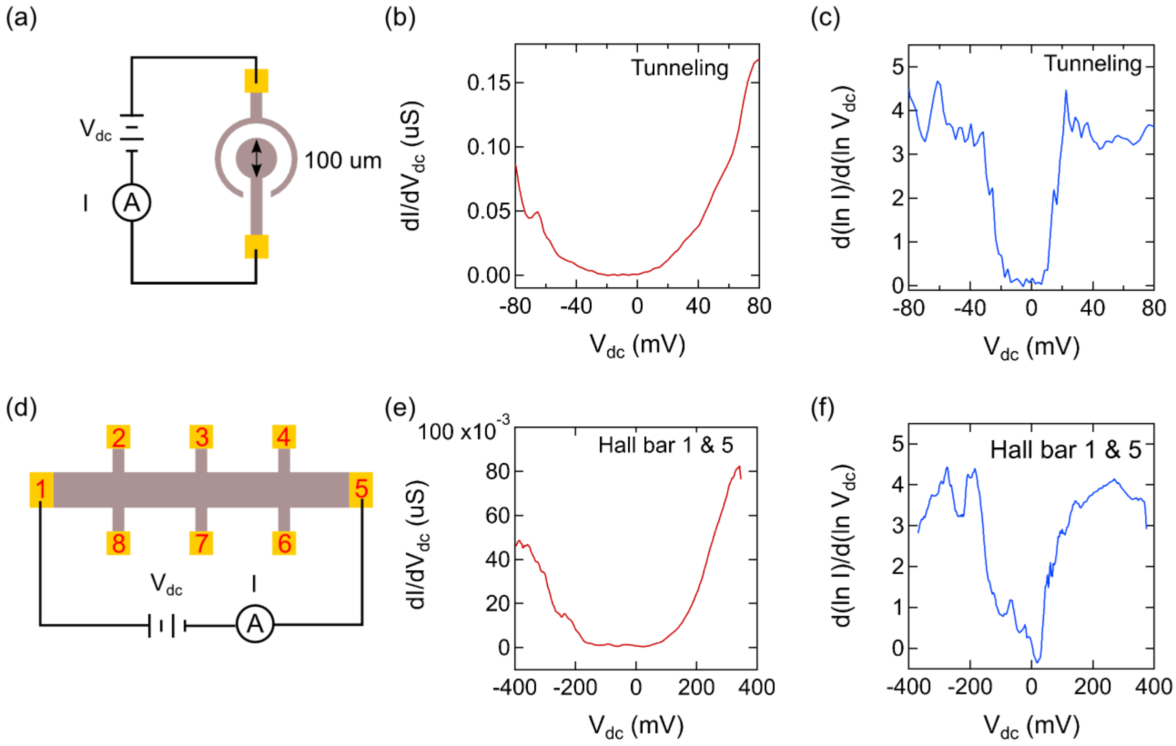

Figure 30: (a) Schematic of the tunneling device with the experimental setup for two-terminal I-V measurements between the top and interface electrodes, separated at a distance of 60 μm. (b)(c) Conductance spectra ($\mathrm{d}I/\mathrm{d}V$ vs V) and normalized conductance spectra ($\mathrm{d}(\ln I)/\mathrm{d}(\ln V)$ vs V) of the tunneling device measured at 2K. A pseudogap with a characteristic voltage of 27 mV is estimated. (d) Experimental setup for two-terminal I-V measurements in a Hall bar device between electrodes 1 and 5, separated at a distance of 240 μm. (e)(f) Conductance spectra of ($\mathrm{d}I/\mathrm{d}V$ vs V) and normalized conductance spectra ($\mathrm{d}(\ln I)/\mathrm{d}(\ln V)$ vs V) measured between electrodes 1 and 5 at 50 mK show a pseudogap with a characteristic voltage of 120 mV.

Figure 30 (a)(d) shows the circuit diagrams for low-temperature I-V measurements in a tunneling device (a) and between two longitudinal electrodes of the Hall bar, electrodes 1 and 5 (b).

Each tunneling device contains two electrodes. One electrode is connected to a metal gate deposited on top of $SrZrO_3$ (circular disk with diameter 100 μm), and the other is in di-

Table 4: Characteristic voltage of pseudogap as a function of separation distance between electrodes.

Device type	Separation distance (μm)	characteristic voltage of pseudogap (mV)	Voltage to distance ratio (mV/μm)
Tunneling	60	27	0.45
Hall bar	90	40	0.44
Hall bar	270	120	0.44

rect contact with the $SrTiO_3$ layers. The geometry enables us to use tunneling spectroscopy to map the pseudogap features in our samples. The separation distance between the two electrodes is 60 μm. In Figure 37 (b-c), the conductance spectra ($\mathrm{d}I/\mathrm{d}V_{dc}$) and the normalized $\mathrm{d}(\ln I)/\mathrm{d}(\ln V_{dc})$ obtained in the tunneling device again have a gap shape, with an estimated gap size 27 mV. Since this device geometry is standard for tunneling spectroscopy, we can deduce that the energy scale of pseudogap in the system is 27 meV.

Figure 30 (e)(f) shows results obtained from the same Hall bar device as the one measured to obtain Figure 28 (c)(d), but a different pair of longitudinal electrodes, spaced 270 μm apart, are used here. Overall the spectra appear quite similar with a valley and coherence peaks. However, a significantly larger width of the gap (∼120 mV) is observed. Table 4 put the characteristic voltages of the pseudogap and the separation distance between the electrodes for three data sets side by side and reveals that the two factors are proportional to each other.

3.2.2 Voltage excitation of quasi-particles

Non-equilibrium, non-local I-V measurements are performed along the main channel of the Hall bar, using a combination of ac or dc voltages applied between electrical contacts on the left-hand side of the Hall bar. The resulting currents and voltages between contacts on the right-hand side of the Hall-bar is measured, enabling four-terminal conductance $\mathrm{d}I/\mathrm{d}V$

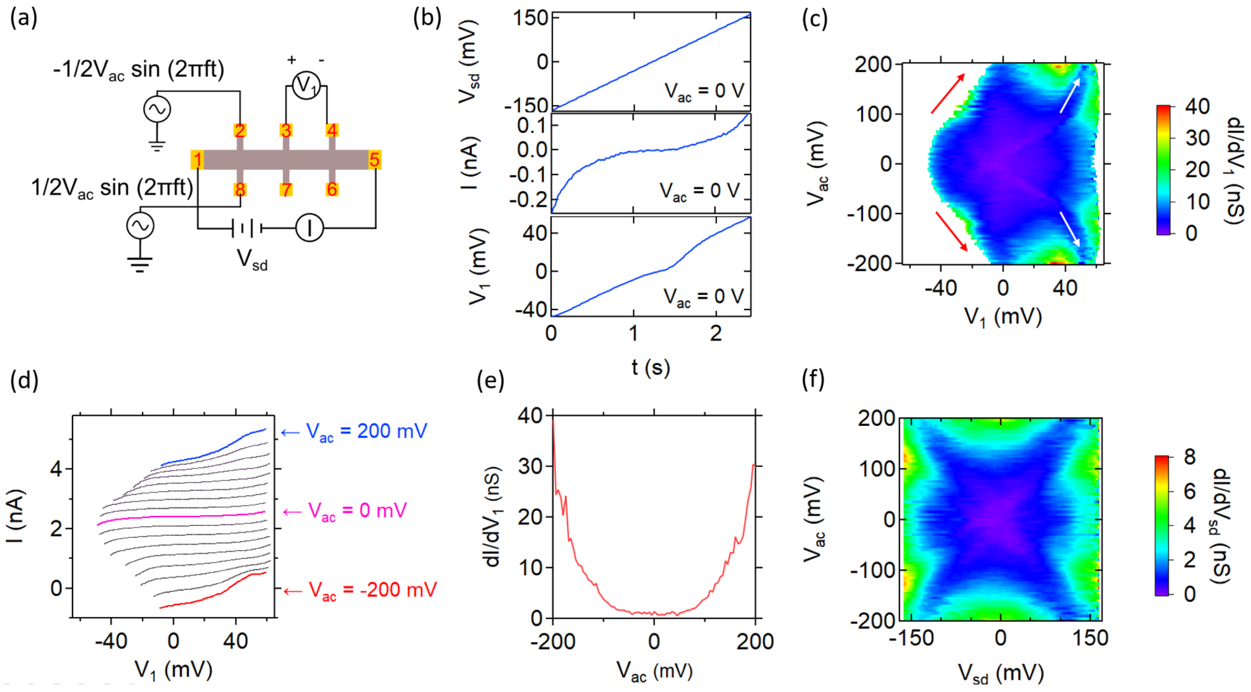

Figure 31: Non-equilibrium, non-local transport measurements using ac voltages for quasi-particle excitation. (a) Experimental setup. High-frequency ac voltages of magnitude $\frac{1}{2}V_{ac}$ and frequency $f = 1000$ Hz are applied to two electrodes labeled 2 and 8 on the left-hand side of the Hall bar device, with a phase difference of 180°. Simultaneously, a quasi-dc voltage V_{sd} applied from electrode 1 is swept slowly between -160 mV and 160 mV at different V_{ac} to generate a quasi-dc current along the main channel of the Hall bar. Four-terminal I-V_1 measurements between electrodes 3 and 4 are performed. (b) From top to bottom, panels of the figure plot V_{sd}, I (dc) measured from electrode 5, four-terminal voltage V_1 as a function of real time t when $V_{ac} = 0$ V. (c) Four-terminal differential conductance dI/dV_1 plotted as a function of V_{ac} and V_1. (d) V_1-I curves at different V_{ac} are displayed as a waterfall plot with vertical offsets. From bottom to top, the corresponding V_{ac} for those curves increase from -0.2 V to 0.2 V with a step size of 0.025 V. (e) dI/dV_1 at $I = 0$ nA at each V_{ac} plotted as a function of V_{ac} shows a gapped feature. (f) Two-terminal differential conductance dI/dV_{sd} plotted as a function of V_{ac} and applied voltage V_{sd}.

to be measured as a function of the dc and ac voltage amplitudes.

Figure 31 (a) is a diagram of the experimental setup using ac voltage for quasi-particle excitation. The applied ac voltage bias are sinusoidal waves with amplitude $\frac{1}{2}V_{ac}$ and frequency $f = 1000$ Hz, driven differentially on electrodes 2 and 8. Therefore, the potential difference between the two electrodes is a sinusoidal wave with amplitude V_{ac}. At the same time, a quasi-dc voltage source V_{sd} is applied on longitudinal electrode 1. The other longitudinal electrode 5 is grounded and a dc current I measure is measured from electrode 5. Four-terminal voltage between electrode 3 and 4 is measured as V_1. Figure 31 (b) shows that an the applied voltage V_{sd} is swept between -160 mV and 160 mV over a period of 2.4 s, which has a much slower frequency than the applied 1000 Hz ac voltage. In the middle and bottom panels of Figure 31 (b), measured I and V_1 is plotted as a function of time t when $V_{ac} = 0$ V. The V_{sd} sweep and I, V_1 measurements is performed at various V_{ac} between -200 mV and 200 mV. Figure 31 (c-e) track the four-terminal differential conductance dI/dV_1 between electrodes 3 and 4 as a function of V_1 and V_{ac}. We plot data as an intensity plot of $dI/dV_1(V_{ac}, V_{dc})$ (Figure 31 (c)), as well as I vs V_1 curves at different V_{ac} values, starting from -0.2 V with 0.025 V increment, displayed as waterfall plots with vertical offsets (Figure 31 (d)). At each V_{ac}, differential dI/dV_1 when $I = 0$ A is calculated and plotted as a function of V_{ac} in Figure 31 (e), revealing a gapped shape with the gap size estimated to be roughly 100 mV. We also plot an intensity plot of $dI/dV_{sd}(V_{ac}, V_{sd})$ (Figure 31 (f)) to show how the two terminal conductance changed with V_{ac}.

A number of observations can be made:

(i) Overall, as $|V_{ac}|$ increases, I increases, indicating that the Hall bar device becomes more conductive.

(ii) In Figure 31 (c), the lower bound of four-terminal voltage V_1 gradually shifts to positive values as as $|V_{ac}|$ increases, while the upper bound of V_1 almost doesn't change for all $|V_{ac}|$ values. The intensity plot is asymmetric with regards to V_1, which shares the same sign as the applied V_{sd}.

(iii) At $V_{ac} = 0$ V, the four-terminal I vs I curve has an zero slope at $I = 0$, corresponding to a gap-shaped dI/dV_1 vs I, as we expect for the pseudogap phase. For $|V_{ac}|$ <100 mV, as $|V_{ac}|$ increases, the slope at $I = 0$ nA in the corresponding V_1 vs I curve slowly increases

(Figure 31 (c)), though the shape of the corresponding dI/dV_1 vs I remains a gap.

(iv) At $|V_{ac}|$ >100 mV, dI/dV_1 at $I = 0$ nA increases significantly. A striking new high conductance area that centers at $V_1 \sim 40$ mV also emerges in Figure 31(c).

(v) The above effects is symmetric for positive and negative V_{ac}, as the ac voltage between 2 and 8 in the two cases can be considered almost identical but for a phase change 180°.

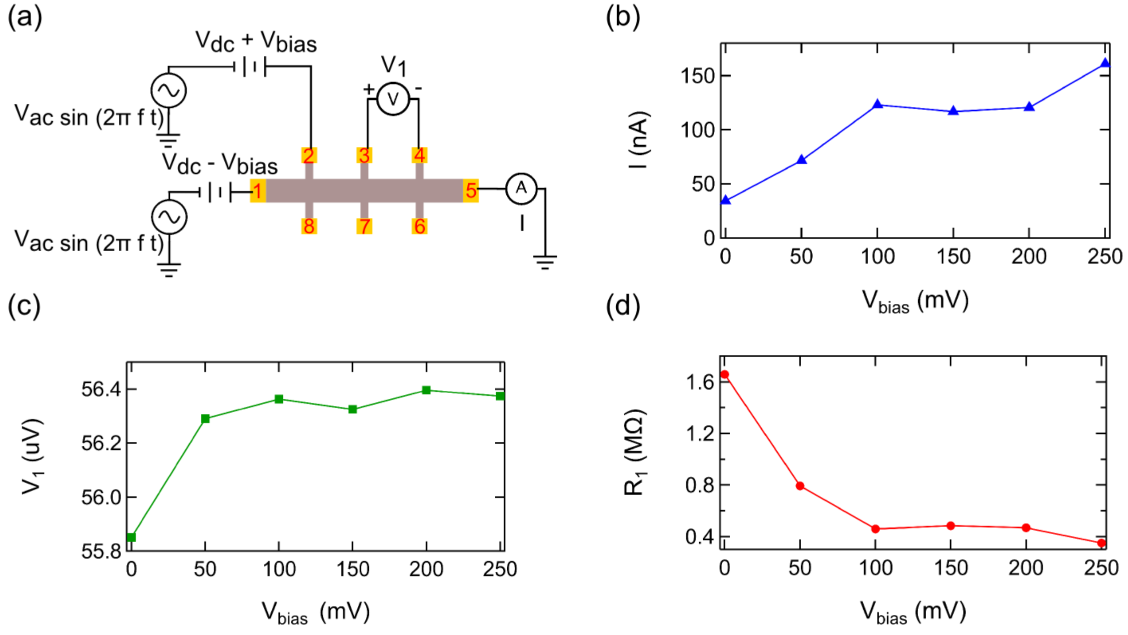

Figure 32: Non-equilibrium, non-local transport measurements using dc voltages for quasi-particle excitation. (a) Set up for the dc voltage excitation experiments. A voltage bias V_{bias} is applied between two contacts on contacts labeled 1 and 2 while four-terminal lock-in measurements are performed between contacts 3 and 4. (b) Current as a function of V_{bias}. (c) Four-terminal voltage as a function V_{bias}. (d) Four-terminal resistance $R = V_1/I$ as a function of V_{bias}.

Next, we show four-terminal conductance measurements at different dc voltages V_{bias}. Non-local transport experiments are performed (Figure 32) by driving a combination of a low dc bias V_{dc} combined with a differentially applied voltage V_{bias}, as depicted in Figure 32 (a). The V_{bias} driving induces a current between electrodes 1 and 2, while the resulting change in resistance along the main channel is measured “downstream“ by driving with V_{ac}

and measuring the resulting current at electrode 5 and voltage drop between electrodes 3 and 4. The measurement is non-local because changes in four-terminal conductance are influenced by an excitation in a region outside of where the voltage drop between electrodes 3 and 4 are measured.

Since electrode 1 and 2 are not identical, we assume V_{bia} also provides an effective dc voltage V_E relative to the grounded drain electrode 5. The magnitude of V_E should be proportional to the magnitude of V_{bias}. Meanwhile, a sinusoidal voltage source with amplitude $V_{ac} = 20$ mV and frequency $f = 13$ Hz as well as a small dc voltage $V_{dc} =$ -40 mV are applied to both source contacts to enable lock-in measurements of current I and four-terminal voltage V_1. In Figure 32 (b), we observe that current first increases as V_{bias} increases from 0 to 0.2 V, stays the same until V_{bias} reaches 0.4 V, and then increases again with V_{bias}. Meanwhile, four-terminal voltages remain relatively stable. Four terminal resistance $R = V_1/I$ in Figure 32 (d) decreases when current increases. Multiple configurations using different electrodes as source/drain and different amplitudes for V_{dc} (20 mV, -40 mV) are adopted and generate similar trends.

3.2.3 Photoexcitation of quasi-particles

Photo-induced conductivity changes within the $SmTiO_3/SrTiO_3/SmTiO_3$ quantum wells are investigated by illuminating the Hall bar with a continuous-wave He-Ne laser or a pulsed laser. He-Ne laser operates at a wavelength of $\lambda = 632.8$ nm, corresponding to a photon energy $E = h * c/\lambda = 1959$ meV, substantially larger than the pseudogap energy.

Figure 33 compares the results for two-terminal measurements of the main channel of the Hall bar, with and without laser. The experiment is conducted in an optical cryostat system (Montana Cryostation), where the sample is cooled down to 4.6 K. A setup schematic is shown in Figure 33 (a). Current-voltage are performed as a function of the ac amplitude V_{ac} (frequency $f = 2.37$ Hz), where the dc bias is set to zero (Figure 33 (b)). We found that He-Ne laser illumination with an estimated intensity $\sim 1 \times 10^6$ W/m^2 induces an increase in current at all V_{ac} and $V_{dc} = 0$ V, suggesting optical quasi-particle excitation. The measurements are repeated using multiple laser intensities to ensure reproducibility of the

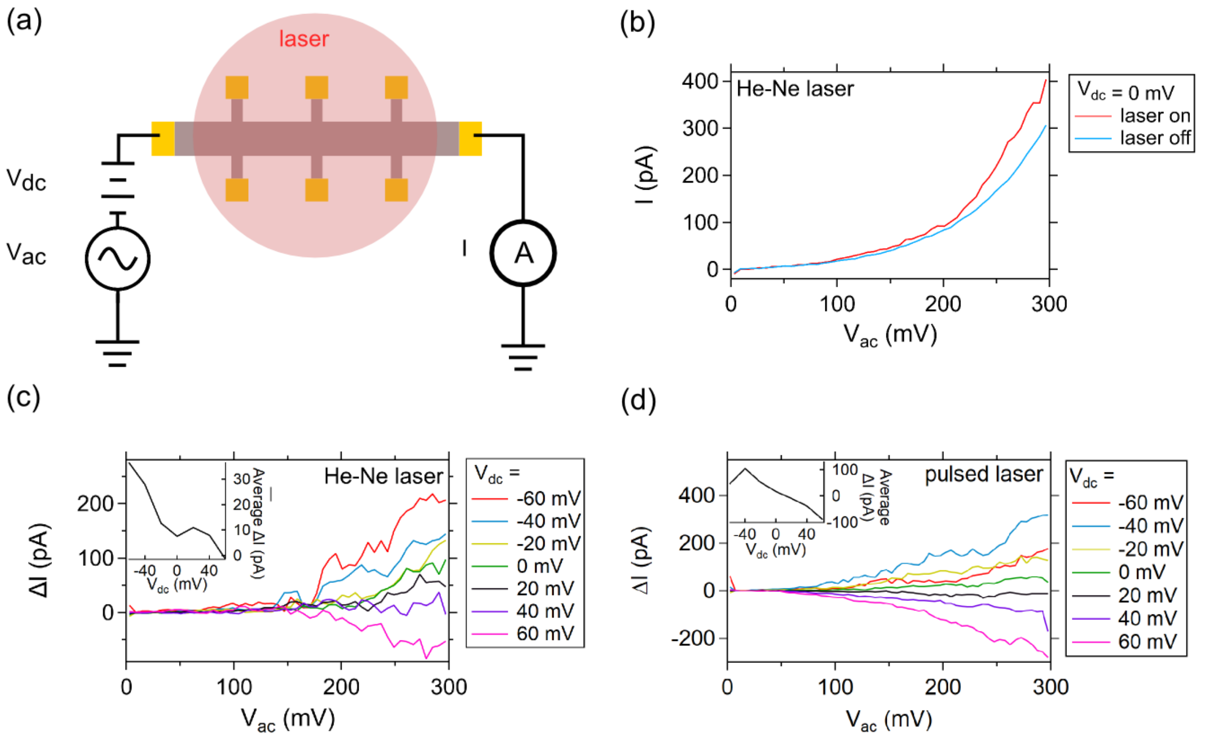

Figure 33: Transport measurements probing photon-induced quasi-particle excitation. (a) Diagram of the setup for the two-terminal Lock-in experiments with laser illumination. (b) Current vs V_{ac} voltage curves show that the system is consistently more conductive with the He-Ne laser illumination at $V_{dc} = 0$ V. (c) He-Ne-laser-induced change in current $\Delta I = I_{HeNe} - I_{laser_off}$ as a function of V_{ac} at different V_{dc} ranging from -60 mV to 60 mV. An insert plots the average ΔI (over 0V $< V_{ac} <$ 300 mV) as a function of V_{dc}. (d) Pulsed-laser-induced change in current ΔI as a function of V_{ac}, with an average ΔI vs V_{dc} plot inserted.

results.

In Figure 33 (c), we plot the difference in current at each V_{ac} with and without He-Ne laser illumination ($\Delta I = I_{laser} - I_{laser_off}$) vs V_{ac} for several dc bias V$_{dc}$ (-60 mV, -40 mV, -20 mV, 0 mV, 20 mV, 40 mV, 60 mV). Overall, photoconductive effects are observed above a threshold of about 150 mV. Average ΔI is calculated by averaging over 0 V $< V_{ac} <$ 300 mV and plotted against V_{dc} in an insert of Figure 33 (c). ΔI is the largest and has mostly positive values at V_{dc} = - 60 mV. It becomes negative at V_{dc} = 60 mV. We observe the trend for ΔI to decrease as V_{dc} increases. The feature eliminates light-induced sample heating as the primary cause for the change in I, since the heating effect should be identical for all curves.

In Figure 33 (d), we plot the results for transport measurements conducted similarly but using a pulsed laser (also providing photon with above-gap energy) instead of a He-Ne laser, using a different wavelength range and light intensities. The results reveal the same trends: photo-current increases with V_{ac} and decreases with V_{dc} (except for when V_{dc} = -60 mV).

Figure 34 (a) shows an alternative method to measure photocurrent using a mechanical chopper and a lock-in amplifier (model SR830). With a dc source voltage V_{dc} applied to one electrode, current I from another electrode is measured with a lock-in amplifier (model SR830), locked to the frequency of a mechanical chopper. From Figure 34 (b), the photo-current is again observed above the threshold of $V_{dc} >$ 150 mV. This agrees with the observations made for Figure 34 (b)(c), demonstrating the internal connection of the two optical methods. The optical effects gradually fade away as temperature increases. At temperatures above 20 K, the photo-current is almost completely gone.

3.3 Discussion

Electrical transport in these quantum wells takes place in the narrow $SrTiO_3$ layers, which contain only a few unit cells in the vertical direction [9]. It makes sense to build upon the rich knowledge about $SrTiO_3$ to further the understanding the quantum wells. Bulk $SrTiO_3$ is discovered to be an unconventional superconductor, inexplicable by the conventional BCS theory [38, 192], as described in depth in Section 1.1.3. In $SrTiO_3$, electron pairs in non-superconducting states has been observed [101, 102].

The pseudogap phase is believed to be closely linked to electron pairs [5, 193], since the pseudogap phase is oftentimes a competing phase for the superconducting phase, for which electron pairs is widely known. A relatively new BEC-BCS crossover theory is proposed, which describes the formation of strongly-bonded electron pairs that can exist even in non-

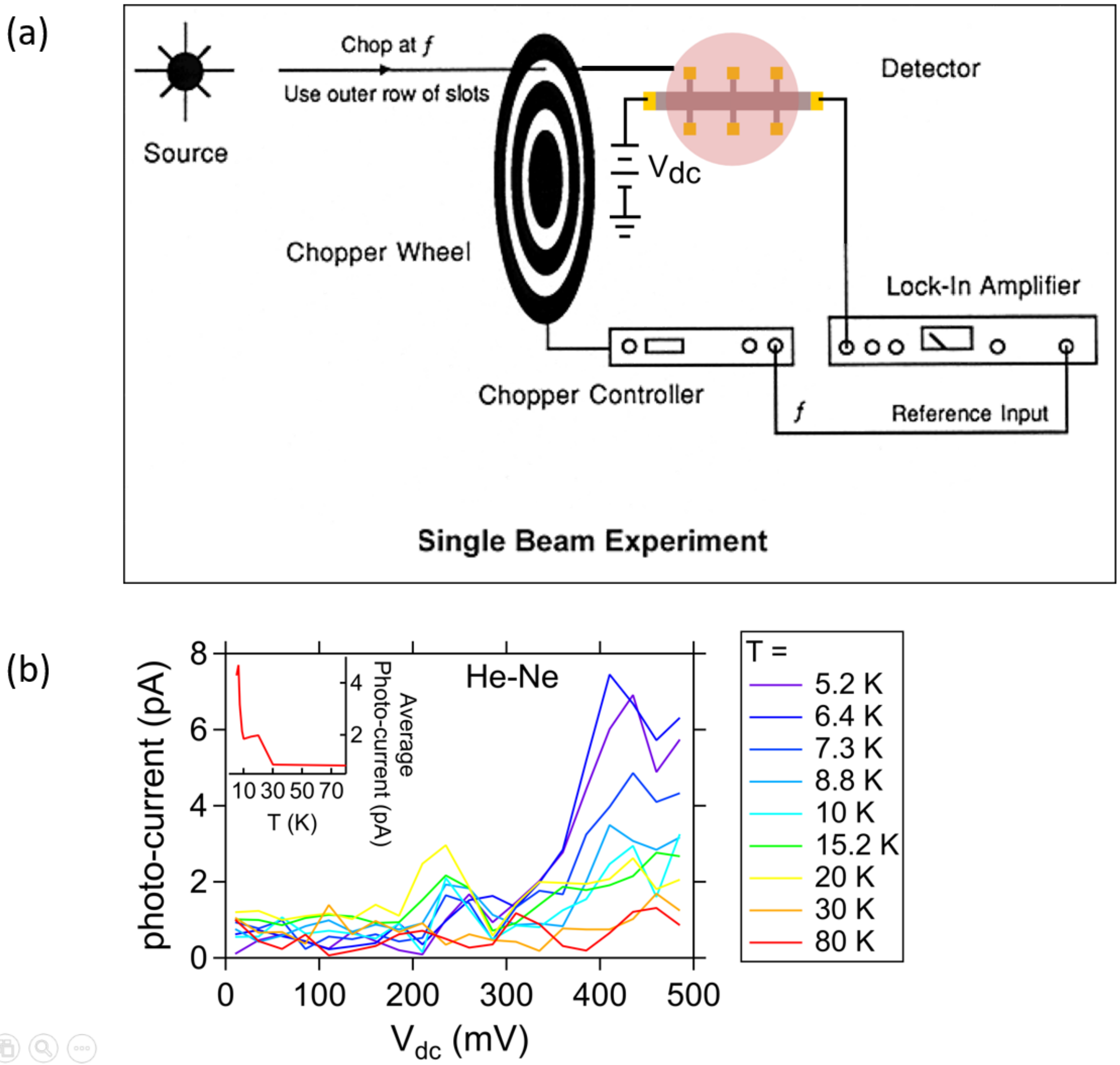

Figure 34: (a) The setup for lock-in measurements of photo-current using a mechanical chopper. A source voltage V_{dc} is applied to one longitudinal electrode in the Hall bar, and current is measured with a lock-in amplifier (SR830). Meanwhile, a He-Ne beam is being chopped by the chopper, and the reference frequency from the chopper controller is input into the lock-in amplifier to lock the current signal to get photo-current. Modified from a diagram credit to Stanford Research Systems.(b) photo-current as a function of V_{dc} at different temperatures from 5.2 K to 80 K.

superconducting states, including the pseudogap state [5]. However, these pairs are localized in the pseudogap phase, unless an input of energy can split up the pairs into single electrons, creating fermionic excitations.

Evidence of electron-pairing in non-superconducting states has been discovered in several $SrTiO_3$-based materials, including Zr-doped bulk $SrTiO_3$ [194] and nanowires in $LaAlO_3$/ $SrTiO_3$ [101, 102]. Electrical transport in the $SrTiO_3$ quantum wells takes place in the narrow $SrTiO_3$ layers. Therefore, the quantum wells is likely to have similar mechanisms with other $SrTiO_3$-based materials, leading to speculation of the existence of electron pairs in the $SmTiO_3/SrTiO_3/SmTiO_3$ quantum wells.

Experiments described in Section 3.2, where voltages and photons are employed for fermionic excitations, provide circumstantial evidence for long lasting quasi-particle excitation in $SmTiO_3/SrTiO_3/SmTiO_3$ quantum wells.

From the normalized conductance spectra of the standard tunneling device (Figure 30 (c)), we find the pseudogap energy to be 27 meV in the quantum wells, which is very close to the pseudogap energy reported for this material by Marshall et al. [9]. We cross-examine the pseudogap energy found in the $SrTiO_3$ quantum wells with the pseudogap energy found in another $SrTiO_3$-based heterostructure, $LaAlO_3/SrTiO_3$ [117]. The energy scale of pseudogap in $LaAlO_3/SrTiO_3$ is reported to be 40 μeV, which is three orders of magnitude smaller than the pseudogap energy in the quantum wells. This indicates an unusually large force binding localized pairs in the quantum wells, and possibly arises from electron confinement. The electron system at the interface of $LaAlO_3$ and $SrTiO_3$ can spread several μms deep into the $SrTiO_3$ side, while the electron system in the quantum wells is confined to within a few nanometers in the vertical direction.

In table 4, the fixed ratio between the characteristic voltage of pseudogap and the separation distance between electrodes in two-terminal *I*-*V* measurements are intriguing. The ratio, which is calculated to be 4.5 $\times 10^5$ V/m, may be interpreted as the critical electric field to excite quasi-particles. Excited quasi-particles are likely to recombine into immobile pairs after existing for a period of time and traveling over some distances, and new pairs can be split up again under the disturbance of voltage to continue the transport. For longer separation distance between electrodes in the horizontal direction, the cycle of electron splitting and recombining needs to occur more times on average, thus, the characteristic voltage should to be larger.

Our approach to understanding results for the non-equilibrium measurements using ac voltage for excitation (Figure 31) begins with identifying two situations: when the ac voltage is larger or smaller than a characteristic pseudogap voltage. We deduce the characteristic voltage to be 100 mV, since a four-terminal conductance spectra deviates from the pseudogap characteristics when the ac voltage is larger than 100 mV. For ac voltage $>$ 100 mV, quasi-particle excitation is expected to occur in one part of the Hall bar. At ac voltage $>$ 100 mV, the four-terminal conductance spectra deviates from pseudogap characteristics with significantly higher conductance at $I = 0$ nA. Assume that quasi-particle excitation occurs in one part of the Hall bar and generates charge carriers. The observation of increased conductance in another part of the Hall bar supports that they are mobile carriers with a sufficient life time. Moreover, the sign of the charge the quasi-particles carry can be deduced to be negative. Under a negative dc drive voltage, quasi-particles with negative charge drift "downstream" into the region where the four terminal voltage V_1 is measured. Therefore, the region becomes more conductive and the magnitude of V_1 is reduced, consistent with the observation that the lower bound of V_1 moves closer to zero as $|V_{ac}|$ increases. Under a positive dc drive voltage, quasi-particles drift in the opposite direction and won't change V_1, consistent with the observation hat the upper bound of V_1 doesn't change with $|V_{ac}|$. The characteristic voltage 100 mV derived in the ac excitation results is in the same order of magnitude as and moderately larger than the characteristic voltage 40 mV derived from the two-terminal I-V measurements. The former being larger makes sense given the requirement for the quasi-particles to have a long lifetime for the non-local measurements.

Similarly, results for the non-equilibrium transport measurements using dc voltage for excitation (Figure 32) can be explained. When the dc voltage V_{bias} is larger than 50 mV, it can provide the energy necessary for quasi-particle excitation in one part of the Hall bar. Then, the dc potential in the main channel of the Hall bar, which would be a combination of V_E and V_{dc}, drives those quasi-particles to the other part of the Hall bar to be detected as a decrease in four-terminal resistance. When the dc excitation voltage V_{bias} is sufficiently large, $V_E + V_{dc}$ also exceeds the pseudogap characteristic voltage along the main channel, generating more quasi-particles, causing the four-terminal resistance to decrease further.

Next, we discuss the optical phenomena: a temperature-dependent photocurrent that appears when there is a sufficiently large drive voltage (larger than 150 mV) in the main channel (Figure 33, 34) in the context of photoexcitation of quasi-particles. The photocurrent is only present at temperature lower than 20 K, which is also the temperature condition for the pseudogap phase to be observed. The co-existence suggests an internal connection between the photocurrent and the pseudogap phase. The photon energies, converted from the wavelengths, are significant larger than the pseudogap energy in the system, sufficient for exciting quasi-particles. But quasi-particles possibly recombine into immobile pairs after a period of time, undetectable by the transport measurements using two electrodes separated 270 μm in the horizontal direction, unless a sufficiently large voltage exists in the main channel to facilitate the splitting and recombination of pairs. The different amplitudes and signs of photon-induced current change ΔI in Figure 33 (c) (d) as a function of a dc voltage V_{dc} again suggest that those quasi-particles carry negative charges. Under a negative dc voltage (E.g. -60 mV), the quasi-particles will drift closer to the drain electrode, making it easier for them to contribute to the current measured. A positive dc voltage is expected to drive quasi-particles away from the drain electrode, causing a depletion of mobile carriers near the drain electrode and a decrease in current.

With both the voltage and optical excitation approaches, the results show that mobile negatively-charged quasi-particles are created by electrical and optical excitation, The results presented thus far are consistent with a scenario in which immobile pre-formed electron pairs exist in the pseudogap phase and can be split up to generate extra mobile carriers by driving the system out of equilibrium.

3.4 Summary

Strongly correlated, two-dimensional electron liquids in $SmTiO_3/SrTiO_3/SmTiO_3$ quantum well structures exhibit a pseudogap phase when the quantum well width is sufficiently narrow. The nature of the pseudogap phase has not be determined. The pseudogap phase has been found in other $SrTiO_3$-based materials with much smaller pseudogap energies, and in those materials has been associated with electron-pairs without superconductivity. Through our experiments, evidence that favors the pairing interpretation of pseudogap has been discovered by breaking up electron pairs in two different ways. In one approach, we electrically drive the system out of equilibrium with applied voltages that exceed the pseudogap energy, and examine local and non-local changes in transport that may arise from quasi-particles excited above the pseudogap. In another approach, the quantum well is excited optically with visible-wavelength light, and changes in four-terminal longitudinal conductance are measured and analyzed. The suggested mechanism most consistent with the data involves breaking strongly bound immobile electron-pairs in the pseudogap phase. This work helps to consolidate behaviours of several $SrTiO_3$-based geometry and provides new insights into electron-pairing. It also highlights the need for an improved understanding of the mesoscopic electron properties in complex oxides that are unconventional Fermi liquids, such as the role quantum confinement plays in increasing the energy scale of pseudogap.

4.0 Toggling superconductivity with uniaxial strain in nanowires at $LaAlO_3/SrTiO_3$ interface

4.1 Introduction

Although $SrTiO_3$ was the first oxide superconductor discovered [35], the origins of its superconductivity continue to be a subject of debate [38, 195, 196, 37, 197, 198], puzzling researchers for five decades. $SrTiO_3$ is known as one of the most "dilute" superconductors, hosting superconductivity with carrier densities as low as $\sim 10^{15}$ cm^{-3} [197, 37]. This low carrier concentration implies a small Fermi energy, and phonon doesn't match up in a high Fermi energy that puts the system in an anti-adiabatic limit, which are at odds with the Bardeen-Cooper-Schrieffer (BCS) theory. The superconductivity in $SrTiO_3$ has many features that resemble those observed in high-temperature superconductors, such as the superconducting dome as a function of carrier density [35, 38].

Of the many theories proposed for the superconducting mechanisms in $SrTiO_3$ [50, 51, 52, 64, 65, 3], hypotheses related to structural phase transitions: ferroelectricity or ferroelasticity are gaining traction. Undoped $SrTiO_3$ is an incipient ferroelectric, but can be tuned towards ferroelectricity by electric field [42], cation (Ca, La) or oxygen isotope substitution [46, 47, 48] and hydrostatic pressure or strain [43, 44, 45, 15]. Most notably, the shift towards ferroelectricity is found to be accompanied by carrier density change and enhanced superconductivity [13, 15]. Therefore, pictures linking superconductivity to the ferroelasticity quantum critical point through quantum-critical fluctuations or hardening of phonon modes are proposed [49, 24, 65, 64]. Bulk $SrTiO_3$ has a cubic lattice structure at room temperature, but undergoes a phase transition into a tetragonal structure, forming ferroelastic domains a low temperatures [21]. Several experimental studies have suggested that ferroelastic domains plays an important role in the superconducting state [17, 199, 30], as described in Section 1.1.2.

Application of strain has been one of the most powerful methods for studying the superconductivity in $SrTiO_3$, due to its ability to directly influence ferroelastic domains and to induce a crossover between a paraelectric phase and an incipient ferroelectric phase [10, 11, 12, 13, 16, 15, 54]. Application of tensile or compressive strain at cryogenic temperatures using instruments based on piezoelectric stacks [162, 200] can be used to probe changes in superconducting state. With the technique, it has been discovered that superconducting transition temperature T_c in Nb-doped $SrTiO_3$ increased 50% under an external tensile strain of 0.05% [10].

In the chapter, we study the strain effects on superconducting nanowires in the conducting interface between a thin layer of $LaAlO_3$ and TiO_2-terminated $SrTiO_3$. The heterostructure material has aroused great interests from researchers with many unexpected properties, such as high-mobility 2D electron gas [59], superconductivity [71, 201, 117, 100], magnetism [202, 76] and Rashba spin-orbit [74, 203]. In the system, when the $LaAlO_3$ layer is of thickness 3.4 u.c., the 2D electron gas at the interface can be tuned to go through a local metal-to-insulator transition using c-AFM lithography [4], enabling the creation of superconducting nanowires. Pai et al. [17] has revealed the quasi-1D nature of such superconducting nanowires. The results from experiments are consistent with that superconductivity exists on the conductive channel edges, and co-located with ferroelastic domain boundaries. More evidence for the connection between ferroelastic domain boundaries and electron pairing mechanism has been discovered in $LaAlO_3/SrTiO_3$, in non-superconducting paired states [102, 101].

4.2 Experimental methods

To elucidate the effects of external strain on superconductivity at the interface of $LaAlO_3$ $/SrTiO_3$, we apply uniaxial compressive and tensile stresses to thin bars of $LaAlO_3/SrTiO_3$ and measure low-temperature transport behavior in c-AFM created conductive channels. Our experimental setup contain a cryogenic strain cell [200], as shown in Figure 35 (a), which contains three piezoelectric actuators. Applying positive or negative voltages on each piezoelectric actuator extends or shrinks the actuator. Extending the outer two actuators and shrinking the central actuator stretches the sample, while shrinking the outer two actuators and extending the central actuator compresses the sample, as detailed in Section 2.4. To mount a sample, the two ends of the sample are glued using epoxy to two washers underneath, which are bolted to the strain cell, as illustrated in Figure 35 (b-c). One washer moves with the outer piezoelectric actuators, and the other washer moves with the central piezoelectric actuator so that a tunable uniaxial stress can be applied along the long side of the sample. This allows for the displacement of the sample edges as piezo-stacks expand or shrink. The resulting displacement is provided by a parallel plate capacitor built-in the strain cell.

A global strain in the sample is defined as the measured displacement at the edges of the sample, divided by the sample length. In one instance. the global strain is calibrated to be around ± 0.03 % for a 5 mm × 5 mm × 0.1 mm sample mounted on the strain cell that is driven to its full capacity at 50 mK. For different samples, slight variations in sample sizes and the conditions of epoxy can change the range of the global strain, but the order of magnitude should still apply.

We focus on investigating the conductive channels formed at the $LaAlO_3/SrTiO_3$ interface using c-AFM lithography, $LaAlO_3/SrTiO_3$ heterostructures are grown by PLD with growth parameters detailed in Section 2.1. $SrTiO_3$ substrates are chosen to be 100 um, the thinnest commercially available type, making it easier to strain them. The thickness of $LaAlO_3$ are fixed to 3.4 u.c., the critical thickness for the metal-to-insulator transition. Electrical contacts to the interface are made by Ar+ etching (25 nm) followed by sputter depositing Ti/Au (4 nm/25 nm) (Section 2.1). Conductive nanostructures at the interface are subsequently created using c-AFM lithography, by moving an AFM tip with a positive voltage (15 $\sim$ 22 V) across the surface of the grounded sample, as detailed in Section 2.3. The devices created for this research are nanowires devices, each with at least four leads to allow for four-terminal measurements. According to previous researches involving the same interfacial material and c-AFM lithography method, the width of nanowires are calibrated to be in the nanometer scale [4, 17].

After the c-AFM lithography, the devices are transferred into a dilution refrigerator and cooled to $T \sim 60$ mK, below the superconducting transition temperature T_c without any applied stress. We then drive the strain cell by applying voltages to one or both piezo-stacks. Small regions where devices are located are under stress. We define the strain at

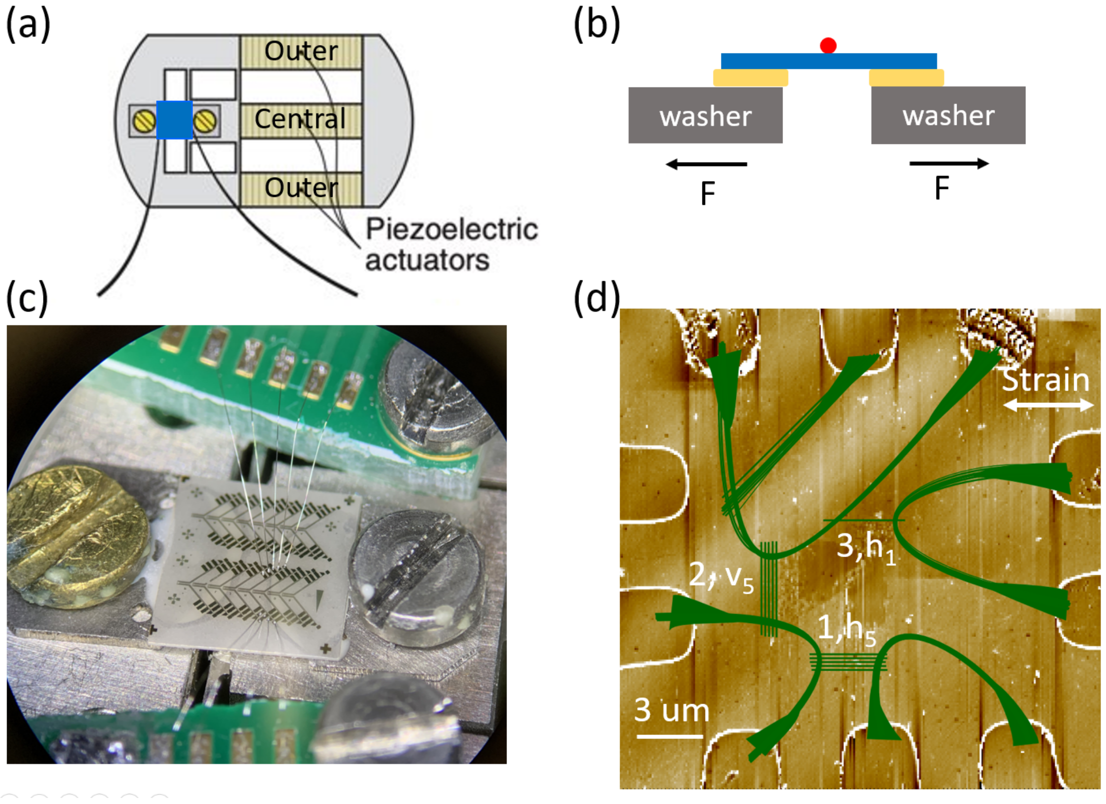

Figure 35: (a) Strain cell apparatus configuration. (c) A thin rectangular $LaAlO_3/SrTiO_3$ sample (at the center of the image, $5 \times 5 \times 0.1$ mm^3 in size) is attached to washers with epoxy. Two washers are fastened to the strain cell with screws. The sample has gold electrical contacts to the $LaAlO_3/SrTiO_3$ interface and is wire-bonded to two PC Boards, to enable the probing of transport properties of interfacial nanowire devices. (b) Side view of the $LaAlO_3/SrTiO_3$ sample (blue) mounted on two washers (grey) using epoxy (yellow). The red dot on the sample denotes the rough location for c-AFM lithography-created nanowire devices. (d) Device at the $LaAlO_3/SrTiO_3$ interface consists of three devices of nanowires, in directions parallel to the uniaxial strain (5 wire, labeled 1, h_5), perpendicular to strain (5 wires, 2, v_5), and parallel to strain (1 wires, 3, h_1). All three devices have the same length, $L = 3$ μm. Green areas depict conductive regions. The background is a AFM-scanned topography image of the canvas surface.

the location of a nanowire device as a local strain, and the local strain is believed to be the direct cause for any strain-induced changes in the transport properties of the nanowire. Despite lack of a direct way to measure this local strain, it is likely to be in the same order of magnitude as global strain. The global strain should be proportional to the voltages on the piezo-stacks, so does the local strain. Therefore, we sometimes use outer piezo-stack voltage V_{PO} to indicate uniaxial local strain qualitatively.

4.3 Results

In the section, we present the results of the effects of external uniaxial stress on superconductivity in three different samples. Local strain is hard to quantify and the effects of strain are rich and complex. We perform transport experiments on multiple samples, then select the results from three representative samples to analyze. We categorize the effects of strain into two kinds: non-hysteretic responses to the strain and hysterestic responses. The former kind is derived from sample A, when a smaller range of strain is applied. The latter kind is mainly derived from sample B and C, when a larger range of strain is applied.

4.3.1 Non-hysteretic responses to the strain

In sample A (5 mm × 5 mm × 100 μm), experiments characterizing the effects of strain in superconductivity is performed on three nanowire devices shown in Figure 35 (d). The devices considered here consist of three devices in series (which are subsequently referred to as (1, h_5), (2, v_5), and (3, h_1)): from the bottom, a device of five nanowires, spaced 200 nm apart, all aligned parallel to the uniaxial strain direction (1, h_5); to the middle, a device of five nanowires spaced 200 nm apart, all perpendicular to the strain direction (2, v_5); and to the top, a single nanowire, parallel to the strain direction (3, h_1). All three devices have the same length L = 3 μm. Each devices can be monitored independently or simultaneously. Transport experiments is done in a dilution refrigerator at 55 mK, which is below the superconducting phase transition temperature T_c for the sample ($\sim$ 290 mK).

For sample A, we drive the strain cell only with the outer piezo-stack since the central piezo-stack is broken at the time of the experiments. The maximum global tension corresponds to when the outer piezo-stack voltage equals 200 V, while the maximum global compression corresponds to when the outer piezo-stack voltage equals to -200 V. As elaborated earlier, the variable most relevant to the nanowire devices is the local strain, which should be proportional to the global strain and the outer piezo-stack voltage.

Four-terminal *I*-*V* curves are measured in sample A for all three devices during compression -to-tension and tension-compression continuously stress sweeps. A selection of *I*-*V* curves under different strain states are plotted in waterfall plots with offsets in y axis determined by the outer piezo-stack voltage (Figure 36 (a-c)). From these *I*-*V* curves, four-terminal resistance vs current curves are derived via numerical differentiation and plotted against the outer piezo-stack voltage in intensity graphs (Figure 36 (d-f)). Four-terminal resistance vs four-terminal voltage curves are also plotted against the outer piezo-stack voltage in intensity graphs (Figure 36 (d-f)). All figures in Figure 36 correspond to data taken when the strain is continuously changed from compression (-200 V) to tension (200 V).

No obvious hysteresis is observed in sample A. To show this, in Figure 37, four-terminal resistance vs current at different outer piezo-stack voltages when the strain is continuously swept from tension (200 V) to compression (-200 V) for device (1, h_5) and (2, v_5) wires are plotted. Figure 37 (a) and Figure 36 (d) are almost identical. The same goes for Figure 37 (b) and Figure 36 (e), despite the different directions in which the stress is swept. In device 3, hysteresis is also not observed (not plotted here).

A number of novel strain-induced phenomena are present from Figure 36, 37 at zero magnetic field.

(A) In device (1, h_5), strain moderates the height of coherence peaks, making them asymmetric with respect to current, as shown in Figure 36 (d,g) and Figure 37 (a). Coherence peaks are the peaks located right outside of the superconducting gap and usually indicate the accumulation of single electron density of state. Compression makes the coherence peak on the negative current side more prominent, at the same time diminishes the peak on the positive current side. Tension has the opposite effects.

(B) In device (2, v_5), strain induces a secondary peak and a valley outside of the original

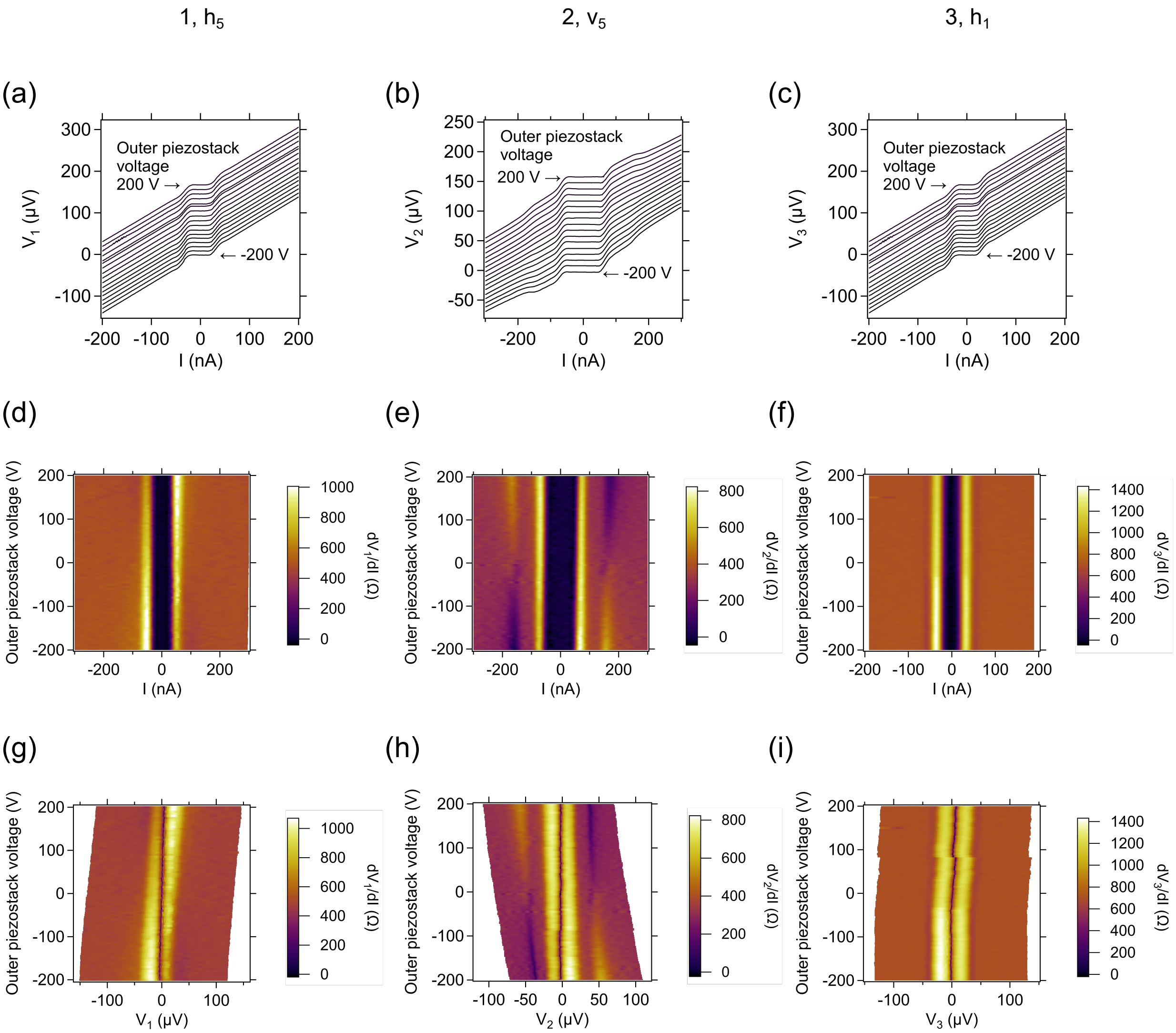

Figure 36: (a-c) Four-terminal characteristic I-V curves under different strain states, offseted in the vertical direction as determined by the corresponding outer piezo-stack voltage. (d-f) Four-terminal resistances as a function of I and the outer piezo-stack voltage. (g-i)Four-terminal resistances as a function of four-terminal voltage and the outer piezo-stack voltage. Figures in column 1, 2 and 3 correspond to device (1, h_5), (2, v_5), and (3, h_1) devices. Data for this set of figures is taken at zero magnetic field.

coherence peaks, as shown in Figure 36 (e,f) and Figure 37 (b). With compression, the secondary peak is on the positive current side, while the valley is on the negative current

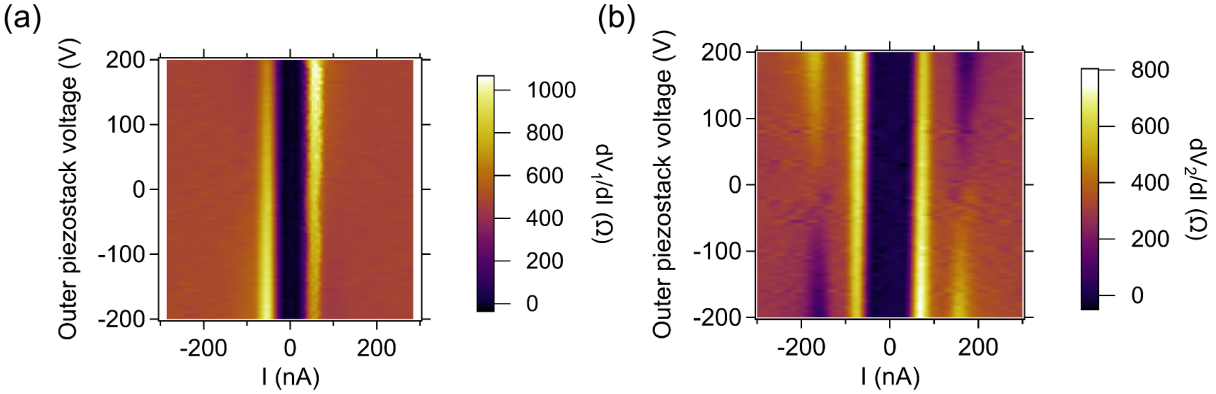

Figure 37: Four-terminal resistance as a function of I and outer piezo-stack voltage for device (1, h_5) (a) and device (2, v_5) (b). Data for this set of data is taken at zero magnetic field.

side. With tension, the positions of the secondary peak and the valley are switched.

(C) Effects of stress on the transport properties are not as strong in device (3, h_1) as in (1, h_5) and (2, v_5). However, from the shift of four-terminal voltage V_3 to more positive values under tension in Figure 36 (i), and the lack of signs for secondary peaks or valleys in Figure 36 (f,i), it can be deduced that device (3, h_1) behaves more similar to device (1, h_5) under strain. It is worth noting that the two devices with nanowires aligned in the same direction behave similarly.

(D) In all three devices, there is no distinguishable change in the critical current, which is the value of the current at which the device passes from superconducting (zero four-terminal resistance) into the normal, non-superconducting state (non-zero four-terminal resistance).

(E) Strain shifts the four-terminal voltages gradually in Figure 36 (g-i). The left and right edges of, the locations of coherence peaks, and the location of the superconducting region in the four-terminal voltage vs resistance curves are all shifted by strain, but at different speeds. Specifically, the edges in Figure 36 (g-i) represents the minimum and maximum value in four-terminal voltages at each outer piezo-stack voltage. In figures (g), at each outer piezo-stack voltage, the minimum (maximum) value of V_1 correspond to the four-terminal voltages when

I = -320 nA (+320 nA). In figure (h, i), the minimum (maximum) values of V_2 and V_3 corresponds to I = -300 nA (+300 nA), and I = -200 nA (+200 nA) respectively.

(F) Changes in current and four-terminal resistance with regards to strain are smooth, with no sign for an abrupt change or shift (Figure 36 (d-f), Figure 37 (a-b)).

(G) An abrupt change in four-terminal voltage at outer piezo stack voltage = 85 V is shown in Figure 36 (i), although all other figures show a smooth change with strain.

Next, we add the out-of-plane magnetic field (B) to investigate the effects of external uniaxial stress on transport properties in superconducting and non-superconducting states. In general, the magnetic field disrupts the precisely coordinated motion of the electron pairs and in turn, suppresses superconductivity. For the three devices of nanowire devices with zero strain, the critical magnetic field, which is the maximum value of magnetic field that can sustain superconductivity in the devices, is estimated to be $\sim$ 60 mT.

When the magnetic field is set to be 50 mT, 100 mT, 150 mT, we measure the four-terminal resistance as a function of current and outer piezo-stack voltage. The results for device (1, h_5) and (2, v_5) are shown in Figure 38.

Here, we take a close look at magnetic field with magnitude 100 mT and 150 mT, which are both above the critical magnetic field. A shallow gap near zero current can still be seen in four-terminal resistance dV_1/dI, dV_2/dI vs I curves, but the in-gap resistances are non-zero. The location of the gap is shifted by strain, and this shift becomes more obvious for higher magnetic fields. At zero strain (outer piezo-stack voltage = 0 V), there isn't any sign for coherence peaks. However, strain induces a peak on one side of the shallow gap in device (1, h_5), while creating a peak and a valley on each side of the shallow gap in device (2, v_5). These effect are consistent with the observations in Figure 36 and 37, at zero field. It is intriguing that these strain-induced novel peaks or valleys can survive much higher magnetic fields than coherence peaks that originally exist in unstrained devices.

We plot the strain sweep data at B = 50 mT, 100 mT, 150 mT (the same data set for Figure 39) in another way, as intensity graphs of four-terminal resistance as a function of four-terminal voltage and outer piezo-stack voltage for each device. The results for device (1, h_5) and (2, v_5) are shown in Figure 39. The majority of times, transport properties change smoothly with the slowly varying strain. However, in Figure 39 (a) (f), abrupt changes in

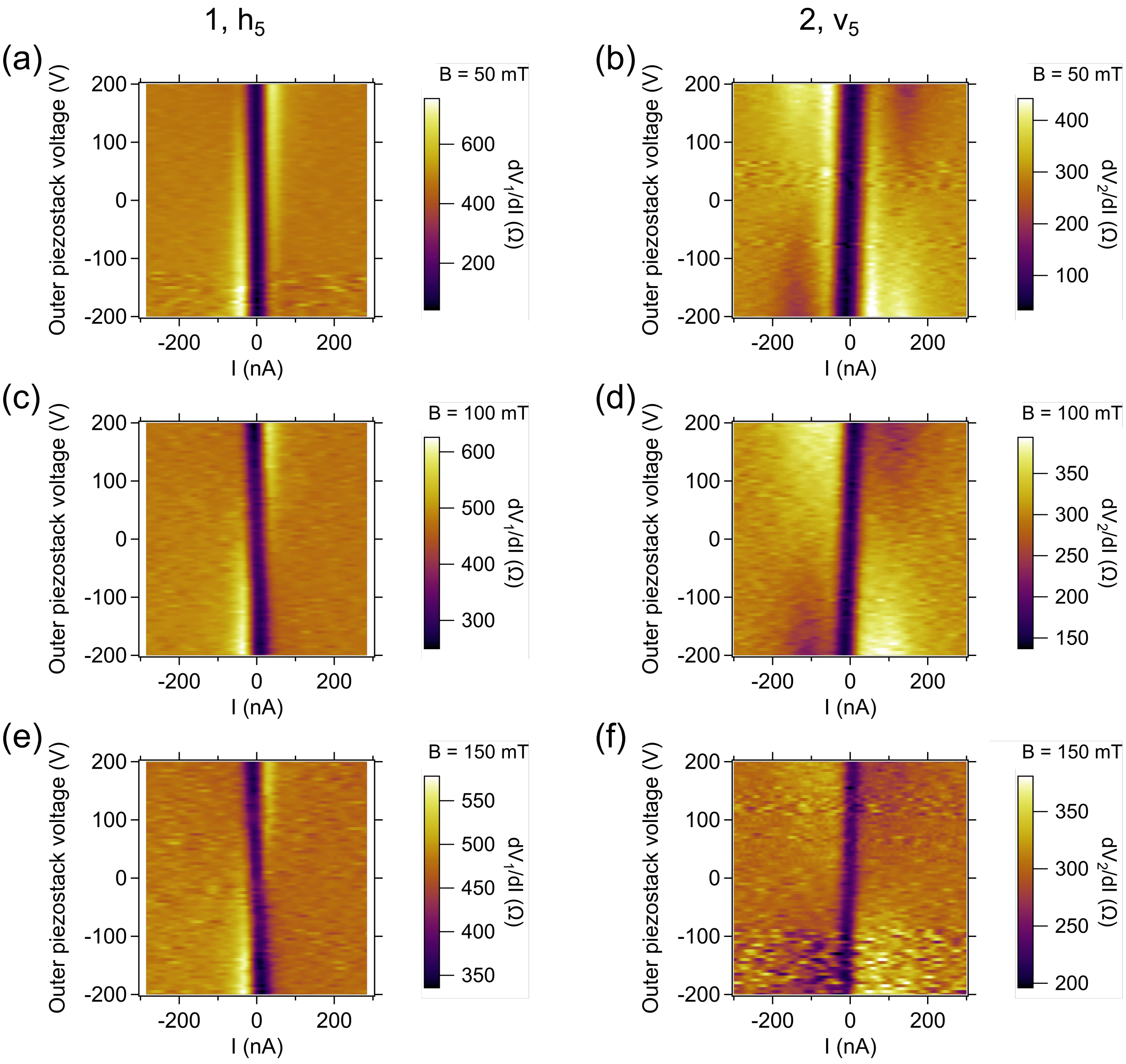

Figure 38: Four-terminal resistances as a function of I and outer piezo-stack voltage for device (1, h_5) (a,c,e) and device (2, v_5) (b,d,f), and with out-of-plane magnetic fields B = 50 mT (a,b), 100 mT (c,d), and 150 mT (e,f).

four terminal voltages caused by strain again occur under compression (outer piezo-stack = -120 V, -90 V). In Figure 39 (b,c), several dash lines are inserted to mark the features: the data points at the edge, which correspond to when I = -300 nA (black, for convenience,

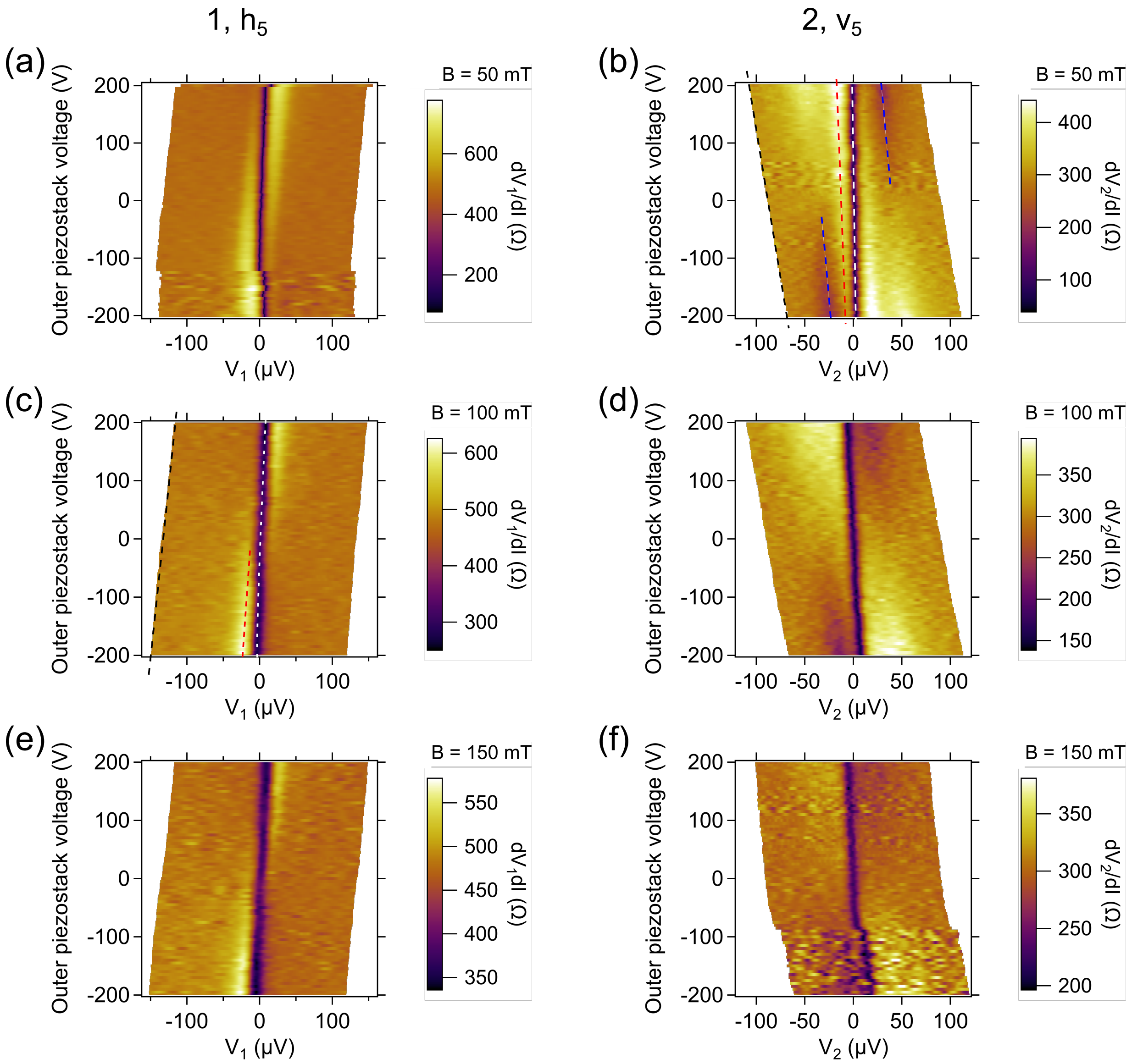

Figure 39: Four-terminal resistances as a function of four-terminal voltage and outer piezo-stack voltage for (1, h_5) (a,c,e) and (2, v_5) (b,d,f) devices, and with magnetic fields B = 50 mT (a,b), 100 mT (c,d), and 150 mT (e,f). Black, white, and red dash lines mark the shift in the edge, the superconducting state location, and the coherence peak location of four-terminal voltage with regards to the outer piezo-stack voltage respectively. Blue dash lines mark the location of secondary coherence peak and are only present in (2, v_5).

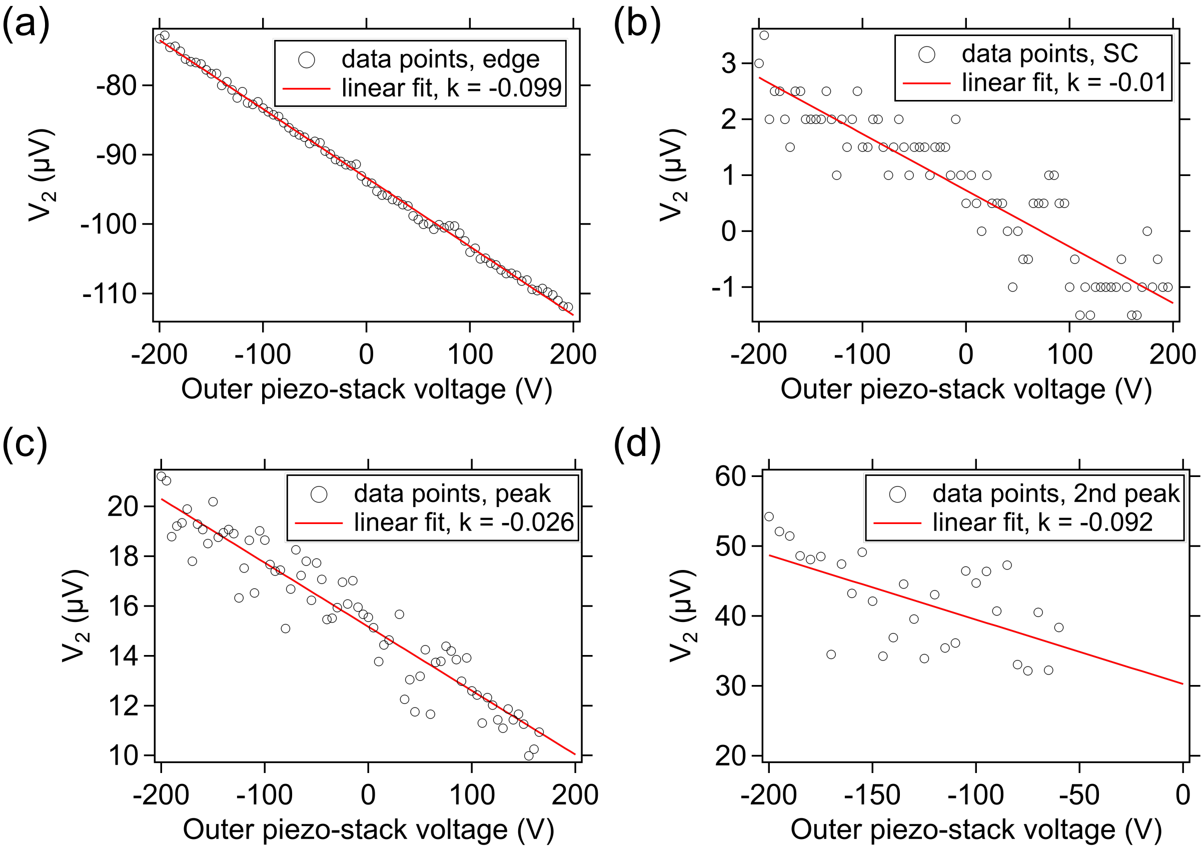

Figure 40: (a-d) For (2, v_5) at B = 50 mT, data points corresponding to the features marked in dashed lines in intensity graph Figure 39 (b): the left edge ((a), blue dashed line), the superconducting gap ((b), white dashed line), the left coherence peak ((c), red dashed line) and the strain-induced secondary peak ((d), blue dashed line) are plotted with circular markers. In each graph, a line of best fit is plotted with a red line, with its slopes k labeled at the top right corner.

referred to in short as "edge"); the locations of the center of the gaps, which correspond to the minimum value for dV_2/dI at each strain state (white, referred to later as "SC"); the locations of the coherence peaks on the negative V_2 side (red, referred to later as "peak"); the locations of the strain-induced secondary peaks on the negative V_2 side (blue, referred to later as "2nd peak"). From the intensity graphs, the shifts of those features seem to be linear with the outer piezo-stack voltage, since straight dash lines can trace those features

Table 5: Slopes for strain-induced shift in gap and peak features for three devices.

B (mT)	0	50	100	150	200
(1, h_5), edge	0.084	0.087	0.088	0.091	0.545
(1, h_5), SC	0.024	0.030	0.033	0.036	0.048
(1, h_5), peak	0.036	0.036	0.044	NA	NA
(2, v_5), edge	-0.098	-0.096	-0.103	-0.119	-0.040
(2, v_5), SC	0.017	-0.010	-0.032	-0.063	NA
(2, v_5), peak	0.007	-0.026	NA	NA	NA
(2, v_5), 2nd peak	-0.050	-0.083	NA	NA	NA
(3, h_1) , edge	0.056				
(3, h_1) , SC	0.046				
(3, h_1) , peak	0.047				

quite well. We attempt to calculate the slope of dashed lines.

For device (2, v_5), at B = 50 mT, at each outer piezo-stack voltage, we select the V_2 values that satisfy the above criteria and plot them as a function of the outer piezo-stack voltage, as shown in Figure 40. Then, linear fit using regression is conducted on the data points in Figure 40 to extract the slopes (referred to as k), which is indicative of how fast the above features are shifted by strain.

Besides device (2, v_5), we do the same analysis for the other two devices as well, at multiple magnetic fields. Table 5 shows the results. It is worth noting that the secondary peak feature is only present in device (2, v_5). Also, at higher magnetic fields, in dV/dI vs I curves, the gap feature gradually disappear, and the peak features get lower and broader. This makes it difficult for us to precisely determine the location of these features. This is also the reason why in Figure 40 (d), data points appear more scattered. In the case when k cannot be calculated from data using the above analysis, NA is used in table 5. Empty cells in table 5 indicates that data is not available.

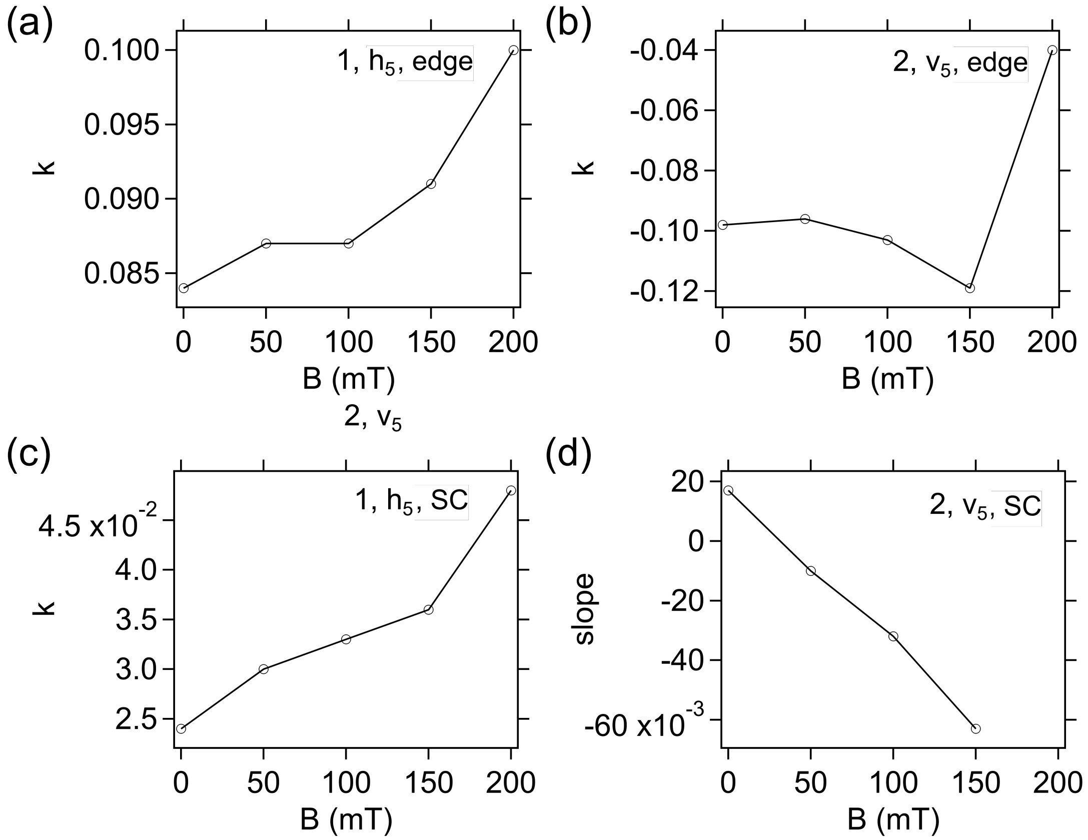

Figure 41: (a-d)k for the strain-induced shift in the “edge” (a,b) and the “SC” (a,b) features in device (1, h_5) (a,c) and device (2, v_5) (a,c), as a function of magnetic field. All k are determined using the linear-fit method shown in Figure 40.

In Figure 41, the slopes for the “edge” and “SC” features for device (1, h_5) and (2, v_5) are plotted as a function of the magnetic field. Application of the out-of-plane magnetic field increases the absolute values for the k in Figure 41 (a-d), except for device (2, v_5) at B = 200 mT, which is clearly an out-liner. It can also be deduced that of the two features, the field has a bigger influence on shifting the “SC” feature. Comparing B = 0 T and B = 200 mT, k for the “edge” feature in device (1, h_5) increases 19%, while k for the “SC” feature in the same device increased 100%.

Next, we show the results for lock-in measurements of four-terminal resistances of three nanowire devices with both uniaxial strain and temperature as variables. Four-terminal

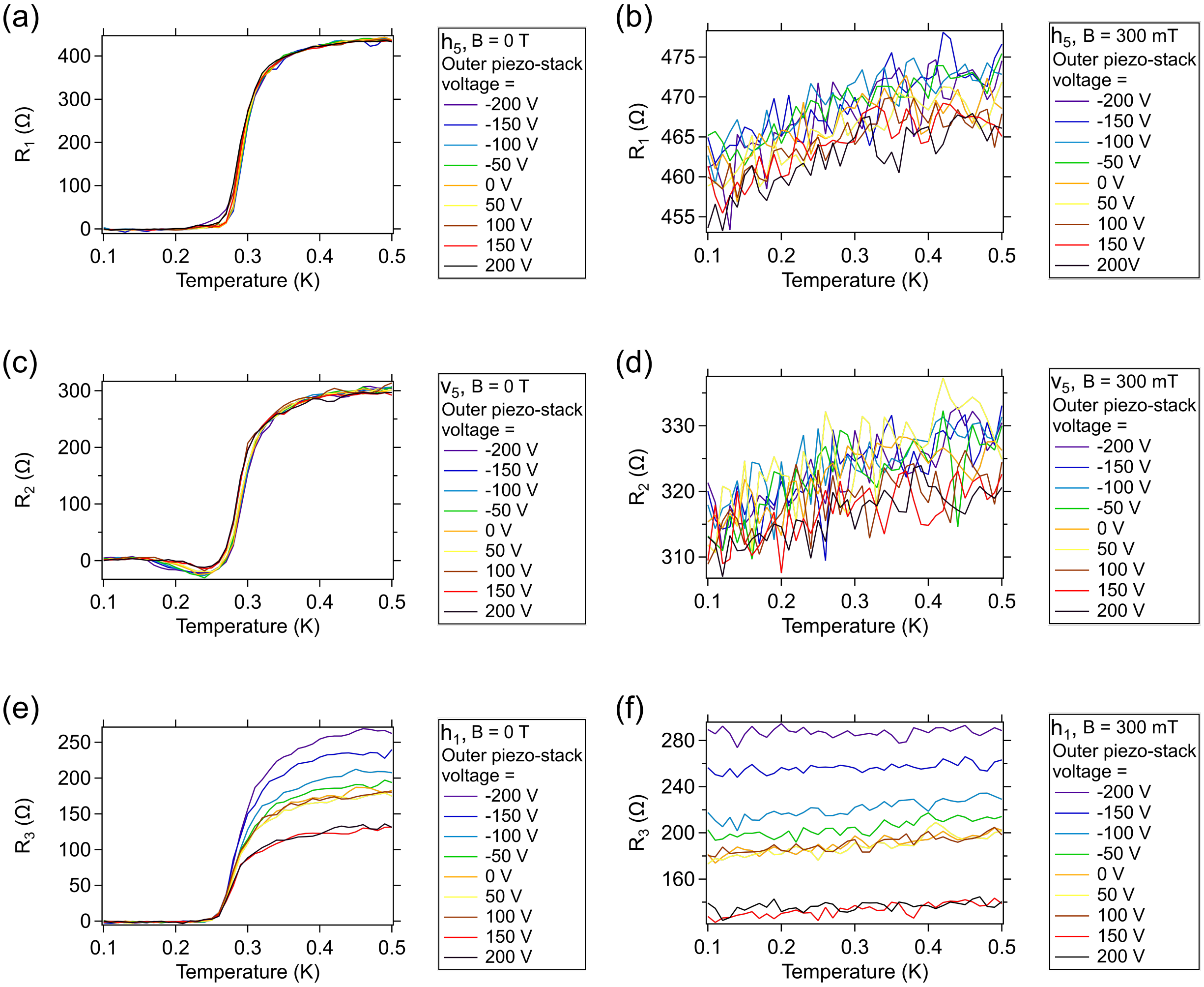

Figure 42: (a-f) Four-terminal resistances vs temperature for (1, h_5) (a,b), (2, v_5) (c,d), (3, h_1) (e,f) under multiple outer piezo-stack voltages. (a,c,e) show that superconducting phase transitions occur at $T_c \sim 300$ mK at zero magnetic field. (b,d,f) show the results when an out-of-plane magnetic field of magnitude 300 mT is applied.

devices containing the nanowire devices are driven differentially with two voltage sources V_s and $-V_s$ applied to two leads. We use $V_s = V_{ac}\sin(2\pi ft) + V_{dc}$, with $V_{ac} = 100\mu V$, $f = 13$ Hz and $V_{dc} = 200$ μV. If V_s only contains the ac component, due to instrumental offsets from the voltage sources and voltage drop on wires, electrodes and leads, the chemical potential on the nanowire device is, in fact, non-zero. This unintended chemical potential on nanowires may lead to misleading results. Therefore, a dc component V_{dc} is employed to the ensure the actual chemical potential on the nanowire device is close to zero.Current and four-terminal voltage signals are processed using a virtual lock-in algorithm to extract their amplitudes in phase with the voltage sources. Then, dividing the four-terminal voltage by the current, four-terminal resistances R_1 (for devices (1, h_5)), R_2 (for device (2, v_5)) and R_3 (for device (3, h_1)) are calculated. R_1, R_2 and R_3 as a function of temperature at multiple strain states (outer piezo-stack voltage ranging from -200 V to 200 V) and with and without out-of-plane magnetic field (B = 50 mT) are shown in Figure 42.

At zero magnetic field, superconducting phase transitions occur at $T_c \sim 300$ mK for all three devices, as shown in Figure 42 (a,c,e). Moreover, four-terminal resistance vs temperature curves for devices (1, h_5) and (2, v_5) at different strain states, including maximum compression (-200 V) and maximum tension (200 V), have no distinguishable differences. For device (3, h_1) , strain separated four-terminal resistances above T_c, increasing R_3 for compression, and decreasing R_3 for tension. However, strain doesn't change T_c in device (3, h_1) either. With a magnetic field above the critical field (Figure 42 (b,d,f), throughout all temperature, the nanowires are in the normal conductive state. Under the circumstance, compression is found to increase four-terminal resistance, while tension decreases four-terminal resistance. This effect is consistent in all three devices, but to different extents.

4.3.2 Hysteretic responses to the strain

4.3.2.1 Sample B

Sample B is a piece of sample with dimensions 2.5 × 5 × 0.1 mm^3. The edge orientation of the sample known to be [100], verified using X-ray diffraction. We use square brackets to denote a pseudo-cubic crystallographic axis, e.g. [001]. The conductive devices considered here (Figure 43 (b)) consist of three devices in series (which are subsequently referred to as devices 1, 2, and 3): from the top, a single horizontal nanowire ("1, v_1"), aligned with $[001]_t$; to the middle, a device of five vertical nanowires spaced 200nm apart ("2, h_5"), perpendicular to [001]; and to the bottom, a device of five horizontal nanowires, spaced 200nm apart ("3, v_5"), aligned with [001]. All three devices have the same length L = 3 µm. Conductive rectangular regions separate the individual wire segments, allowing each to be monitored independently and simultaneously. The uniaxial strain is in the horizontal direction, as illustrated in Figure 43 (d), which is parallel with device 2 nanowires, and perpendicular to [001].

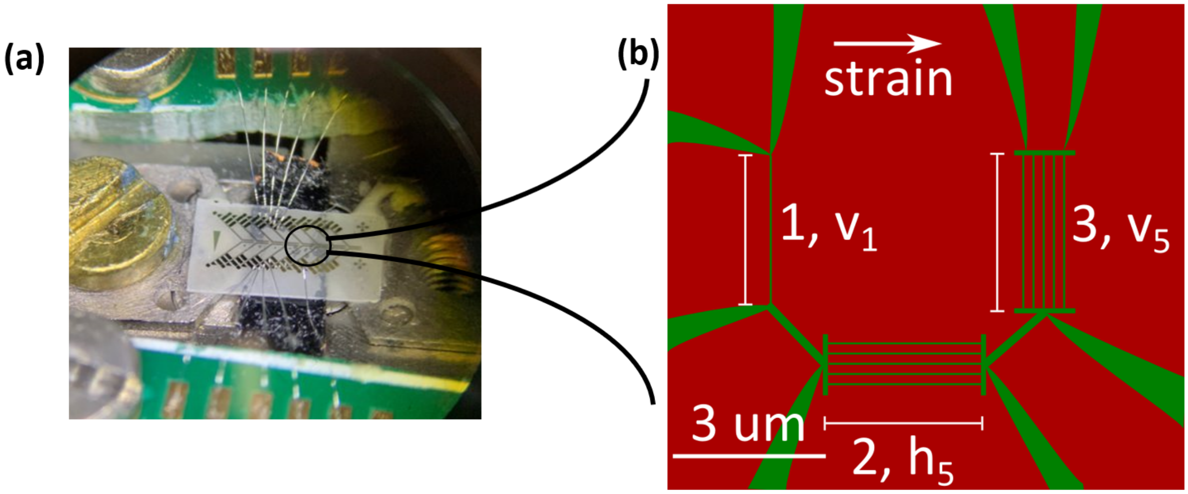

Figure 43: (a) A thin rectangular $LaAlO_3/SrTiO_3$ sample (at the center of the image, 2.5 × 5 × 0.1 mm^3 in size) is attached to washers with epoxy. Two washers are fastened to the strain cell with screws (one screw not shown in picture). (d) Device at the $LaAlO_3/SrTiO_3$ interface consists of three nanowire devices, in directions perpendicular to the uniaxial strain (1 wire, labeled 1, v_1), parallel to strain (5 wires, labeled 2, h_5), and perpendicular to strain (5 wires, labeled 3, v_5). All three devices have the same length, $L = 3\ \mu m$. Green areas depict conductive regions, while red areas are insulating.

With sample B, we drive the outer and the central piezo stacks simultaneously with differential voltages; if the outer piezo stack extends under a positive voltage, the central piezo stack shrinks under a negative voltage of the same magnitude, and vice versa. The combined effect is that when the voltage on the outer piezo stack is positive, the sample is under tensile stress, while a negative voltage on the outer piezo stack corresponds to compressive stress.

Comparing with the measurements performed on sample A, more piezo-stacks are used to apply stress to sample B and sample B is also half the size as sample A. By logic, the range of reachable global strain in sample B should be increased to be roughly four times the range in sample A. However, the local strain that nanowire devices are under is not the same as the global strain, and may not be four times larger than in sample A, since strain is distributed unevenly in $SrTiO_3$. The presence of ferroelastic domain in $SrTiO_3$ is known to cause local strain as large as 1% [21, 204, 205]. And there are also metal electrodes inserted into the sample that can induce local strain.

Four-terminal current-voltage (I-V) measurements for each of the three devices are recorded as a function of the outer piezo-stack voltage, and four-terminal resistances dV/dI are calculated using numerical differentiation, as shown in Figure 44. The vertical axis in intensity graphs is the outer piezo-stack voltage, used to indicate the type (tension or compression) and the magnitude of local strain qualitatively. Figure 44 (a) and (d) correspond to device (1, v_1) nanowire in Figure 43 (d), which contains one nanowire perpendicular to the uniaxial strain direction. Figure 44 (b) and (e) correspond to device (2, h_5) nanowires while Figure 44 (d) and (f) correspond to device (3, v_5) nanowires.

Figures in the top row (Figure 44 (a-c)) show the four-terminal transport measurement results when the strain is continuously swept from maximum tension to maximum compression, while figures in the bottom row (Figure 44 (d-f)) show the results when the stress is swept in the opposite direction. Compression-to-tension data used for the bottom row figures is taken right after tension-to-compression data used for the corresponding top row figures, with no additional change in piezo-stack voltages between the two data sets. For different directions of the stress sweeps, significant hysteresis in the responses to the external stress is observed.

Furthermore, there are several instances when the I-V characteristics abruptly change despite a smooth change in the external stress applied. For example, when outer piezo-stack voltage is -50 V, in Figure 44 (a-c), -100 V in Figure 44 (a), -160 V in Figure 44 (c), sudden shifts in the critical current and the locations for coherence peaks in the intensity graphs are observed. This feature is not observed in sample A.

We identify strain-induced quantum phase transitions from the superconducting state to the normal conductive state, shown as the sudden disappearance of the superconducting-gap feature I- $\mathrm{d}V_3/\mathrm{d}I$ in device (3, v_5) (Figure 44 (c)) at outer piezo-stack voltage = -160 V. At

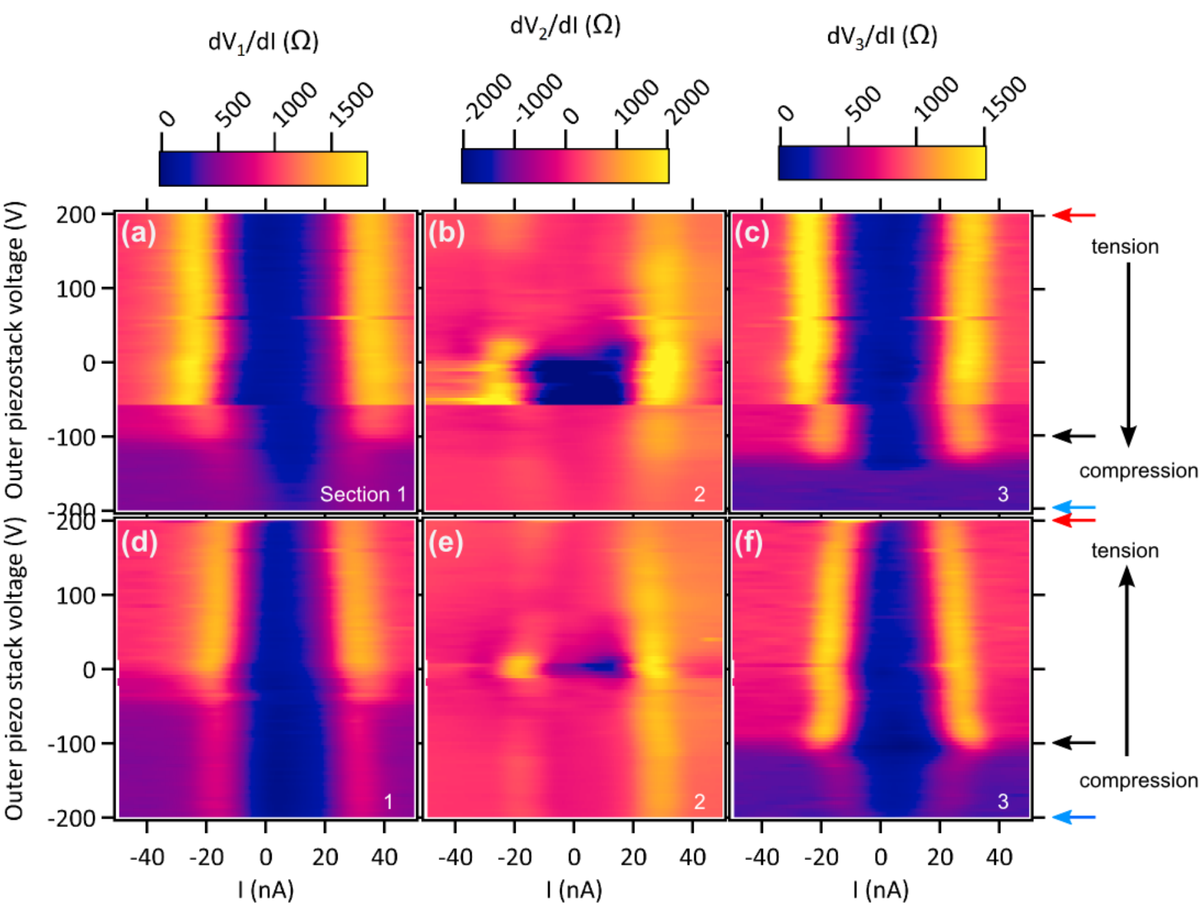

Figure 44: (a-f) Differential resistance, plotted as a function of current and outer piezo-stack voltage of the strain cell for three devices. Three columns of figures, from left to right, corresponds to devices (1, v_1), (2, h_5) and (3, v_5). The top row of figures correspond to when stress is swept from tension to compression, while the bottom row correspond to when stress is swept in the opposite direction.

that level of compression or more, four-terminal I-dV/dI curves for device (3, v_5) become relatively featureless, with four-terminal resistances being roughly 400 Ohm.

As the outer piezo-stack voltage increase from -200 V, superconducting gap features in four-terminal I-V curves are restored (Figure 44 (f)). Critical current I_c, increases as the outer piezo stack voltage increases from -200 V to -100 V, then reduces as outer piezo stack voltage increases from -100 V to 200 V. More prominent coherent peaks are also observed

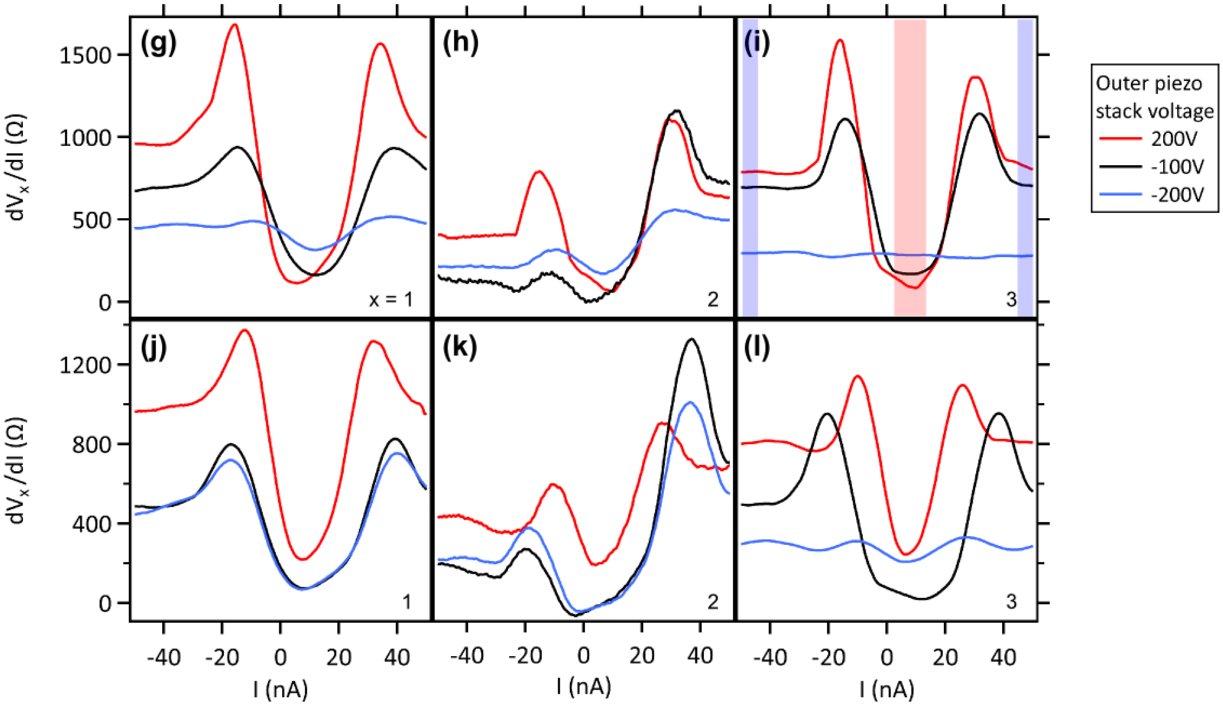

Figure 45: Part 2 of Figure 44 (g-i) Horizontal line-cuts of intensity graphs in Figure 44 (a-f) at outer piezo stack voltage = 200 V (red), -100 V (black), -200 V (blue). In (i), the red-shaded region is within superconducting gaps for curves with a gapped feature, including data points with the smallest 10% four-terminal resistance in those curves. The blue-shaded regions are outside of the gap and excludes the coherence peaks.

in the -100 V to -200 V range.

Comparing Figure 44 (a) with (c), (b) with (f), effects of uniaxial stress on transport properties of devices (1, v_1) and (3, v_5) are similar, and minor differences between the two devices can be attributed to the numbers of nanowires (one vs five) and differences in the local strain. However, the effects of strain on device (2, h_5) are different, indicating a strong correlation with the angle between the uniaxial strain axis and the nanowire direction.

In device (2, h_5), the strain induces negative four-terminal resistances during stress sweeps, when the outer piezo stack voltage is between 20 V and -50 V (Figure 44 (b,e)).

This may be due to non-local transport effects, similar to the anomaly reported in [206].

We describe the above phenomena by breaking four-terminal resistances down into two types: minimum resistances and normal state resistances. Minimum resistances are determined by averaging the lowest 10 % of four-terminal resistances for each I vs dV/dI curve. They indicate in-gap resistances for gap-shaped curves and are closely related to electron-pairing states, as shown in the red-shaded region near zero current in Figure 45 (i). Normal state resistances are calculated by averaging four-terminal resistances from 10 % of data points that are out of the gap in each I vs dV/dI curve, as shown in the purple-shaded regions at two ends of the curve in Figure 45 (i). They are considered for the connection to carrier densities or the conductive channel width in a normal conductive state. Figure 46 tracks them as a function of outer piezo stack voltages.

A number of observations can be made.

(A) For device (1, v_1), minimum resistances increase in the same direction with stress sweeps. For example, when the uniaxial strain sweep from tension to compression, they increase as the outer piezo stack voltage decrease from 200 V to -200 V. When the uniaxial strain change from compression to tension, they increase as outer piezo stack voltages increase from -200 V to 200 V.

(B) For device (3, v_5), the trend is the same as device (1, v_1) at positive outer piezo stack voltages, while a dip is observed at negative outer piezo stack voltages. Local minimum for the dip appear at outer piezo stack voltage = -160V or -100V, for different strain sweep directions, which are the same strain states when the quantum phase transitions appear. The coincident suggests that the dip is likely a sign of increased quantum fluctuations [207].

(C) For devices (1, v_1) and (3, v_5), normal state resistances both first increase when increasing outer piezo stack voltages from compression, then reach plateaus. Hysteresis can also be observed.

(D) For device (2, h_5), for both minimum resistances and normal state resistances, there were big dips in the middle, when uniaxial strain was small. Again, this anomaly is likely a reflection of the non-local effect in the system [206].

Comparing features at maximum compression in Figure 44 (a) and (d), (c) and (f), we notice that the dV/dI vs I characteristics are different, despited being measured at the

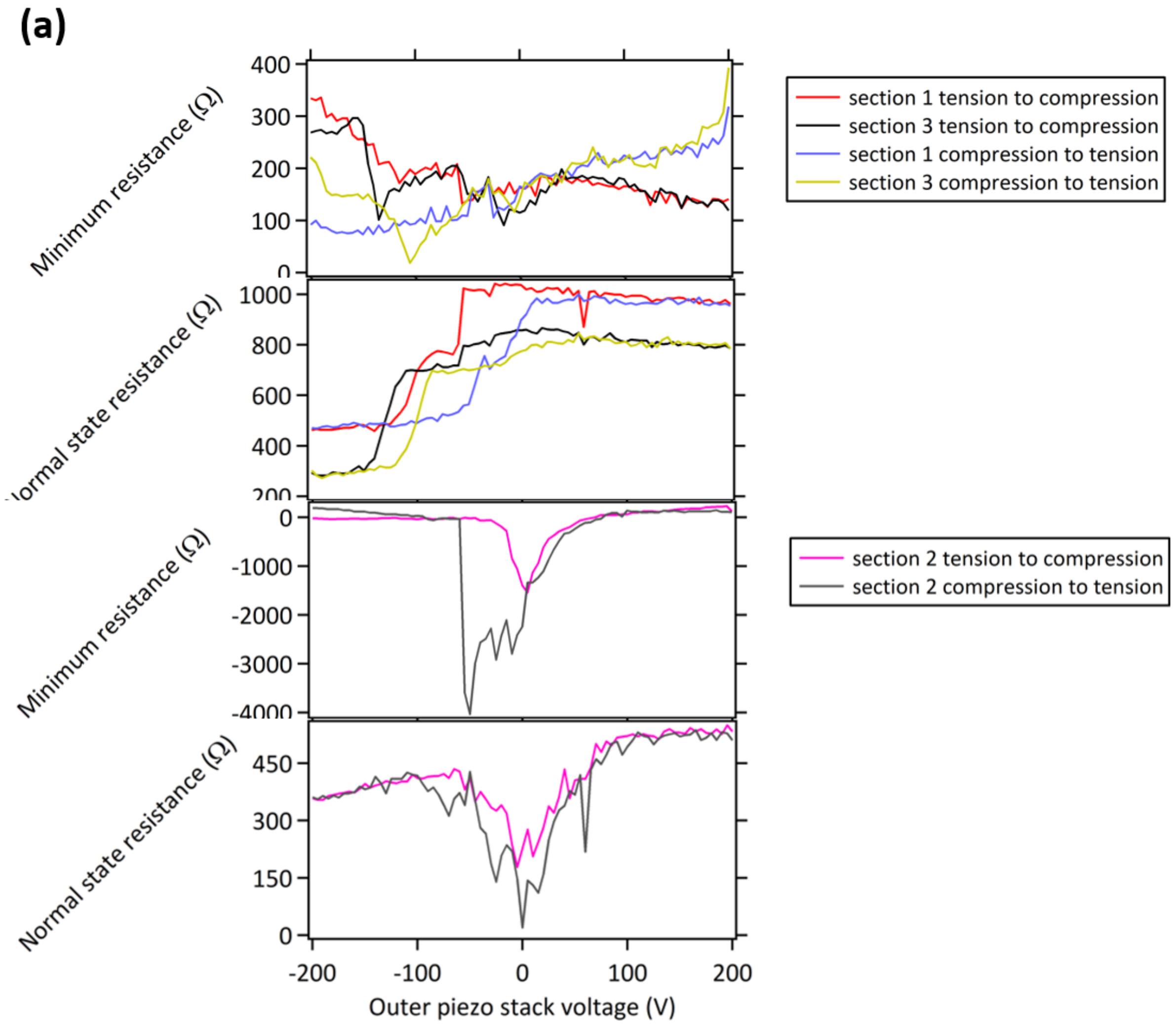

Figure 46: (a) From top to bottom, minimum resistances (in-gap, averaged from data points in the red-shaded region in Figure 45 (i)) for devices (1, v_1) and (3, v_5), normal state resistances (out-of-gap, averaged from data points in blue-shaded regions in Figure 45 (i)) for device (1, v_1) and (3, v_5) , minimum resistances for device (2, h_5), normal state resistances for device (2, h_5), plotted as a function of outer piezo stack voltages.

same value of outer piezo-stack voltage (-200 V). To get to the bottom of this, we plot the four-terminal I-V curves for device (1, v_1) (Figure 47 (b,d)) and (3, v_5) (Figure 47 (a,c)) respectively at outer piezo-stack voltage = -200 V, the last three curves at the end of the tension-to-compression sweep (Figure 47 (a,c)) and the first three curves at the start of the compression-to-tension sweep (Figure 47 (b,d)). Those curves are taken with a time separation of 30 minutes, and despite no change in piezo-stack voltages on the strain cell during this time period, local strain appears to have relaxed.

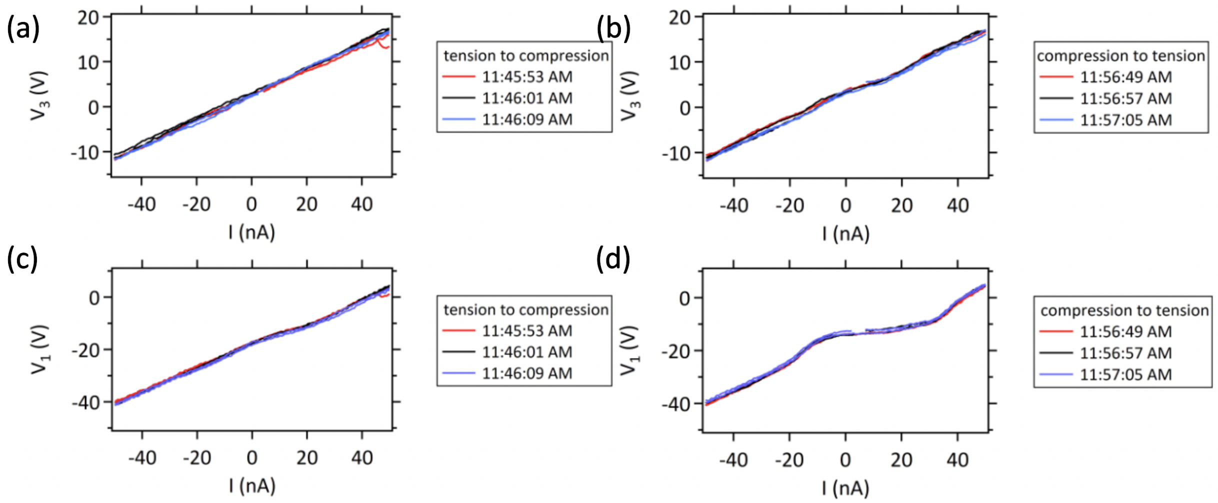

Figure 47: (a),(c) Four-terminal current vs voltage curves for device 3 and device 1 respectively at outer piezo stack voltage = -200 V, when strain changed from tension to compression.(b),(d) Four-terminal current vs voltage curves for device 3 and device 1 at the same outer piezo stack voltage, taken $\sim$ 30 minutes after (a),(c) with no change in outer piezo stack voltage in between.

At the same time that the stress sweeps take place for Figure 44, the temperature of the sample is monitored using a sensor located at the mixing chamber plate, as shown in Figure 48. The mixing chamber plate is designed to be in good thermal contact with the sample. Temperature sensor readings stay under 61 mK. The superconducting phase transition temperature T_c for the nanowire devices without any strain in sample B is measured to be $\sim$ 140 mK for all three devices. Therefore, we do not have any reason to think that the normal conductive state observed during stress sweeps (Figure 44-46) are caused by a higher temperature.

In Figure 48, minor increases in temperature when piezo-stack voltages are changing

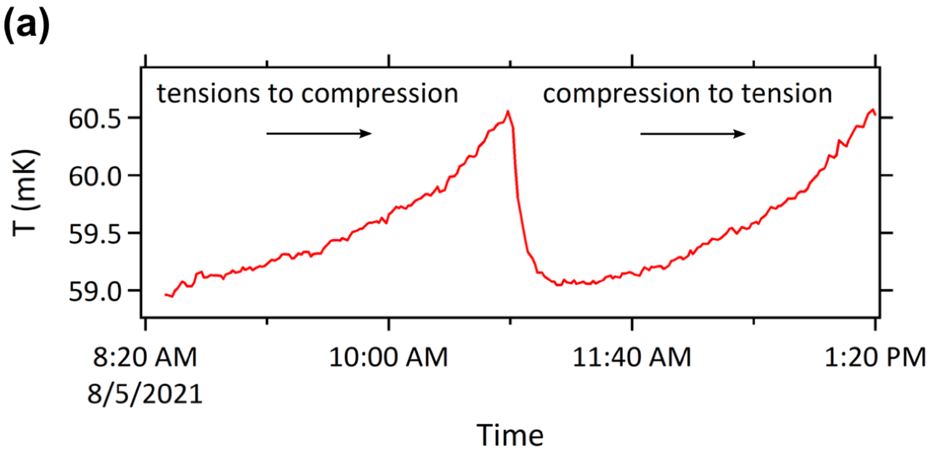

Figure 48: (a) Changes in the temperature at the mixing chamber plate of the dilution refrigerator, which is in excellent thermal contact with the sample, are minor, less than 2 mK during stress sweeps.

are observed. The increase in temperature can be explained as follows: when voltages on the piezo-stacks are changed, a current will run through the wires going to the strain cell, generating heat. But there will not be heat generated if the piezo-stack voltages stay the same, consistent with the observations. The quick drop in temperature at 10:50 AM corresponds to the end of a tension-to-compression sweep and afterwards voltages on both piezo-stacks remain unchanged (± 200 V) for approximately 30 minutes. During this period, no extra heat is generated, and the dilution refrigerator is able to cool down the strain cell back to the base temperature.

With the understanding of heating effects from the operation of the strain cell, we conduct the stress sweeps at a slow enough pace to leave sufficient time for heat generated from the strain cell to be removed by dilution cooling. Besides, the heating effects don't show much differences for the directions of the stress sweeps and should influence three devices in the same way. However, changes in transport properties are different for different nanowires devices and for different sweep directions (Figure 44-46). Therefore, heating as a cause for the observed strain-induced quantum phase transition can be excluded.

4.3.2.2 Sample C

In sample C (5 mm × 5 mm × 100 μm), similar experiments characterizing the effects of external uniaxial strain in superconductivity is performed on a single nanowire device (L = 3 μm, aligned parallel to the uniaxial strain direction). The experiment is done in another dilution refrigerator at 50 mK, using another strain cell of the same model. Again, we drive the outer and the central piezo stacks simultaneously with differential voltages. Position feedback data from the built-in capacitor is also collected using the calibration method described in Section 2.4.3, enabling us to correlated the four-terminal resistance (dV/dI) vs current curves with the global strain, as shown in Figure 49. The global strain is found to be extremely small, in the order of magnitude 1×10^{-4}.

A series observations can be made in sample C, bearing close resemblance to observations in sample B. When the uniaxial stress is continuously swept from compression to tension, a quantum phase transition from the superconducting state to a non-superconducting state is observed (Figure 49 (a)). Soon after the strain relaxed from the maximum compression, the superconducting gap feature in four-terminal resistance vs current curves is quickly restored (Figure 49 (b)). The responses to the stress are again found to be highly hysteretic relative to the direction of the stress sweeps and abrupt changes in dV/dI vs I characteristics occur several times (global strain = 0.006 % (Figure 49 (a)), -0.005 % (Figure 49 (b) etc.).

Additionally, in sample C, it is revealed that a sufficiently large tensile strain can also destroy superconductivity. In sample B, we are probably limited by the extent of the local strain reachable where those nanowires are located, so that this behaviour isn't observed.

4.4 Discussions

4.4.1 Piezoelectric effects

In sample A, strain-induced changes in four-terminal voltages (Figure 39-41) are observed and characterized by shifted locations of the superconducting gap and coherence peak features (Table 5). The piezoelectric effect opens up a new route for us to quantify the local

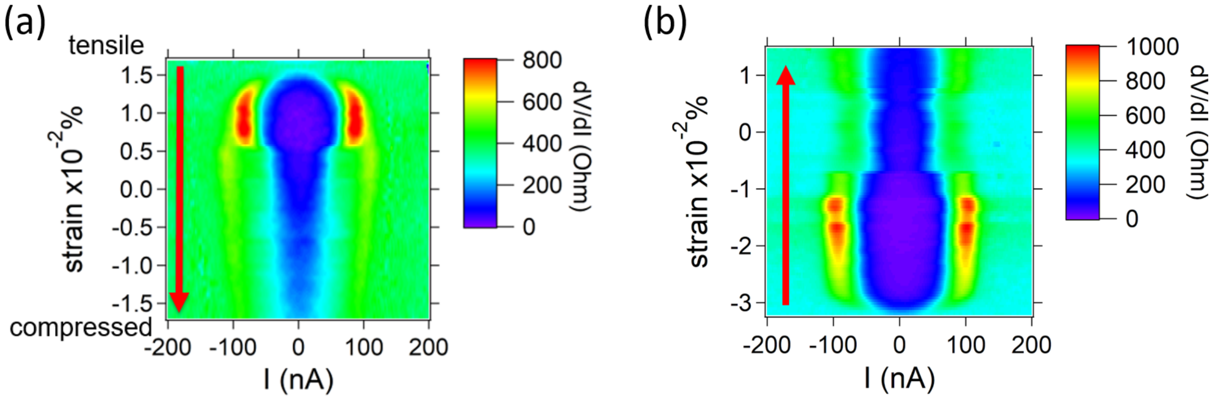

Figure 49: (a-b) Differential resistance (dV/dI), plotted as a function of the current and the global strain for a single nanowire aligned parallel to the uniaxial strain direction in sample B. (a) corresponds to when the stress is swept from tension to compression, while (b) corresponds to a compression-to-tension sweep.

strain at each nanowire device.

$SrTiO_3$ is a known to have a large piezoelectric response at cryogenic temperatures, as a result of the proximity to a ferroelectric quantum critical point and the existence of ferroelastic domains [205]. The coefficient of piezoelectricity is measured to be $d_{311} = 1.6 \times 10^{-9}$ m/V at T = 1.6 K. We multiply the slope for shifted superconducting gap location ("SC") in device (1, h_5) at zero magnetic field 0.024 μV/V (Table 5), by the maximum applied outer piezo-stack voltage 200 V, and derive the maximum change in voltage 4.8 μV. This voltage is the local strain induced piezo-voltage on the 3 μm-long nanowire device. Multiplying 4.8 μV by d_{311} gives us the displacement in the device 7.68×10^{-15} m. Finally, the displacement divided by the length of the device, gives us an estimation of the local strain 2.56×10^{-9}. The slopes for the "SC" feature for devices (2, v_5) and (3, h_1) at zero field are 0.017 μV/V and 0.046 μV/V respectively, suggesting variations in the local strains in the three nanowire devices, which are spaced roughly 10 μm apart on the same canvas.

The local strain on device (1, h_5) is significantly smaller than 0.03%, which is the global strain calculated and calibrated from position feedback data. A couple of things could contribute to this. The positive feedback is a measurement of the relative displacement of the piezo-stacks and contains the displacements from not just the sample, but also washers and epoxy. The epoxy used may be softer than the $SrTiO_3$-based sample and stretches a lot more than the sample. The inhomogeneity of local strain in the sample caused by ferroelastic domains is also a large factor. Moreover, canvases where devices are written on are surrounded by 10 metal electrical contacts, which can make local strain uneven in the canvas region (Figure 10 (a), Section 2.1).

The changes in the four-terminal voltages are not just related to the changes in transport properties of the nanowires, but also to changes in the resistances on the leads and electrodes. Moreover, it is challenging to provide explanations for other intriguing observations from Table 5: the slopes are larger for features that appear at a higher current (E.g. the locations of coherence peaks); the magnetic field increases the absolute values of the slopes. These observations are still open to interpretation for those with deep insights on the superconducting system.

The hypothesis that strain influences superconductivity in $SrTiO_3$ through the proximity to a quantum critical point has been used to explain previous strain-superconductivity experiment results in $SrTiO_3$ [10, 64, 13]. However, the hypothesis is at odds with our observations. Although piezoelectric effects prove the existence of a local strain, which should drive the system closer to or away from ferroelectric quantum criticality, no change in the superconducting phase transition temperature T_c is observed in the elastic regime.

4.4.2 Ferroelastic domains picture

In sample B and C, a strain-induced quantum phase transition is observed, in the non-hysteretic regime. Considering that local strain is minute, the suppression of superconductivity is indeed striking (Figure 44, 49). We also find that devices that have nanowires aligned in the same direction (devices (1, v_1) and (3, v_5) in Figure 44) demonstrate similar strain-induced behaviours, while devices containing nanowires aligned in different directions (devices (1, v_1) and (2, h_5) in Figure 44) demonstrate starkly different strain-induced behaviours. Small differences in the effects of stress in parallel wire devices (devices (1, v_1)

and (3, v_5)) can be contributed to the different numbers of nanowires contained (one vs five) and differences in the local strain.

Again, the ferroelectric quantum critical point hypothesis couldn't explain why the responses to external stress are dependent on the angle between the nanowires and the uniaxial stress direction (0° or 90°). Since the responses to stress is hysteretic and contain abrupt changes in the critical current and the heights of coherent peaks, it is natural to consider motions in local ferroelastic domains.

$SrTiO_3$ is known to harbour ferroelastic X, Y or Z domains, separated by nanometer-scale domain walls at temperatures below 105 K. Conductive regions created using c-AFM lithography are elongated in Z direction at room temperature [28], seeding ferroelastic Z domains at low temperatures. Insulating regions, by strain compensation, will form ferroelastic X or Y domains. Therefore, conductive channel edges coincide with ferroelastic domain walls. It has been demonstrated that superconductivity exists at these conductive channel edges, as shown in Figure 50 (a), and domain walls are believed to play an important role [17].

We build on the ferroelastic hypothesis and propose a simplified picture in which local strain moves the ferroelastic domain boundaries. In Figure 50 (b), when there is a sufficiently large compression perpendicular to the conductive channel, the ferroelastic Y domains as part of the insulating regions are likely to transition into ferroelastic Z domains, pushing the domain boundaries (yellow lines) outwards into the originally insulating regions. The green-color conductive channel is overdoped in the 2D bulk regions, while the red-color insulating regions are under-doped. The domain boundaries falling into the under-doped regions with reduced carrier density will lead to the suppression of superconductivity. This scenario corresponds to devices (1, v_1) and (3, v_5) in sample B, when uniaxial stress is perpendicular to the nanowires. And in those two devices, suppressed superconductivity under compression is indeed observed.

Also, in the picture illustrated by Figure 50 (b), the conductive channel width is expected to increase as compression gets larger. In the normal conductive state, assuming the carrier density remains unchanged, a wider channel will lead to a reduced resistance. This is consistent with the trend for the normal state resistance to decrease under compression for devices (1, v_1) and (3, v_5) (Figure 46).

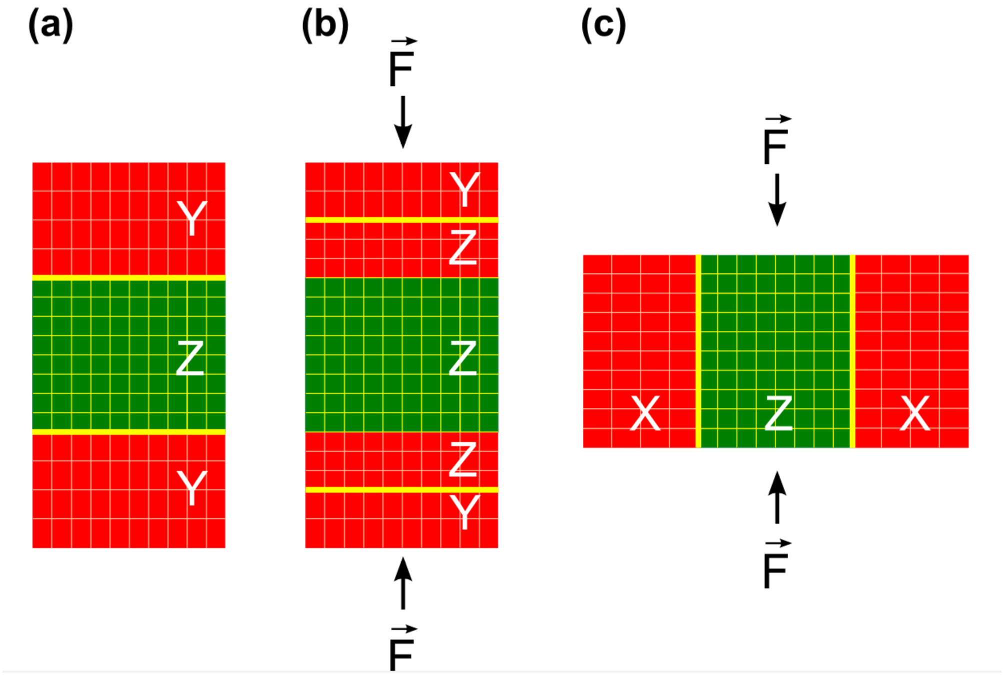

Figure 50: (a) Illustration of the expected ferroelastic domain structure associated with a green-color conductive region (filled with Z domains) surrounded by red-color insulating regions (filled with Y domains) at zero strain. Thick yellow lines mark domain boundaries that coincide with conducting region edges. (b) Illustration of a strain-induced phase transition turning some Y domains to Z domains, and the resulting displacement of domain boundaries to insulating regions. This scenario corresponds to devices (1, v_1) and (3, v_5) nanowires under strain in the perpendicular direction. (c) Illustration showing that the strain parallel to nanowire direction doesn't shift domain boundaries in the 2D assumption. This corresponds to device (2, h_5) nanowires under strain in the parallel direction.

In Figure 50 (c), the application of strain in the parallel direction with the nanowires doesn't induce ferroelastic phase transition in insulating regions, which are filled with ferroelastic X domains. Therefore, ferroelastic domain boundaries will not be moved. This picture corresponds to device (2, h_5) in sample B. Comparing Figure 50 (b) and (c), the effects of uniaxial stress on the ferroelastic domain boundaries in nanowires aligned in different directions are shown to be fundamentally different.

The simplified picture has its limitations. The 2D picture doesn't take into consideration that ferroelastic domains are 3D structures. When it comes to explaining hysteretic behaviours, the picture also doesn't offer deep insights beyond that the ferroelastic phase transition in the center of the picture is inherently hysteretic. Understanding the responses to uniaxial stress quantitatively calls for more advanced theoretical tools, such as the phase field simulation.

4.5 Summary

Oxide interfaces offer new ways to probe superconductivity in reduced spatial dimensions. The interface between $SrTiO_3$ and $LaAlO_3$, has a high-mobility 2D electron gas which can be superconducting at sub-Kelvin temperatures. We are able to create 1D conducting channels at the interface using c-AFM lithography [4]. Superconductivity in the system is associated with ferroelastic domain boundaries at the conductive region edges [17] and therefore is in the transition between 2D and 1D regimes. We investigate the effects of uniaxial stress on the superconductivity of nanowires in $LaAlO_3/SrTiO_3$. We find that superconductivity is strongly affected by uniaxial stress applied parallel to the nanowire direction and in the transverse direction. In the non-hysteretic regime, we observe that uniaxial stress modulates the heights and locations of coherence peaks and induces piezo-voltages. In the hysteretic regime, we find that minute changes in uniaxial stress can abruptly and reversibly switch $LaAlO_3/SrTiO_3$ nanowires from a superconducting state to a normal state. We discuss the implications of these results in the context of ferroelastic domain hypothesis.

5.0 Conclusions and Outlook

The stronitium titanate-based complex oxide heterostructure and nanostructures connect two well-established fields in condensed matter and material physics. On the one hand, there is correlated electron physic, which is often studied in bulk materials. Bulk $SrTiO_3$ has demonstrated a wide range of properties – superconductivity, ferromagnetism, and ferroic/multiferroic – that can be inherited by heterostructures [3]. On the other hand, there is semiconductor electronics, which allows for single electron control. In particular, the ability to control the metal-to-insulator transition at the $LaAlO_3/SrTiO_3$ interface using conductive atomic force microscopy (c-AFM) lithography has made it possible for the creation of nanoscale complex devices, making it an attractive platform for quantum information.

This dissertation seeks to deepen the understanding of superconductivity and electron-pairing for those oxide-based nanodevices. Six decades after the discovery of superconductivity in the unconventional superconductor $SrTiO_3$, the origin for superconductivity remains mysterious. Recent findings provide intriguing evidences for a intrinsic 1D nature of superconductivity in nanowires at the polar-nonpolar interface of $LaAlO_3/SrTiO_3$. In this dissertation, the effect of uniaxial strain on the superconductivity in those nanowires is investigated. Hysteretic and non-hysteretic moderations of superconductivity in quantum wires parallel to the strain direction and in transverse direction at cryogenic temperatures is achieved. Under certain strain conditions, minutes changes in uniaxial strain can abruptly and reversibly switch $LaAlO_3/SrTiO_3$ nanowires from a superconducting state to a normal state. That strain-induced phase transition is a hysteretical behaviour offers unique information in the complex interplay between strain and ferroelastic domains. In the non-hysteretic regime, the shifting of superconducting coherence peaks, a characteristics of electron-pairing, without changing superconducting transition temperature T_c is also demonstrated, suggesting that an alternative mechanism to the ferroelastic domain hypothesis could be in play.

The properties of unconventional superconductors are large shaped by competing phases. Chiefly among them is the pseudogap phase, where pre-formed Cooper pairs are believed to exist. In this dissertation, quasi-particle excitations in the pseudogap phase in $SmTiO_3$

/$SrTiO_3$/$SmTiO_3$ quantum well heterostructures are closely examined. By driving a portion of the device out of equilibrium with voltages or photons that exceed the pseudogap energy, mobile carriers generation is demonstrated. These results help to fill the knowledge gap in as well as introducing new approaches to studying the largely unknown pseudogap phase in oxide-based heterostructures.

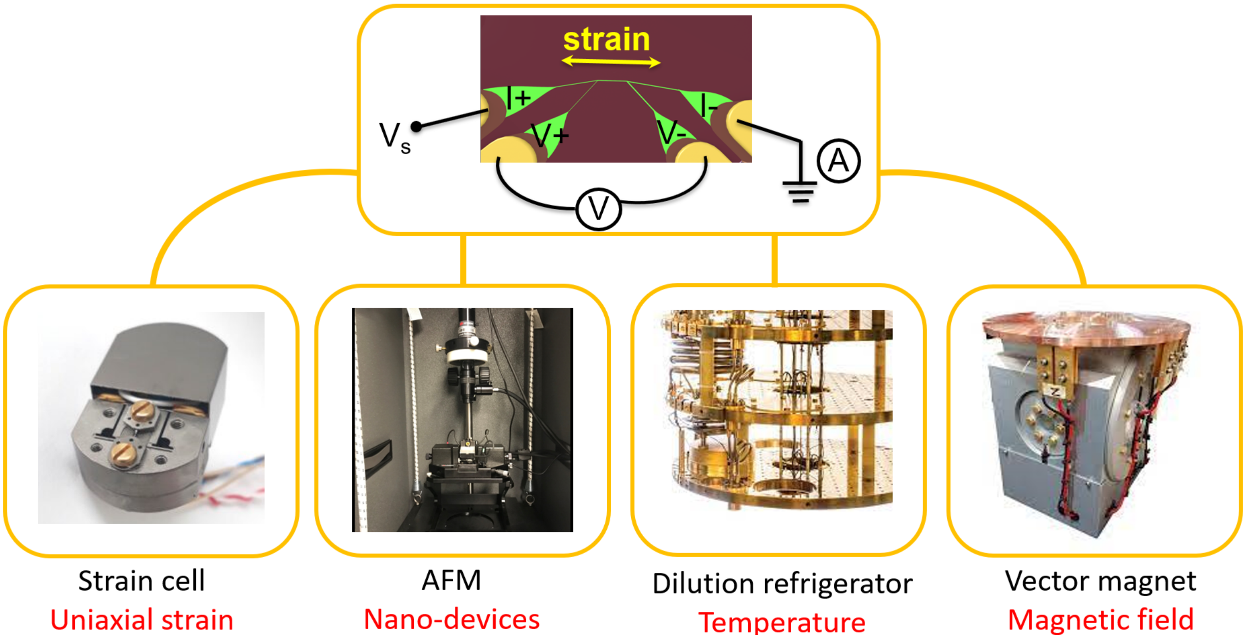

Strain cell
Uniaxial strain

AFM
Nano-devices

Dilution refrigerator
Temperature

Vector magnet
Magnetic field

Figure 51: Experiment setups for characterizing $LaAlO_3$/$SrTiO_3$ nanoscale devices. The properties of devices need be investigated with one or more of parameters: strain, device design, temperature, magnetic field and chemical potential etc., controllable by the instruments shown above.

There are many future follow up works to be done.

(1) Continuation on local probe characterization of mesoscale devices created at $LaAlO_3$ /$SrTiO_3$, using one or the combination of several variables: the amplitude of the strain, the angle between the strain and nanowires, temperature, in-plane and out-of-plane magnetic field, and chemical potential enabled by back gates or side gates.

(2) The design of nanowire devices can be enriched to include conductive square regions, waveguides, 1D zigzag nanowires, as the c-AFM lithography technique is mature enough for

these complex device designs to be executed with ease and the strain may produce more interesting results based on them. Especially, further exploration on 1D physics can greatly benefit from the electron waveguide. The c-AFM tip voltage or the shape of the electron waveguide can be modulated to access more electron transport properties, including the spin of electrons, which can lead to the realization of spintronics and Majorana Physics in the system.

(3) Phase-field modeling for $SrTiO_3$ can be employed as a power tool to simulate the formation of Ferroelastic domains. Besides the Ferroelastic domain hypothesis, alternative theories including Ferroelectricity and quantum critical point also need to be cross-examined with the experiment results to provide reasonable explanations for some of strain-related observations described in chapter 4.

(4) A variety of oxide-based heterostructures have been found to be superconducting, for example, the newly discovered $KTaO_3$ (KTO) interfaces [208, 209, 210, 211]. $KTaO_3$ shared many common features with $SrTiO_3$, yet $KTaO_3$ interfaces have an order of magnitude higher T_c than $LaAlO_3/SrTiO_3$ and behaves very differently. Utilizing the existing experimental setup, simply replacing the samples epoxied on top of the strain cell, characterizations of strain-transport properties for many thin film materials can be performed. The coordination of several instruments in the lab forms a extremely powerful and versatile platform, enabling numerous complex future researches that are only limited by our imagination.

Bibliography

[1] van Dirk and Peter Kes. The discovery of superconductivity. *Europhysics News*, 63, 01 2011.

[2] Wikipedia contributors. Superconductivity – wikipedia, the free encyclopedia, 2022. [Online; accessed 3-October-2022].

[3] Yun-Yi Pai, Anthony Tylan-Tyler, Patrick Irvin, and Jeremy Levy. Physics of srtio$_3$-based heterostructures and nanostructures: a review. *Reports on Progress in Physics*, 81(3):036503, feb 2018.

[4] Cheng Cen, Stefan Paetel, German Hammerl, C. Schneider, K Andersen, Carl Hellberg, Jochen Mannhart, and Jeremy Levy. Nanoscale control of an interfacial metal-insulator transition at room temperature. *Nature materials*, 7:298–302, 04 2008.

[5] Qijin Chen, Zhiqiang Wang, Rufus Boyack, Shuolong Yang, and K. Levin. When superconductivity crosses over: From bcs to bec, 2022.

[6] Hanjie Ding, Takayoshi Yokoya, Juan Carlos Campuzano, Toshiaki Takahashi, M. Randeria, M. Norman, T. Mochiku, Kazuo Kadowaki, and J. Giapintzakis. Spectroscopic evidence for a pseudogap in the normal state of underdoped high-T$_c$ superconductors. *Nature*, 382, 07 1996.

[7] Anthony Loeser, Zhen Shen, Dan Dessau, D. Marshall, C. Park, Patrick Fournier, and A Kapitulnik. $Bi_2Sr_2CaCu_2O_8 + \delta$. *Science (New York, N.Y.)*, 273:325–9, 08 1996.

[8] Ch. Renner, B. Revaz, J.-Y. Genoud, K. Kadowaki, and Ø. Fischer. Pseudogap precursor of the superconducting gap in under- and overdoped bi$_2$sr$_2$cacu$_2O_{8+\delta}$. *Phys. Rev. Lett.*, 80:149–152, Jan 1998.

[9] Patrick B. Marshall, Evgeny Mikheev, Santosh Raghavan, and Susanne Stemmer. Pseudogaps and emergence of coherence in two-dimensional electron liquids in $SrTiO_3$. *Phys. Rev. Lett.*, 117:046402, Jul 2016.

[10] Chloe Herrera, Jonah Cerbin, Amani Jayakody, Kirsty Dunnett, Alexander V. Balatsky, and Ilya Sochnikov. Strain-engineered interaction of quantum polar and superconducting phases. *Phys. Rev. Materials*, 3:124801, Dec 2019.

[11] E.R. Pfeiffer and J.F. Schooley. Superconducting transition temperatures of nb-doped $SrTiO_3$. *Physics Letters A*, 29(10):589–590, 1969.

[12] E.R. Pfeiffer and J.F. Schooley. Effect of stress on the superconducting transition temperature of $SrTiO_3$. *Journal of Low Temperature Physics*, 2(3-4):333–352, May 1970.

[13] Kaveh Ahadi, Luca Galletti, Yuntian Li, Salva Salmani Rezaie, Wangzhou Wu, and Susanne Stemmer. Enhancing superconductivity in $SrTiO_3$ films with strain. *Science Advances*, 5:eaaw0120, 04 2019.

[14] Ekhard Salje, Stuart Hayward, and William Lee. Ferroelastic phase transitions: Structure and microstructure. *Acta crystallographica. Section A, Foundations of crystallography*, 61:3–18, 02 2005.

[15] J Haeni, Patrick Irvin, W Chang, R Uecker, P Reiche, Y Li, Shak Choudhury, Wahyu Tian, M Hawley, B Craigo, A Tagantsev, X. Pan, S Streiffer, L Chen, S Kirchoefer, Jeremy Levy, and D Schlom. Room-temperature ferroelectricity in strained $SrTiO_3$. *Nature*, 430:758–61, 09 2004.

[16] N. Pertsev, AK Tagantsev, and N. Setter. Phase transitions and strain-induced ferroelectricity in $SrTiO_3$ epitaxial thin films. *Phys. Rev. B*, 61:R825–, 01 2000.

[17] Yun-Yi Pai, Hyungwoo Lee, Jung-Woo Lee, Anil Annadi, Guanglei Cheng, Shicheng Lu, Michelle Tomczyk, Mengchen Huang, Chang-Beom Eom, Patrick Irvin, and Jeremy Levy. One-dimensional nature of pairing and superconductivity at the $LaAlO_3/SrTiO_3$ interface. *Physical Review Letters*, 120, 07 2017.

[18] P. A. Fleury, J. F. Scott, and J. M. Worlock. Soft phonon modes and the 110° k phase transition in $SrTiO_3$. *Phys. Rev. Lett.*, 21:16–19, Jul 1968.

[19] K. A. Muller, W. Berlinger, and F. Waldner. Characteristic structural phase transition in perovskite-type compounds. *Phys. Rev. Lett.*, 21:814–817, Sep 1968.

[20] L. Rimai and G. A. deMars. Electron paramagnetic resonance of trivalent gadolinium ions in strontium and barium titanates. *Phys. Rev.*, 127:702–710, Aug 1962.

[21] Andy Buckley, Jean-Pierre Rivera, and Ekhard Salje. Twin structures in tetragonal $SrTiO_3$: The ferroelastic phase transition and the formation of needle domains. *Journal of Applied Physics*, 86:1653–1656, 08 1999.

[22] R. A. Cowley. Lattice dynamics and phase transitions of strontium titanate. *Phys. Rev.*, 134:A981–A997, May 1964.

[23] K. A. Muller and H. Burkard. $SrTiO_3$: An intrinsic quantum paraelectric below 4 k. *Phys. Rev. B*, 19:3593–3602, Apr 1979.

[24] S Rowley, Leszek Spalek, Robert Smith, M. Dean, Mitsuru Itoh, J Scott, G Lonzarich, and Siddharth Saxena. Ferroelectric quantum criticality. 04 2014.

[25] Yun-Yi Pai. Superconductivity of strontium titanate in reduced dimensions. June 2020.

[26] R.J.D. Tilley. Perovskites: Structure-property relationships. pages 1–315, 03 2016.

[27] J Scott, Ekhard Salje, and M Carpenter. Domain wall damping and elastic softening in $SrTiO_3$: Evidence for polar twin walls. *Physical review letters*, 109:187601, 11 2012.

[28] Maayan Honig, Joseph Sulpizio, Jonathan Drori, Arjun Joshua, E Zeldov, and Shahal Ilani. Local electrostatic imaging of striped domain order in $LaAlO_3/SrTiO_3$. *Nature materials*, 12, 11 2013.

[29] Yiftach Frenkel, Noam Haham, Yishai Shperber, Christopher Bell, Yanwu Xie, Zhuoyu Chen, Yasuyuki Hikita, Harold Hwang, and Beena Kalisky. Anisotropic transport at the $LaAlO_3/SrTiO_3$ interface explained by microscopic imaging of channel-flow over srtio 3 domains. *ACS Applied Materials & Interfaces*, 8, 04 2016.

[30] Hilary Noad, Eric Spanton, Katja Nowack, Hisashi Inoue, Minu Kim, Tyler Merz, Christopher Bell, Yasuyuki Hikita, Ruqing Xu, Wenjun Liu, Arturas Vailionis, Harold Hwang, and Kathryn Moler. Enhanced superconducting transition temperature due to tetragonal domains in two-dimensionally doped $SrTiO_3$. *Physical Review B*, 94, 05 2016.

[31] Z. Erlich, Yiftach Frenkel, Jonathan Drori, Y. Shperber, C. Bell, H. Sato, M. Hosoda, Yanwu Xie, Yasuyuki Hikita, H. Hwang, and Beena Kalisky. Optical study of tetragonal domains in $LaAlO_3/SrTiO_3$. *Journal of Superconductivity and Novel Magnetism*, 28, 03 2014.

[32] H.J Ma, S. Scharinger, Shengwei Zeng, D. Kohlberger, M. Lange, A. Stohr, Xiao Renshaw Wang, T. Venkatesan, R. Kleiner, J.F Scott, J M D Coey, Dieter Koelle, and A. Ariando. Local electrical imaging of tetragonal domains and field-induced ferroelectric twin walls in conducting $SrTiO_3$. *Physical Review Letters*, 116, 06 2016.

[33] Amel Hachemi, H. Hachemi, Abdelhak Ferhat, and Layachi Louail. Elasticity of $SrTiO_3$ perovskite under high pressure in cubic, tetragonal and orthorhombic phases. *Physica Scripta - PHYS SCR*, 82, 08 2010.

[34] Bin Okai and Jiichiro Yoshimoto. Pressure dependence of the structural phase transition temperature in $SrTiO_3$ and $KMnF_3$. *Journal of The Physical Society of Japan - J PHYS SOC JPN*, 39:162–165, 07 1975.

[35] J. F. Schooley, W. R. Hosler, and Marvin L. Cohen. Superconductivity in semiconducting $SrTiO_3$. *Phys. Rev. Lett.*, 12:474–475, Apr 1964.

[36] Zengwei Zhu, Benoit Fauque, and Kamran Behnia. Fermi surface of the most dilute superconductor. *Physical Review X*, 3, 11 2012.

[37] D. Eagles. Comment on two papers claiming records for the lowest carrier concentration at which superconductivity has been observed. 04 2016.

[38] Maria N. Gastiasoro, Jonathan Ruhman, and Rafael M. Fernandes. Superconductivity in dilute $SrTiO_3$: A review. *Annals of Physics*, 417:168107, 2020. Eliashberg theory

at 60: Strong-coupling superconductivity and beyond.

[39] Jutta Escher, J. Harke, Frank Dietrich, N. Scielzo, Ian Thompson, and Walid Younes. Reviews of modern physics. *Review of Modern Physics*, 84:353, 03 2012.

[40] Beena Kalisky, Eric Spanton, Hilary Noad, John Kirtley, Katja Nowack, Christopher Bell, Hiroki Sato, Masayuki Hosoda, Yanwu Xie, Yasuyuki Hikita, Carsten Woltmann, Georg Pfanzelt, Rainer Jany, Christoph Richter, Harold Hwang, Jochen Mannhart, and Kathryn Moler. Locally enhanced conductivity due to the tetragonal domain structure in $LaAlO_3/SrTiO_3$ heterointerfaces. *Nature materials*, 12, 09 2013.

[41] Xiao Lin, Zengwei Zhu, Benoît Fauqué, and Kamran Behnia. Fermi surface of the most dilute superconductor. *Phys. Rev. X*, 3:021002, Apr 2013.

[42] J. Hemberger, P. Lunkenheimer, R. Viana, R. Bohmer, and A. Loidl. Electric-field-dependent dielectric constant and nonlinear susceptibility in $SrTiO_3$. *Phys. Rev. B*, 52:13159–13162, Nov 1995.

[43] Hiromoto Uwe and Tunetaro Sakudo. Stress-induced ferroelectricity and soft phonon modes in $SrTiO_3$. *Phys. Rev. B*, 13:271–286, Jan 1976.

[44] W.J. Burke and R.J. Pressley. Stress induced ferroelectricity in $SrTiO_3$. *Solid State Communications*, 9(3):191–195, 1971.

[45] Darrell G. Schlom, Long-Qing Chen, Chang-Beom Eom, Karin M Rabe, Stephen K Streiffer, and Jean-Marc Triscone. Strain tuning of ferroelectric thin films. *Annual Review of Materials Research*, 37(1):589–626, 2007.

[46] T. Mitsui and W. B. Westphal. Dielectric and x-ray studies of $ca_xba_{1-x}Tio_3$ and $ca_xsr_{1-x}Tio_3$. *Phys. Rev.*, 124:1354–1359, Dec 1961.

[47] A. Stucky, G. Scheerer, Z. Ren, Didier Jaccard, jean-marie Poumirol, Celine Barreteau, E. Giannini, and D. Marel. Isotope effect in superconducting n-doped $SrTiO_3$. *Scientific Reports*, 6, 10 2016.

[48] V. V. Lemanov, E. P. Smirnova, P. P. Syrnikov, and E. A. Tarakanov. Phase transitions and glasslike behavior in $sr_{1-x}ba_xtio_3$. *Phys. Rev. B*, 54:3151–3157, Aug 1996.

[49] Jonathan M. Edge, Yaron Kedem, Ulrich Aschauer, Nicola A. Spaldin, and Alexander V. Balatsky. Quantum critical origin of the superconducting dome in $srtio_3$. *Phys. Rev. Lett.*, 115:247002, Dec 2015.

[50] V L Gurevich, A I Larkin, and Yu A Firsov. Possibility of superconductivity in semiconductors. *Sov. Phys. - Solid State (Engl. Transl.); (United States)*, 4, 7 1962.

[51] C. S. Koonce, Marvin L. Cohen, J. F. Schooley, W. R. Hosler, and E. R. Pfeiffer. Superconducting transition temperatures of semiconducting $srtio_3$. *Phys. Rev.*,

163:380–390, Nov 1967.

[52] Marvin L. Cohen. Superconductivity in many-valley semiconductors and in semimetals. *Phys. Rev.*, 134:A511–A521, Apr 1964.

[53] Sajna Hameed, Damjan Pelc, Zach Anderson, Avi Klein, R. J. Spieker, L. Yue, B. Das, J. Ramberger, M. Lukas, Y. Liu, M. J. Krogstad, R. Osborn, Y. Li, C. Leighton, Rafael M Fernandes, and M. Greven. Enhanced superconductivity and ferroelectric quantum criticality in plastically deformed strontium titanate. *Nature Materials*, 21(1):54–61, January 2022.

[54] Ryan Haislmaier, R. Engel-Herbert, and Venkatraman Gopalan. Stoichiometry as key to ferroelectricity in compressively strained srtio3 films. *Applied Physics Letters*, 109:032901, 07 2016.

[55] P. Wiecki, A.-A. Haghighirad, F. Weber, M. Merz, R. Heid, and A. E. Böhmer. Dominant in-plane symmetric elastoresistance in $CsFe_2As_2$. *Phys. Rev. Lett.*, 125:187001, Oct 2020.

[56] Paul Wiecki, Mehdi Frachet, Amir-Abbas Haghighirad, T. Wolf, C. Meingast, R. Heid, and A. Böhmer. Emerging symmetric strain response and weakening nematic fluctuations in strongly hole-doped iron-based superconductors. *Nature Communications*, 12, 08 2021.

[57] Saien Xie, Lijie Tu, Yimo Han, Lujie Huang, Kibum Kang, Ka Un Lao, Preeti Poddar, Chibeom Park, David A. Muller, Robert A. DiStasio, and Jiwoong Park. Coherent, atomically thin transition-metal dichalcogenide superlattices with engineered strain. *Science*, 359(6380):1131–1136, 2018.

[58] C. A. Perroni, V. Cataudella, G. De Filippis, G. Iadonisi, V. Marigliano Ramaglia, and F. Ventriglia. Modeling of strain effects in manganite films. *Phys. Rev. B*, 68:224424, Dec 2003.

[59] A Ohtomo and HY Hwang. A high-mobility electron gas at the $LaAlO_3/SrTiO_3$ heterointerface. *Nature*, 427(6973):423, 2004.

[60] Abhijit Biswas and Yoon Hee Jeong. Strain effect in epitaxial oxide heterostructures. chapter 1. IntechOpen, Rijeka, 2018.

[61] Darrell G Schlom, Long-Qing Chen, Craig J Fennie, Venkatraman Gopalan, David A Muller, Xiaoqing Pan, Ramamoorthy Ramesh, and Reinhard Uecker. Elastic strain engineering of ferroic oxides. *Mrs Bulletin*, 39(2):118–130, 2014.

[62] Chung Wung Bark, D Felker, Yong Wang, Ying Zhang, Ho Jang, Chad Folkman, J. W. Park, Seung-Hyub Baek, Hua Zhou, D Fong, X. Pan, Evgeny Tsymbal, M Rzchowski, and C. Eom. Tailoring a two-dimensional electron gas at the $LaAlO_3/SrTiO_3$ (001)

interface by epitaxial strain. *Proceedings of the National Academy of Sciences of the United States of America*, 108, 02 2011.

[63] Guo-zhen Liu, Qingyu Lei, Matt Wolak, Qun Li, L.-Q Chen, Christopher Winkler, Jennifer Sloppy, Mitra Taheri, and Xiaoxing Xi. Epitaxial strain and its relaxation at the $LaAlO_3/SrTiO_3$ interface. *Journal of Applied Physics*, 120, 08 2016.

[64] K. Dunnett, Awadhesh Narayan, N. A. Spaldin, and A. V. Balatsky. Strain and ferroelectric soft-mode induced superconductivity in strontium titanate. *Phys. Rev. B*, 97:144506, Apr 2018.

[65] S. E. Rowley, C. Enderlein, J. Ferreira de Oliveira, D. A. Tompsett, E. Baggio Saitovitch, S. S. Saxena, and G. G. Lonzarich. Superconductivity in the vicinity of a ferroelectric quantum phase transition, 2018.

[66] Hisashi Sato. Enhanced superconductivity by reducing magnetism in strained $la_{2x}sr_x cuo_4$ films. *Physica C: Superconductivity*, 468:2366–2368, 12 2008.

[67] Alessia Sambri, Mario Scuderi, Anita Guarino, Emiliano Di Gennaro, Ricci Erlandsen, Rasmus Dahm, Anders Bjørlig, Dennis Christensen, Roberto Capua, Bartolomeo Ventura, Umberto Scotti di Uccio, Salvo Mirabella, Giuseppe Nicotra, Corrado Spinella, Thomas Jespersen, and F. Granozio. Self-formed, conducting $LaAlO_3/SrTiO_3$ micro-membranes. *Advanced Functional Materials*, 30, 11 2020.

[68] Hongli Guo, Wissam A. Saidi, and Jin Zhao. Tunability of the two-dimensional electron gas at the $LaAlO_3/SrTiO_3$ interface by strain-induced ferroelectricity. *Phys. Chem. Chem. Phys.*, 18:28474–28484, 2016.

[69] I. Bozovic, G. Logvenov, I. Belca, B. Narimbetov, and I. Sveklo. Epitaxial strain and superconductivity in $la_{2-x}sr_x cuo_4$ thin films. *Phys. Rev. Lett.*, 89:107001, Aug 2002.

[70] Stefan Paetel, German Hammerl, Andreas Schmehl, C. Schneider, and Jochen Mannhart. Tunable quasi-two-dimensional electron gases in oxide heterostructures. *Science (New York, N.Y.)*, 313:1942–5, 10 2006.

[71] Nicolas Reyren, Stefan Paetel, Andrea Caviglia, L Kourkoutis, German Hammerl, Christoph Richter, C. Schneider, Thilo Kopp, A.-S Ruetschi, Didier Jaccard, M Gabay, DA Muller, J.-M Triscone, and Jochen Mannhart. Superconducting interfaces between insulating oxides. *Science (New York, N.Y.)*, 317:1196–9, 09 2007.

[72] AD Caviglia, Stefano Gariglio, Nicolas Reyren, Didier Jaccard, T Schneider, M Gabay, S Thiel, G Hammerl, Jochen Mannhart, and J-M Triscone. Electric field control of the $LaAlO_3/SrTiO_3$ interface ground state. *Nature*, 456(7222):624, 2008.

[73] Nicolas Reyren, S Thiel, AD Caviglia, L Fitting Kourkoutis, German Hammerl, Christoph Richter, CW Schneider, Thilo Kopp, A-S Ruetschi, Didier Jaccard, Marc

Gabay, David A Muller, J-M Triscone, and Jochen Mannhart. Superconducting interfaces between insulating oxides. *Science*, 317(5842):1196–1199, 2007.

[74] Andrea Caviglia, M Gabay, Stefano Gariglio, Nicolas Reyren, Claudia Cancellieri, and J.-M Triscone. Tunable rashba spin-orbit interaction at oxide interfaces. *Physical review letters*, 104:126803, 03 2010.

[75] Moshe Ben Shalom, M Sachs, David Rakhmilevitch, Alexander Palevski, and Yoram Dagan. Tuning spin-orbit coupling and superconductivity at the $LaAlO_3/SrTiO_3$ interface: A magnetotransport study. *Physical review letters*, 104:126802, 03 2010.

[76] A Brinkman, M Huijben, M Zalk, Jeroen Huijben, U. Zeitler, J. Maan, Wilfred Wiel, Guus Rijnders, Dave Blank, and Hans Hilgenkamp. Magnetic effects at the interface between non-magnetic oxides. *Nature materials*, 6:493–6, 08 2007.

[77] Chunhai Yin, Patrick Seiler, Lucas Tang, Inge Leermakers, Nikita Lebedev, Uli Zeitler, and J. Aarts. Tuning rashba spin-orbit coupling at $LaAlO_3/SrTiO_3$ interfaces by band filling. *Physical Review B*, 101, 06 2020.

[78] Mario Basletic, Jean-Luc Maurice, C Carrétéro, Gervasi Herranz, O Copie, Manuel Bibes, E Jacquet, K. Bouzehouane, S Fusil, and Agnes Barthelemy. Mapping the spatial distribution of charge carriers in $LaAlO_3/SrTiO_3$ heterostructures. *Nature materials*, 7:621–5, 07 2008.

[79] Naoyuki Nakagawa, Harold Y. Hwang, and David A. Muller. Why some interfaces cannot be sharp. *Nature Materials*, 5(3):204–209, March 2006.

[80] S.A. Chambers, M.H. Engelhard, V. Shutthanandan, Z. Zhu, T.C. Droubay, L. Qiao, P.V. Sushko, T. Feng, H.D. Lee, T. Gustafsson, E. Garfunkel, A.B. Shah, J.-M. Zuo, and Q.M. Ramasse. Instability, intermixing and electronic structure at the epitaxial $LaAlO_3/SrTiO_3(001)$ heterojunction. *Surface Science Reports*, 65(10):317–352, 2010.

[81] Alexey Kalabukhov, Robert Gunnarsson, Johan Borjesson, Eva Olsson, Tord Claeson, and Dag Winkler. Effect of oxygen vacancies in the $SrTiO_3$ substrate on the electrical properties of the $LaAlO_3/SrTiO_3$ interface. *Phys. Rev. B*, 75:121404, Mar 2007.

[82] Y.Z. Chen, D.V. Christensen, F. Trier, N. Pryds, A. Smith, and S. Linderoth. On the origin of metallic conductivity at the interface of $LaAlO_3/SrTiO_3$. *Applied Surface Science*, 258(23):9242–9245, 2012. EMRS 2011 Spring Symp J: Laser Materials Processing for Micro and Nano Applications.

[83] S. McKeown Walker, A. de la Torre, F. Y. Bruno, A. Tamai, T. K. Kim, M. Hoesch, M. Shi, M. S. Bahramy, P. D. C. King, and F. Baumberger. Control of a two-dimensional electron gas on $SrTiO_3(111)$ by atomic oxygen. *Phys. Rev. Lett.*, 113:177601, Oct 2014.

[84] Gervasi Herranz, Florencio Sanchez, Nico Dix, and Mateusz Scigaj. High mobility

conduction at (110) and (111) $LaAlO_3/SrTiO_3$ interfaces. *Scientific reports*, 2:758, 10 2012.

[85] Mark Huijben, Gertjan Koster, Michelle Kruize, Sander Wenderich, J. Verbeeck, S. Bals, E. Slooten, B. Shi, Hajo Molegraaf, J.E. Kleibeuker, S. van Aert, J.B. Goedkoop, Alexander Brinkman, David H.A. Blank, M.S. Golden, G. van Tendeloo, Johannes W.M. Hilgenkamp, and Augustinus J.H.M. Rijnders. Defect engineering in oxide heterostructures by enhanced oxygen surface exchange. *Advanced functional materials*, 23(42):5240–5248, 2013.

[86] Lu Chen, Jianan Li, Yuhe Tang, Yun-Yi Pai, Yunzhong Chen, Nini Pryds, Patrick Irvin, and Jeremy Levy. Extreme reconfigurable nanoelectronics at the $CaZrO_3/SrTiO_3$ interface. *Advanced Materials*, 30, 07 2018.

[87] Dengyu Yang, Shan Hao, Jun Chen, Qing Guo, Muqing Yu, Yang Hu, Kitae Eom, Jung-Woo Lee, Chang-Beom Eom, Patrick Irvin, and Jeremy Levy. Nanoscale control of $LaAlO_3/SrTiO_3$ metal-insulator transition using ultra-low-voltage electron-beam lithography. 08 2020.

[88] Joseph A. Sulpizio, Shahal Ilani, Patrick Irvin, and Jeremy Levy. Nanoscale phenomena in oxide heterostructures. *Annual Review of Materials Research*, 44(1):117–149, 2014.

[89] Thach Ngo, Jung-Won Chang, Kyujoon Lee, Seungju Han, Joon Sung Lee, Young Kim, Myung-Hwa Jung, Yong-Joo Doh, Mahn-Soo Choi, Jonghyun Song, and Jinhee Kim. Polarity-tunable magnetic tunnel junctions based on ferromagnetism at oxide heterointerfaces. *Nature communications*, 6:8035, 08 2015.

[90] Dennis Christensen, Yiftach Frenkel, Yunzhong Chen, Y. Xie, Z. Chen, Yasuyuki Hikita, A. Smith, Lior Klein, H. Hwang, Nini Pryds, and Beena Kalisky. Strain-tunable magnetism at oxide domain walls. *Nature Physics*, 15, 03 2019.

[91] R. Ohtsuka, Mikko Matvejeff, K. Nishio, Ryota Takahashi, and M. Lippmaa. Transport properties of $LaAlO_3/SrTiO_3$ heterostructures. *Applied Physics Letters*, 96:192111–192111, 05 2010.

[92] M. Huijben, D. Kockmann, Jeroen Huijben, J. Kleibeuker, Arie Houselt, Gertjan Koster, Dave Blank, Hans Hilgenkamp, Guus Rijnders, A. Brinkman, and H. Zandvliet. Local probing of coupled interfaces between two-dimensional electron and hole gases in oxide heterostructures by variable-temperature scanning tunneling spectroscopy. *Physical Review B*, 86:35140–, 07 2012.

[93] A. Annadi, A. Putra, Z. Liu, X. Wang, K. Gopinadhan, Zhengtang Huang, Sudesh Dhar, T. Venkatesan, and Ariando Ariando. Electronic correlation and strain effects at the interfaces between polar and nonpolar complex oxides. *Physical Review B*, 86, 08 2012.

[94] Kaveh Ahadi and Susanne Stemmera. Novel metal-insulator transition at the $SmTiO_3/SrTiO_3$ interface. *Physical Review Letters*, 118, 05 2017.

[95] Ryan Need, Patrick Marshall, Eric Kenney, Andreas Suter, Thomas Prokscha, Zaher Salman, Brian Kirby, Susanne Stemmer, Michael Graf, and Stephen Wilson. Quasistatic antiferromagnetism in the quantum wells of $SmTiO_3/SrTiO_3$ heterostructures. *npj Quantum Materials*, 3, 12 2018.

[96] Clayton Jackson, Jack Zhang, Christopher Freeze, and Susanne Stemmer. Quantum critical behaviour in confined $SrTiO_3$ quantum wells embedded in antiferromagnetic $SmTiO_3$. *Nature communications*, 5:4258, 07 2014.

[97] Nicolas Reyren, Stefano Gariglio, Andrea Caviglia, Didier Jaccard, Toni Schneider, and J.-M Triscone. Anisotropy of the superconducting transport properties of the laalo3/srtio3 interface. *Applied Physics Letters*, 94:112506 – 112506, 04 2009.

[98] V. L. Ginzburg. On surface superconductivity. *Physics Letters*, 13(2):101–102, November 1964.

[99] M. Kim, Y. Kozuka, C. Bell, Y. Hikita, and H. Y. Hwang. Intrinsic spin-orbit coupling in superconducting δ-doped $srtio_3$ heterostructures. *Phys. Rev. B*, 86:085121, Aug 2012.

[100] Julie Bert, Katja Nowack, Beena Kalisky, Hilary Noad, John Kirtley, Chris Bell, Hiroki Sato, Masayuki Hosoda, Yasuyuki Hikita, Harold Hwang, and Kathryn Moler. Gate-tuned superfluid density at the superconducting $laalo_3/srtio_3$ interface. *Phys. Rev. B*, 86, 08 2012.

[101] Guanglei Cheng, Michelle Tomczyk, Shicheng Lu, Joshua Veazey, Mengchen Huang, Patrick Irvin, Sangwoo Ryu, Hyungwoo Lee, Chang-Beom Eom, Carl Hellberg, and Jeremy Levy. Electron pairing without superconductivity. *Nature*, 521:196–9, 05 2015.

[102] Anil Annadi, Guanglei Cheng, Hyungwoo Lee, Jung-Woo Lee, Shicheng Lu, Anthony Tylan-Tyler, Megan Briggeman, Michelle Tomczyk, Mengchen Huang, David Pekker, Chang-Beom Eom, Patrick Irvin, and Jeremy Levy. Quantized ballistic transport of electrons and electron pairs in $LaAlO_3/SrTiO_3$ nanowires. *Nano Letters*, 18, 06 2018.

[103] Mengchen Huang, Feng Bi, Sangwoo Ryu, Chang-Beom Eom, Patrick Irvin, and Jeremy Levy. Direct imaging of $LaAlO_3/SrTiO_3$ nanostructures using piezoresponse force microscopy. *APL Materials*, 1:052110, 11 2013.

[104] Alexei Gruverman and Sergei Kalinin. Piezoresponse force microscopy and recent advances in nanoscale studies of ferroelectrics. *Journal of Materials Science*, 41:107–116, 01 2006.

[105] C. L. Jia, S. B. Mi, M. Faley, U. Poppe, J. Schubert, and K. Urban. Oxygen octahedron reconstruction in the $srtio_3/laalo_3$ heterointerfaces investigated us-

ing aberration-corrected ultrahigh-resolution transmission electron microscopy. *Phys. Rev. B*, 79:081405, Feb 2009.

[106] Jean-Luc Maurice, C. Carretero, Marie-Jose Casanove, K. Bouzehouane, S. Guyard, Eric Larquet, and J. Contour. Electronic conductivity and structural distortion at the interface between insulators srtio3 and laalo3. *physica status solidi (a)*, 203, 07 2006.

[107] P. R. Willmott, S. A. Pauli, R. Herger, C. M. Schlepütz, D. Martoccia, B. D. Patterson, B. Delley, R. Clarke, D. Kumah, C. Cionca, and Y. Yacoby. Structural basis for the conducting interface between laalo$_3$ and srtio$_3$. *Phys. Rev. Lett.*, 99:155502, Oct 2007.

[108] V. Vonk, M. Huijben, K. J. I. Driessen, P. Tinnemans, A. Brinkman, S. Harkema, and H. Graafsma. Interface structure of SrTio$_3$LaAlo$_3$ at elevated temperatures studied in situ by synchrotron x rays. *Phys. Rev. B*, 75:235417, Jun 2007.

[109] Clayton A. Jackson and Susanne Stemmer. Interface-induced magnetism in perovskite quantum wells. *Phys. Rev. B*, 88:180403, Nov 2013.

[110] Evgeny Mikheev, Christopher R. Freeze, Brandon J. Isaac, Tyler A. Cain, and Susanne Stemmer. Separation of transport lifetimes in SrTiO$_3$-based two-dimensional electron liquids. *Phys. Rev. B*, 91:165125, Apr 2015.

[111] Will Hardy, Baani Isaac, Patrick Marshall, Evgeny Mikheev, Panpan Zhou, Susanne Stemmer, and Douglas Natelson. Potential fluctuations at low temperatures in mesoscopic-scale SmTiO$_3$/SrTiO$_3$/SmTiO$_3$ quantum well structures. *ACS nano*, 11, 03 2017.

[112] H.J. Tao, Farun Lu, and E.L. Wolf. Observation of pseudogap in bi2sr2cacu2o8+ single crystals with electron tunneling spectroscopy. *Physica C: Superconductivity*, 282-287:1507–1508, 1997. Proceedings of the International Conference on Materials and Mechanisms of Superconductivity High Temperature Superconductors V.

[113] Tom Timusk and Bryan Statt. The pseudogap in high-temperature superconductors: an experimental survey. *Reports on Progress in Physics*, 62(1):61–122, jan 1999.

[114] Patrick A. Lee, Naoto Nagaosa, and Xiao-Gang Wen. Doping a mott insulator: Physics of high-temperature superconductivity. *Rev. Mod. Phys.*, 78:17–85, Jan 2006.

[115] T. Shimojima, T. Sonobe, W. Malaeb, K. Shinada, A. Chainani, S. Shin, T. Yoshida, S. Ideta, A. Fujimori, H. Kumigashira, K. Ono, Y. Nakashima, H. Anzai, M. Arita, A. Ino, H. Namatame, M. Taniguchi, M. Nakajima, S. Uchida, Y. Tomioka, T. Ito, K. Kihou, C. H. Lee, A. Iyo, H. Eisaki, K. Ohgushi, S. Kasahara, T. Terashima, H. Ikeda, T. Shibauchi, Y. Matsuda, and K. Ishizaka. Pseudogap formation above the superconducting dome in iron pnictides. *Phys. Rev. B*, 89:045101, Jan 2014.

[116] M Opel, F Venturini, R Hackl, B Revaz, H Berger, and L Forró. Superconducting gap

and pseudogap in bi-2212. *Physica B: Condensed Matter*, 284-288:669–670, 2000.

[117] Christoph Richter, H Boschker, W Dietsche, Evangelos Fillis-Tsirakis, Rainer Jany, Florian Loder, L Kourkoutis, D Muller, J Kirtley, C. Schneider, and Jochen Mannhart. Interface superconductor with gap behaviour like a high-temperature superconductor. *Nature*, 502, 10 2013.

[118] Patrick Marshall, Honggyu Kim, and Susanne Stemmer. Disorder versus two transport lifetimes in a strongly correlated electron liquid. *Scientific Reports*, 7, 08 2017.

[119] Daniel C. Harris. A peek into the history of sapphire crystal growth. volume 5078, pages 1 – 11. International Society for Optics and Photonics, SPIE, 2003.

[120] Masashi Kawasaki, Kazuhiro Takahashi, Tatsuro Maeda, Ryuta Tsuchiya, Makoto Shinohara, Osamu Ishiyama, Takuzo Yonezawa, Mamoru Yoshimoto, and Hideomi Koinuma. Atomic control of the $SrTiO_3$ crystal surface. *Science*, 266:1540–1542, 12 1994.

[121] Gertjan Koster, Boike Kropman, Guus Rijnders, Dave Blank, and Horst Rogalla. Quasi-ideal strontium titanate crystal surfaces through formation of strontium hydroxide. *Applied Physics Letters*, 73:2920–2922, 11 1998.

[122] Elliott Ortmann, Agham Posadas, and Alex Demkov. The mbe growth of arbitrarily thick srtio 3 /laalo 3 quantum well heterostructures for use in next-generation optoelectronic devices. *Journal of Applied Physics*, 124:015301, 07 2018.

[123] Graziella Malandrino, Ignazio Fragalà, and P. Scardi. Cheminform abstract: Heteroepitaxy of laalo3 (100) on srtio3 (100): In situ growth of laalo3 thin films by metalorganic chemical vapor deposition from a liquid single source. *Cheminform*, 30, 03 2010.

[124] Ishrat Dildar, Mariya Neklyudova, Qiang Xu, Henny Zandbergen, S. Harkema, D. Boltje, and J. Aarts. Growing laalo3/srtio3 interfaces by sputter deposition. *AIP Advances*, 5, 06 2015.

[125] Wikipedia contributors. Pld – wikipedia, the free encyclopedia, 2022. [Online; accessed 4-October-2022].

[126] R. Kuzel and J. Bursik. On x-ray diffraction study of preferred grain orientations in polycrystalline thin films — multicomponent texture in $KTaO_3$ films. *Thin Solid Films*, 530:2–8, 2013. 6th Size-Strain International Conference Diffraction analysis of the microstructure of materials.

[127] Guus Rijnders, Gertjan Koster, Dave Blank, and Horst Rogalla. In situ monitoring during pulsed laser deposition of complex oxides using reflection high energy electron diffraction under high oxygen pressure. *Applied Physics Letters - APPL PHYS LETT*, 70:1888–1890, 04 1997.

[128] Wikipedia contributors. X-ray crystallography — wikipedia, the free encyclopedia. `https://en.wikipedia.org/w/index.php?title=X-ray_crystallography&oldid=1113855911`, 2022. [Online; accessed 4-October-2022].

[129] T. Toshima, Hiroyuki Ishikawa, Satoshi Tanda, and Tomohiro Akiyama. Multipod crystals of perovskite srtio 3. *Crystal Growth Design - CRYST GROWTH DES*, 8:2066–2069, 07 2008.

[130] Jianan Li. Graphene-complex oxide heterostructure. September 2019.

[131] Alejandro Enrique Plaza, Nicola Manca, Cristina Bernini, Daniele Marré , and Luca Pellegrino. The role of etching anisotropy in the fabrication of freestanding oxide microstructures on SrTiOsub3/sub(100), SrTiOsub3/sub(110), and SrTiOsub3/sub(111) substrates. *Applied Physics Letters*, 119(3):033504, jul 2021.

[132] Victor Leca, Guus Rijnders, Gertjan Koster, Dave H. A. Blank, and Horst Rogalla. Wet etching methods for perovskite substrates. *MRS Proceedings*, 587:O3.6, 1999.

[133] Jens Dienelt, Klaus Zimmer, Frieder Bigl, and Roland Höhne. Investigations of different dry etching methods on laalo3. *Journal of Vacuum Science and Technology*, 17:2531–2534, 1999.

[134] Guanyu Chen, Eric Cheung, Yu Cao, Jisheng Pan, and Aaron Danner. Analysis of perovskite oxides etching using argon inductively coupled plasmas for photonics applications, 11 2020.

[135] Nicolas Rivas, Aslihan Babayigit, Bert Conings, Torsten Schwarz, Andreas Sturm, Alba Manjón, Oana Cojocaru-Mirédin, Baptiste Gault, and Frank Renner. Cryo-focused ion beam preparation of perovskite based solar cells for atom probe tomography. *PLOS ONE*, 15:e0227920, 01 2020.

[136] M.J Vasile, R Nassar, J Xie, and H Guo. Microfabrication techniques using focused ion beams and emergent applications. *Micron*, 30(3):235–244, 1999.

[137] Bryan Matthew Love. Mechanical and laser scribing for use as precision shaping techniques. May 2001.

[138] Y. AHN, T. N. Farris, and Chandrasekar S. Elastic stress fields caused by sliding microindentation of brittle materials. *NIST Special Publication*, 847:71–81, 1993.

[139] Pouya Moetakef, Clayton A. Jackson, Jinwoo Hwang, Leon Balents, S. James Allen, and Susanne Stemmer. Toward an artificial mott insulator: Correlations in confined high-density electron liquids in $SrTiO_3$. *Phys. Rev. B*, 86:201102, Nov 2012.

[140] Jack Y. Zhang, Clayton A. Jackson, Ru Chen, Santosh Raghavan, Pouya Moetakef, Leon Balents, and Susanne Stemmer. Correlation between metal-insulator transitions

and structural distortions in high-electron-density $SrTiO_3$ quantum wells. *Phys. Rev. B*, 89:075140, Feb 2014.

[141] Pouya Motakef, Jack Zhang, Santosh Raghavan, Adam Kajdos, and Susanne Stemmer. Growth window and effect of substrate symmetry in hybrid molecular beam epitaxy of a mott insulating rare earth titanate. *Journal of Vacuum Science & Technology A Vacuum Surfaces and Films*, A:041503, 05 2013.

[142] Keisuke Shibuya, Tsuyoshi Ohnishi, Masashi Kawasaki, Hideomi Koinuma, and Mikk Lippmaa. Metallic $latio_3$/$SrTiO_3$ superlattice films on the $SrTiO_3$ (100) surface. *Japanese Journal of Applied Physics*, 43, 09 2004.

[143] Bharat Jalan, Roman Engel-Herbert, Nicholas Wright, and Susanne Stemmer. Growth of high-quality $SrTiO_3$ films using a hybrid molecular beam epitaxy approach. *Journal of Vacuum Science & Technology A - J VAC SCI TECHNOL A*, 27, 05 2009.

[144] Evgeny Mikheev, Christopher R. Freeze, Brandon J. Isaac, Tyler A. Cain, and Susanne Stemmer. Separation of transport lifetimes in $SrTiO_3$-based two-dimensional electron liquids. *Phys. Rev. B*, 91:165125, Apr 2015.

[145] D. J. Scalapino and R. D. Parks. *Superconductivity.* 1969.

[146] Tinkham M. *Introduction to Superconductivity.* 1975.

[147] Inc. Agilent Technologies. *Agilent Technologies 5500 Scanning Probe Microscope, User's Guide*, 2011.

[148] Andrew Barron and many others. Physical methods in chemistry and nano science. 06 2012.

[149] Matthew Linford. Introduction to surface and material analysis and to various analytical techniques. *Vacuum Technology & Coating*, pages 27 – 33, 02 2014.

[150] Elisabeth Soergel. Piezoresponse force microscopy (pfm). *Journal of Physics D: Applied Physics*, 44:464003, 11 2011.

[151] Prashant Potnis, Nien-Ti Tsou, and John Huber. A review of domain modelling and domain imaging techniques in ferroelectric crystals. *Materials*, 4, 12 2011.

[152] Brian Rodriguez, Sergei Kalinin, Stephen Jesse, Gary Thompson, A Vertegel, Sophia Hohlbauch, and Roger Proksch. Nanoelectromechanics of inorganic and biological systems: From structural imaging to local functionalities. *Microscopy Today*, 16, 01 2008.

[153] Peng Jiang, Fei Yan, Ehsan Nasr Esfahani, Shuhong Xie, Daifeng Zou, Xiaoyan Liu, Hairong Zheng, and Jiangyu Li. Electromechanical coupling of murine lung tissues

probed by piezoresponse force microscopy. *ACS Biomaterials Science & Engineering*, 3, 05 2017.

[154] Feng Bi, Mengchen Huang, Chung Wung Bark, Sangwoo Ryu, Sanghan Lee, Chang-Beom Eom, Patrick Irvin, and Jeremy Levy. Electro-mechanical response of top-gated $LaAlO_3/SrTiO_3$ heterostructures, 2013.

[155] Michelle Tomczyk, Rongpu Zhou, Hyungwoo Lee, Jung-Woo Lee, Guanglei Cheng, Mengchen Huang, Patrick Irvin, Chang-Beom Eom, and Jeremy Levy. Electrostatically tuned dimensional crossover in $LaAlO_3/SrTiO_3$ heterostructures. *APL Materials*, 5:106107, 10 2017.

[156] Yuhe Tang, Anthony Tylan-Tyler, Hyungwoo Lee, Jung-Woo Lee, Michelle Tomczyk, Mengchen Huang, Chang-Beom Eom, Patrick Irvin, and Jeremy Levy. Long-range non-coulombic electron–electron interactions between $LaAlO_3/SrTiO_3$ nanowires. *Advanced Materials Interfaces*, 6, 04 2019.

[157] Megan Briggeman, Michelle Tomczyk, Binbin Tian, Hyungwoo Lee, Jung-Woo Lee, Yuchi He, Anthony Tylan-Tyler, Mengchen Huang, Chang-Beom Eom, David Pekker, Roger Mong, Patrick Irvin, and Jeremy Levy. Pascal conductance series in ballistic one-dimensional $LaAlO_3/SrTiO_3$ channels. *Science*, 367:769–772, 02 2020.

[158] Michelle Tomczyk, Guanglei Cheng, Hyungwoo Lee, Shicheng Lu, A. Annadi, Joshua Veazey, Mengchen Huang, Patrick Irvin, Sangwoo Ryu, Chang-Beom Eom, and Jeremy Levy. Micrometer-scale ballistic transport of electron pairs in $LaAlO_3/SrTiO_3$ nanowires. *Physical Review Letters*, 117, 01 2016.

[159] Megan Briggeman, Hyungwoo Lee, Jung-Woo Lee, Kitae Eom, François Damanet, Elliott Mansfield, Jianan Li, Mengchen Huang, Andrew Daley, Chang-Beom Eom, Patrick Irvin, and Jeremy Levy. One-dimensional kronig–penney superlattices at the $LaAlO_3/SrTiO_3$ interface. *Nature Physics*, 17:1–6, 07 2021.

[160] Feng Bi, Daniela Bogorin, Cheng Cen, Chung Wung Bark, J. W. Park, Chang-Beom Eom, and Jeremy Levy. "water-cycle" mechanism for writing and erasing nanostructures at the $LaAlO_3/SrTiO_3$ interface. *Applied Physics Letters*, 97:173110–173110, 10 2010.

[161] Keith Brown, Shu He, Daniel Eichelsdoerfer, Mengchen Huang, Ishan Levy, Hyungwoo Lee, Sangwoo Ryu, Patrick Irvin, Jose Mendez-Arroyo, Chang-Beom Eom, Chad Mirkin, and Jeremy Levy. Giant conductivity switching of $LaAlO_3/SrTiO_3$ heterointerfaces governed by surface protonation. *Nature Communications*, 7:10681, 02 2016.

[162] Tanat Kissikov, Rajib Sarkar, B. Bush, M. Lawson, P. Canfield, and N. Curro. Nuclear magnetic resonance probe head design for precision strain control. *Review of Scientific Instruments*, 88, 08 2017.

[163] M. Ikeda, Thanapat Worasaran, Johanna Palmstrom, P. Walmsley, and I. Fisher.

Symmetric and antisymmetric strain as continuous tuning parameters for electronic nematic order. 98, 12 2018.

[164] Michele Ghini, Matthew Bristow, Joseph C. A. Prentice, Samuel Sutherland, Samuele Sanna, A. A. Haghighirad, and A. I. Coldea. Strain tuning of nematicity and superconductivity in single crystals of fese. *Phys. Rev. B*, 103:205139, May 2021.

[165] Na Hyun Jo, Lin-Lin Wang, Peter P. Orth, Sergey L. Bud'ko, and Paul C. Canfield. Magnetoelastoresistance in WTe_2 : Exploring electronic structure and extremely large magnetoresistance under strain. *Proceedings of the National Academy of Sciences*, 116(51):25524–25529, dec 2019.

[166] John Cenker, Shivesh Sivakumar, Kaichen Xie, Aaron Miller, Pearl Thijssen, Zhaoyu Liu, Avalon Dismukes, Jordan Fonseca, Eric Anderson, Xiaoyang Zhu, Xavier Roy, Xiao di, Jiun-Haw Chu, Ting Cao, and Xiaodong Xu. Reversible strain-induced magnetic phase transition in a van der waals magnet. *Nature Nanotechnology*, 17:1–6, 03 2022.

[167] Jong-Woo Kim, S. H. Chun, Y. Choi, B. J. Kim, M. H. Upton, and P. J. Ryan. Controlling symmetry of spin-orbit entangled pseudospin state through uniaxial strain. *Phys. Rev. B*, 102:054420, Aug 2020.

[168] Ayman H. Said, Harald Sinn, Thomas S. Toellner, Ercan E. Alp, Thomas Gog, Bogdan M. Leu, Sunil Bean, and Ahmet Alatas. High-energy-resolution inelastic x-ray scattering spectrometer at beamline 30-id of the advanced photon source. *Journal of Synchrotron Radiation*, 27:827–835, May 2020.

[169] W. Schranz, P. Sondergeld, A. V. Kityk, and E. K. H. Salje. Elastic properties of $SrTiO_3$ crystals at ultralow frequencies. *Phase Transitions*, 69(1):61–76, 1999.

[170] Martin Schmidbauer, Albert Kwasniewski, and Jutta Schwarzkopf. High-precision absolute lattice parameter determination of $SrTiO_3$, $DyScO_3$ and $NdGaO_3$ single crystals. *Acta crystallographica. Section B, Structural science*, 68 Pt 1:8–14, 2012.

[171] George Fischer, Zichao Wang, and Shun-ichiro Karato. Elasticity of $CaTiO_3$, $SrTiO_3$ and $BaTiO_3$ perovskites up to 3.0 GPa: The effect of crystallographic structure. *Physics and Chemistry of Minerals*, 20:97–103, 01 1993.

[172] Graham Batey and Gustav Teleberg. Principles of dilution refrigeration - a brief technology guide. *Oxford Instruments NanoScience*, 2015.

[173] Seth Devore, Alexandre Gauthier, Jeremy Levy, and Chandralekha Singh. Improving student understanding of lock-in amplifiers. *American Journal of Physics*, 84, 01 2016.

[174] Michael Schmid, David Rath, and Ulrike Diebold. Why and how savitzky–golay filters should be replaced. *ACS Measurement Science Au*, 2, 02 2022.

[175] Ronald W. Schafer. What is a savitzky-golay filter? [lecture notes]. *IEEE Signal Processing Magazine*, 28(4):111–117, 2011.

[176] V. A. Sidorov, M. Nicklas, P. G. Pagliuso, J. L. Sarrao, Y. Bang, A. V. Balatsky, and J. D. Thompson. Superconductivity and quantum criticality in $\mathrm{CeCoIn_5}$. *Phys. Rev. Lett.*, 89:157004, Sep 2002.

[177] K Rossnagel. On the origin of charge-density waves in select layered transition-metal dichalcogenides. *Journal of Physics: Condensed Matter*, 23(21):213001, may 2011.

[178] S. Allen, Adam Hauser, Evgeny Mikheev, Jack Zhang, Nelson Moreno, Junwoo Son, Daniel Ouellette, James Kally, Alexander Kozhanov, Leon Balents, and Susanne Stemmer. Gaps and pseudogaps in perovskite rare earth nickelates. *APL Materials*, 3:062503, 06 2015.

[179] J Stewart, J Gaebler, and D. Jin. Using photoemission spectroscopy to probe a strongly interacting fermi gas. *Nature*, 454:744–7, 09 2008.

[180] Selim Jochim. Bose-einstein condensation of molecules. *Fraunhofer ZV*, 302, 12 2003.

[181] V. M. Krasnov, A. Yurgens, D. Winkler, P. Delsing, and T. Claeson. Evidence for coexistence of the superconducting gap and the pseudogap in bi-2212 from intrinsic tunneling spectroscopy. *Phys. Rev. Lett.*, 84:5860–5863, Jun 2000.

[182] A Matsuda, S Sugita, T Fujii, and T Watanabe. Study of pseudogap phenomena by stm and other probes. *Journal of Physics and Chemistry of Solids*, 62(1):65–68, 2001.

[183] Takahiro Hashimoto, Yuichi Ota, Akihiro Tsuzuki, Tsubaki Nagashima, Akiko Fukushima, Shigeru Kasahara, Yuji Matsuda, Kohei Matsuura, Yuta Mizukami, Takasada Shibauchi, Shik Shin, and Kozo Okazaki. Bose-einstein condensation superconductivity induced by disappearance of the nematic state. *Science Advances*, 6:eabb9052, 11 2020.

[184] Su-Di Chen, Makoto Hashimoto, Yu He, Dongjoon Song, Ke-Jun Xu, Jun-Feng He, Thomas Devereaux, Hiroshi Eisaki, D. Lu, J. Zaanen, and Zhi-Xun Shen. Incoherent strange metal sharply bounded by a critical doping in Bi2212. *Science*, 366:1099–1102, 11 2019.

[185] Marcel Franz. Superconductivity: Importance of fluctuations. *Nature Physics*, 3:686–687, 10 2007.

[186] A.G. Aronov B.L. Altshuler. Zero bias anomaly in tunnel resistance and electron-electron interaction. *Solid State Communications*, 30(3):115–117, 1979.

[187] Mark Lee, J. G. Massey, V. L. Nguyen, and B. I. Shklovskii. Coulomb gap in a doped semiconductor near the metal-insulator transition: Tunneling experiment and scaling ansatz. *Phys. Rev. B*, 60:1582–1591, Jul 1999.

[188] Ivan Bozovic and Jeremy Levy. Pre-formed cooper pairs in copper oxides and $LaAlO_3$—$SrTiO_3$ heterostructures. *Nature Physics*, 16:712–717, 07 2020.

[189] R.M. Feenstra, Joseph A. Stroscio, and A.P. Fein. Tunneling spectroscopy of the si(111)2 × 1 surface. *Surface Science*, 181(1):295–306, 1987.

[190] Joseph A. Stroscio, R. M. Feenstra, and A. P. Fein. Electronic structure of the Si(111)2 × 1 surface by scanning-tunneling microscopy. *Phys. Rev. Lett.*, 57:2579–2582, Nov 1986.

[191] N. D. Lang. Spectroscopy of single atoms in the scanning tunneling microscope. *Phys. Rev. B*, 34:5947–5950, Oct 1986.

[192] J. Bardeen, L. N. Cooper, and J. R. Schrieffer. Theory of superconductivity. *Phys. Rev.*, 108:1175–1204, Dec 1957.

[193] Panpan Zhou, Liyang Chen, Yue Liu, Ilya Sochnikov, Anthony T. Bollinger, Myung-Geun Han, Yimei Zhu, Xi He, Ivan Boz

ović, and Douglas Natelson. Electron pairing in the pseudogap state revealed by shot noise in copper oxide junctions. *Nature*, 572(7770):493–496, aug 2019.

[194] D. M. Eagles. Possible pairing without superconductivity at low carrier concentrations in bulk and thin-film superconducting semiconductors. *Phys. Rev.*, 186:456–463, Oct 1969.

[195] G. Binnig, A. Baratoff, H. E. Hoenig, and J. G. Bednorz. Two-band superconductivity in nb-doped $srtio_3$. *Phys. Rev. Lett.*, 45:1352–1355, Oct 1980.

[196] Alexis Baratoff and Gerd Binnig. Mechanism of superconductivity in srtio3. *Physica B+C*, 108(1):1335–1336, 1981.

[197] Jonathan Ruhman and Patrick A. Lee. Superconductivity at very low density: The case of strontium titanate. *Phys. Rev. B*, 94:224515, Dec 2016.

[198] Markus Thiemann, Manfred H. Beutel, Martin Dressel, Nicholas R. Lee-Hone, David M. Broun, Evangelos Fillis-Tsirakis, Hans Boschker, Jochen Mannhart, and Marc Scheffler. Single-gap superconductivity and dome of superfluid density in nb-doped $srtio_3$. *Phys. Rev. Lett.*, 120:237002, Jun 2018.

[199] Aditi Nethwewala, Hyungwoo Lee, Megan Briggeman, Yuhe Tang, Jianan Li, Jung-woo Lee, Chang-Beom Eom, Patrick Irvin, and Jeremy Levy. Inhomogeneous energy landscape in laalo 3 /srtio 3 nanostructures. *Nanoscale Horizons*, 4, 05 2019.

[200] Razorbill Instruments. Razorbill instrument user guide: how to use and care for your device. 12 2020.

[201] D. A. Dikin, M. Mehta, C. W. Bark, C. M. Folkman, C. B. Eom, and V. Chandrasekhar. Coexistence of superconductivity and ferromagnetism in two dimensions. *Phys. Rev. Lett.*, 107:056802, Jul 2011.

[202] Sumilan Banerjee, Onur Erten, and Mohit Randeria. Ferromagnetic exchange, spin-orbit coupling and spiral magnetism at the laalo3/srtio3 interface. *Nature Physics*, 9, 03 2013.

[203] Zhicheng Zhong, Anna T'oth, and Karsten Held. Theory of spin-orbit coupling at laalo3/srtio3 interfaces and srtio3 surfaces. *Phys. Rev. B*, 87:161102, Apr 2013.

[204] P. Zubko, G. Catalan, A. Buckley, P. R. L. Welche, and J. F. Scott. Strain-gradient-induced polarization in srtio$_3$ single crystals. *Phys. Rev. Lett.*, 99:167601, Oct 2007.

[205] Daniel Grupp and A. Goldman. Giant piezoelectric effect in stronium titanate at cryogenic temperatures. *Science (New York, N.Y.)*, 276:392–4, 05 1997.

[206] Guanglei Cheng, Joshua P. Veazey, Patrick Irvin, Cheng Cen, Daniela F. Bogorin, Feng Bi, Mengchen Huang, Shicheng Lu, Chung-Wung Bark, Sangwoo Ryu, Kwang-Hwan Cho, Chang-Beom Eom, and Jeremy Levy. Anomalous transport in sketched nanostructures at the laalo$_3$/srtio$_3$ interface. *Phys. Rev. X*, 3:011021, Mar 2013.

[207] W. J. Skocpol and M. Tinkham. Fluctuations near superconducting phase transitions. *Reports on Progress in Physics*, 38(9):1049–1097, September 1975.

[208] Changjiang Liu, Yan Xi, Dafei Jin, Yang Ma, Haw-Wen Hsiao, Yulin Lin, Terence Bretz-Sullivan, Xianjing Zhou, John Pearson, Brandon Fisher, J. Jiang, Wei Han, Jian-Min Zuo, Jianguo Wen, Dillon Fong, Jirong Sun, Hua Zhou, and Anand Bhattacharya. Two-dimensional superconductivity and anisotropic transport at $KTaO_3$ (111) interfaces. *Science*, 371:716–721, 01 2021.

[209] Zheng Chen, Zhongran Liu, Yanqiu Sun, Xiaoxin Chen, Yuan Liu, Hui Zhang, Hekang Li, Meng Zhang, Siyuan Hong, Tianshuang Ren, Chao Zhang, He Tian, Yi Zhou, Jirong Sun, and Yanwu Xie. Electric field control of superconductivity at the $LaAlO_3/KTaO_3$(110) heterointerface. *Phys. Rev. Lett.*, 126:026802, Jan 2021.

[210] Yang Ma, Jiasen Niu, Wenyu Xing, Yunyan Yao, Ranran Cai, Jirong Sun, X. C. Xie, Xi Lin, and Wei Han. Superconductor-metal quantum transition at the EuO/$KTaO_3$ interface. *Chinese Physics Letters*, 37(11):117401, nov 2020.

[211] Yanqiu Sun, Yuan Liu, Siyuan Hong, Zheng Chen, Meng Zhang, and Yanwu Xie. Critical thickness in superconducting $LaAlO_3/KTaO_3$(111) heterostructures. *Phys. Rev. Lett.*, 127:086804, Aug 2021.